A DROP-IN CONCEPT FOR DEEP BOREHOLE CANISTER EMPLACEMENT

By

Ethan Allen Bates

SUBMITTED TO THE DEPARTMENT OF NUCLEAR SCIENCE AND ENGINEERING IN PARTIAL FULFILLMENT OF THE REQUIREMENTS FOR THE DEGREES OF

BACHELOR OF SCIENCE IN NUCLEAR SCIENCE AND ENGINEERING
AT THE
MASSACHUSETTS INSTITUTE OF TECHNOLOGY

and

MASTER OF SCIENCE IN NUCLEAR SCIENCE AND ENGINEERING
AT THE
MASSACHUSETTS INSTITUTE OF TECHNOLOGY

JUNE 2011

Signature of Author: _____
Department of Nuclear Science and Engineering
May 8, 2011

Certified by: _____
Prof. Jacopo Buongiorno – Thesis Co-Supervisor
Associate Professor of Nuclear Science and Engineering

Certified by: _____
Prof. Michael J. Driscoll – Thesis Co-Supervisor
Professor Emeritus of Nuclear Science and Engineering

Accepted by: _____
Mujid S. Kazimi
TEPCO Professor of Nuclear Engineering
Chairman, Department Committee on Graduate Students

A DROP-IN CONCEPT FOR DEEP BOREHOLE CANISTER EMPLACEMENT

By Ethan Allen Bates

Submitted to the Department of Nuclear Science and Engineering on May 8, 2011 in partial fulfillment of the requirements for the degrees of Bachelor of Science in Nuclear Science and Engineering and Master of Science in Nuclear Science and Engineering

Abstract

Disposal of high-level nuclear waste in deep boreholes drilled into crystalline bedrock (i.e., "granite") is an interesting repository alternative of long standing. Work at MIT over the past two decades, and more recently in collaboration with the Sandia National Laboratory, has examined a broad spectrum of design aspects associated with this approach. For emplacement, past reports suggest using steel cables to lower each canister into the borehole. This process would require many years to complete and precise control to safely lower the canisters thousands of meters. The current study evaluated a simple, rapid, "passive" procedure for emplacement of canisters in a deep borehole: free-fall release into a water-flooded borehole. The project involves both analytic modeling and $1/5^{th}$ scale experiments on a laboratory mockup. Experiments showed good agreement and validated the model. Depending on the inputs used for the mass and dimensions of the full scale canister and the viscosity of water, the model predicted terminal velocities of 2.4-2.6 m/s (4.5-5.8 mph). Further experiments showed that this could be reduced by 50% by making the surface hydraulically rough. Based on these predictions and a structural analysis, there seems to be little risk of damage when a canister reaches the bottom of the borehole or impacts the stack of previously loaded canisters. For reference, dropping the canister in air from a height of only 0.3 m (1 ft) would result in an impact velocity of 2.44 m/s. Cost estimates for the conventional drill string based method were developed, and the drop-in method was concluded to reduce emplacement costs and time by a minimum of 70%, down to $700,000 per borehole. It is concluded that a simple drop-in procedure deserves serious consideration for adoption as a standard procedure for borehole loading.

Thesis Co-supervisor: Prof. Michael J. Driscoll
Title: Professor Emeritus of Nuclear Science and Engineering

Thesis Co-supervisor: Prof. Jacopo Buongiorno
Title: Associate Professor of Nuclear Science and Engineering

Acknowledgments

Professor Driscoll and Professor Buongiorno were ever-present, and their vast knowledge, continuous support and experience kept me motivated to tackle a wide variety of issues on the intriguing and crucial research area of waste disposal. Without a fellowship and financial support from the Nuclear Science and Engineering department, this research would not have been possible, and for that I am extremely grateful. Dr. Thomas McKrell assisted me with my initial familiarization with experimental procedures and safety, and was always a source of positivity and support. Professor Barbara Hughey was instrumental in providing experimental design advice and sensor hardware. Schlumberger Doll Research Center and Albert Perez have my appreciation for furnishing free use of their confocal microscope to the Department of Nuclear Science and Engineering. I'd also like to thank the support that Sandia has given to deep borehole research at MIT, as it enabled me to travel to conferences to share my research. Daniela Cako, and my twin brother Richard Bates provided indispensible and dedicated moral and technical support during the many hours of derivation, experimentation and explanation of this thesis. Finally, I want to thank my family for raising me in such a supportive and intellectually stimulating environment, allowing me to attend and truly enjoy my experience at MIT.

Table of Contents

List of Figures

List of Tables

1. Introduction

1.1. Objective of the Thesis

This project develops and experimentally verifies an affordable, expedient and reliable method of deploying nuclear waste canisters into deep boreholes. An analytical model based on fluid mechanic first principles aided design of a dimensionally similar experiment, and the results validate the model. Various methods to further increase drag forces and reduce canister velocity were also investigated and successfully integrated into an analytical model. Estimates for the reduction in time and costs associated with the simplified process are made in relation to the overall feasibility of a vertical borehole repository.

1.2. Topic Motivation

1.2.1. Open Fuel Cycle and DOE Contractual Obligation

The unresolved issues of long term nuclear waste disposal in the United States remain a limiting factor in the expansion of nuclear power- a proven and carbon free energy source. Work on the Yucca mountain repository has been suspended, and a Blue Ribbon Commission appointed to recommend a new path forward. Secretary of Energy, Steven Chu, stated that Yucca Mountain would not be considered as one of the alternatives [1]. In the meantime, Finland, Sweden, and Switzerland have successfully pursued repositories in granite, currently scheduled to open in 2020 in Finland and 2025 in Sweden [2].

Despite this change in policy, the truth remains that the U.S government is contractually responsible for removing spent fuel from reactor sites and disposing all commercial nuclear waste [3]. Without a solution by 2020, the government (taxpayers) will have to pay an estimated $12 billion dollars in damages to compensate the utilities for the cost of storing the waste, and further pay $500 million per year after 2020 [4]. Centralized storage has been suggested as an interim solution, but without amending the Nuclear Waste Policy Act (NWPA) of 1982, the DOE cannot legally construct a storage facility until authorization of the final geologic repository. Additionally, under current law the facility could only contain a maximum of 10,000 metric tons of spent fuel, a small fraction of the 60,000 metric tons that is already in spent fuel pools at reactor sites.

In the longer term, closed-fuel cycles could reduce the quantity of high level waste requiring disposal; however, recent MIT and Harvard studies[5]-[8] conclude that a closed fuel cycle will not be economically feasible over the next 50 years or more, and point out that long time scales are required to change the fuel cycle. An MIT study proposes, "the highest priority in fuel cycle analysis, research, development, and demonstration, deserving first call on available funds, lies with efforts that enable robust deployment of the once-through fuel cycle...We believe deep boreholes, as an alternative to mined repositories, should be aggressively pursued" [8]. Therefore, to deal with the volumes of waste generated from the once-through fuel cycle, the quick development of the alternative to mined repositories-deep boreholes- is crucial and justified.

1.3. Overview of Deep Borehole Waste Disposal (DBWD)

DBWD has been proposed as an attractive alternative to shallow mined repositories. The deep borehole disposal strategy involves drilling and lining a borehole a few kilometers (e.g. 4 km) down into a region of the Earth's crust which mainly consists of granite. The feasibility of drilling to such depths has improved over the years with the interest in enhanced geothermal systems (EGS), which can require boreholes to depths greater than 10 km [9][10]. The current estimates of costs for drilling a vertical 0.5 m diameter, 4 km deep hole are between 10-20 million dollars [11][12]. The metric of drilling cost has typically been considered the driver for borehole repository economics. However, detailed cost evaluations of the subsequent operations such as emplacement are quite scarce and not well defined.

Canisters containing spent nuclear fuel are stacked in the lower 2 km of the hole, while the upper region is sealed off with a multilayer plug (bentonite clay,asphalt, and cement for example). A schematic of the DBWD concept is shown in Figure 1-1.

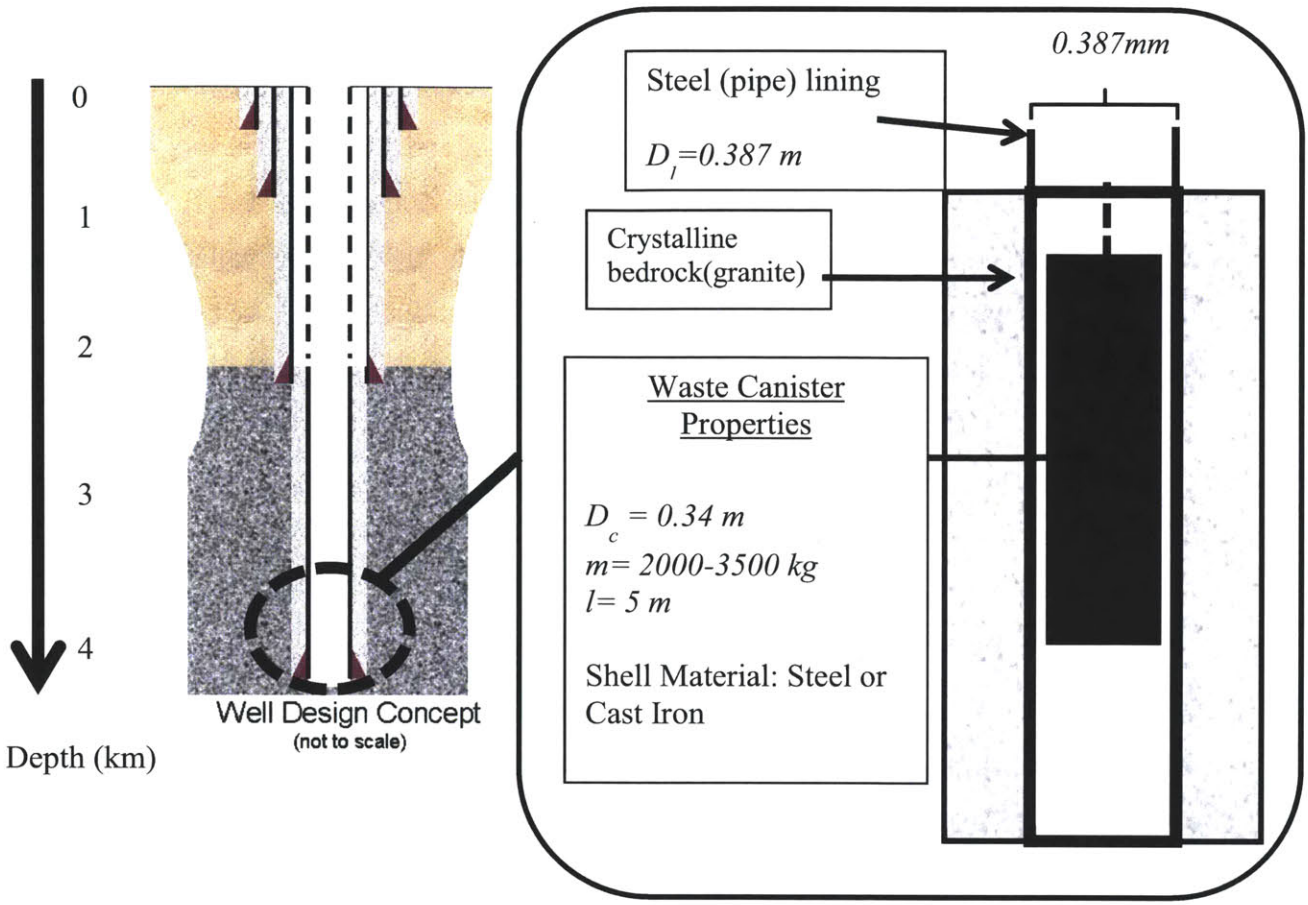

Figure 1-1. Cross section of the deep borehole concept [12][13].

This disposal technique is promising for a number of reasons. Waste in boreholes is significantly deeper and further away from water sources compared to typical shallow mined repositories. This naturally results in better isolation of radionuclides from the surface and humans. Deep granite rock is typically a chemically reducing environment, which reduces radionuclide solubility and decreases their mobility. These geologic conditions with reduced water flow are the main component of the added safety of deep boreholes [14]. The average age of these basement rocks is on the order of billions of years [13]. The performance does not depend as heavily on engineered barriers, which have greater long term uncertainties associated with them. Preliminary performance assessments of DBWD have estimated the peak radioactive dose to a human to be many orders of magnitude less than the internationally recommended limits for post-closure dose [14]. Furthermore, since solid granite formations are relatively common at depths of 2-5 km in the United States, DBWD increases the number of potential sites for waste repositories. Increasing the possible number of sites that can volunteer or spreading the nation's

waste inventory over a number of disposal sites may help reduce political tensions associated with licensing repositories while reducing transportation costs and concerns.

Granite is also being seriously considered as a medium for geologic disposal by several other nations such as China, Japan, and the U.K. [2]. DBWD is a widely researched alternative to mined repositories and has had substantial attention from researchers at Sheffield University in the UK, SKB in Sweden and MIT in collaboration with Sandia National Laboratory[11],[15]-[17] The main areas for improvement to the deep borehole disposal concept are site selection criteria, borehole fill materials, emplacement details and performance risk assessments. A discussion of the emplacement facility and systems is needed to demonstrate the viability of DBWD, but also represent an opportunity for DBWD to make significant savings over shallow mined repositories such as Yucca mountain[13].

1.4. Arrangement of the Thesis

Chapter 2: Emplacement Issues

This chapter deals with the loading issues associated with the Yucca Mountain repository and past proposals by SKB and MIT for emplacement methods in deep boreholes. The feasibility, time, risks and unresolved factors of each study are compared and discussed. The baseline emplacement scenario (that the proposed method is contrasted against) is investigated in this chapter.

Chapter 3: Proposed Emplacement Method

In this chapter, a simple drop-in method is proposed and a reference canister and scenario is defined. Finally, the equipment and facilities required for such an operation are illustrated.

Chapter 4: Analytical Modeling of Proposed Emplacement Method

This chapter details the assumptions and basis for predicting the canister velocity in a flooded borehole. It also outlines other down-hole conditions that could alter the canister's velocity. A dimensional analysis is completed on the pertinent variables, and confirms the functional form of the analytically derived expression for terminal velocity.

Chapter 5: Experiment

This chapter begins with the approach to experimental design, in which a number of constraints were established and met. The experimental apparatus, sensors, materials, and procedure are defined. Discussions of design and results focus heavily on dimensionless variables and frequent comparison to analytical solutions, and consistency of the results is clearly shown, through regression of the data. Alternative methods of reducing the canister velocity are tested and confirmed within the framework of the analytically derived solution.

Chapter 6: Feasibility of Proposed Emplacement Method

The logistical issues of the drop-in method are discussed in this chapter. The primary concerns are thermal, structural, economic and regulatory. Thermal issues are addressed to ensure that the previously defined analytical model applies at the elevated temperatures that the canister surface achieves prior to emplacement. The model and experimental data are used to make velocity predictions for the full scale canister, and the consequences of impact are analyzed. Emplacement economics are discussed in comparison to the previously suggested methods using drilling rigs and strings. The issues of retrievability and its lack of clear definition within current U.S policy are discussed in relation to its implications for DBWD and repository choice in general.

Chapter 7: Summary, Conclusions, and Recommendations

In closing, the results from the analytical modeling, experimental work, and feasibility analysis are presented for the drop-in method. Future topics that will be crucial to an objective and comprehensive comparison of DBWD to other repository designs are suggested.

2. Emplacement Issues

2.1. Chapter Introduction

To give perspective and background on the complexity and challenges posed by emplacement of waste, a discussion of the well documented techniques for emplacement of nuclear waste is given based on the now suspended Yucca Mountain repository in the U.S. The Swedish (SKB) feasibility assessments and emplacement operation details for deep boreholes are reviewed and an analysis is completed to present the cost estimates in current dollars. Finally, the emplacement methods suggested at MIT are discussed on the basis of structural, time and cost issues.

2.2.Previously Suggested Emplacement in Shallow Mined Repositories

2.2.1. Yucca Mountain

Emplacement, the act of deploying and fixing the canisters in their final destination is a complex and crucial process that must be outlined in detail to fully understand the feasibility of a disposal method. In the case of the Yucca Mountain shallow mined repository, emplacement procedures constituted the most expensive phase in the entire disposal process. Figure 2-1 shows a breakdown of costs for the Yucca Mountain repository.

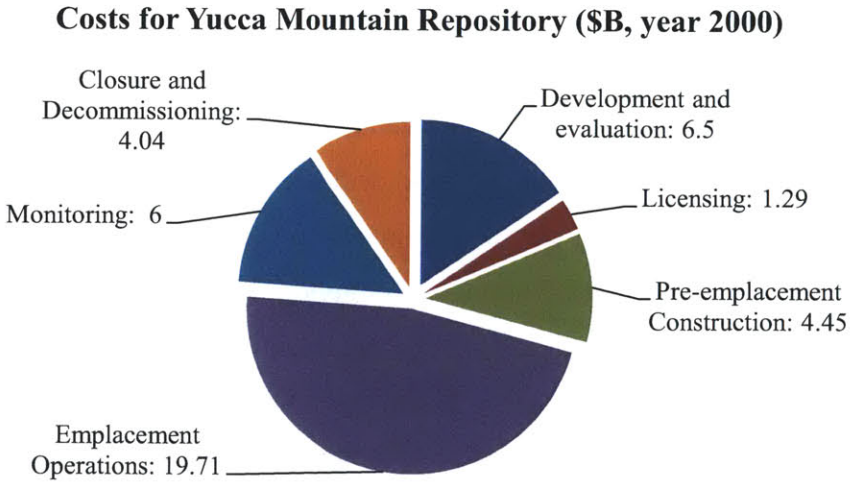

Figure 2-1. Breakdown of costs for the Yucca Mountain repository (with originally defined capacity of 70,000 metric tons) in Billions of year 2000 dollars [12]

Emplacement in shallow mined repositories is complicated by a number of constraints: presence of human workers underground with ventilation, radiation and possibly drainage issues, low visibility in dusty environments, integrity of rails and evacuation routes, spatial, weight and mobility restrictions for emplacement machines with sufficient lifting capabilities [18][19]. Transport of the waste package from the surface facility to the emplacement drift requires a human operated, electrically powered transport locomotive, shown in Figure 2-2.

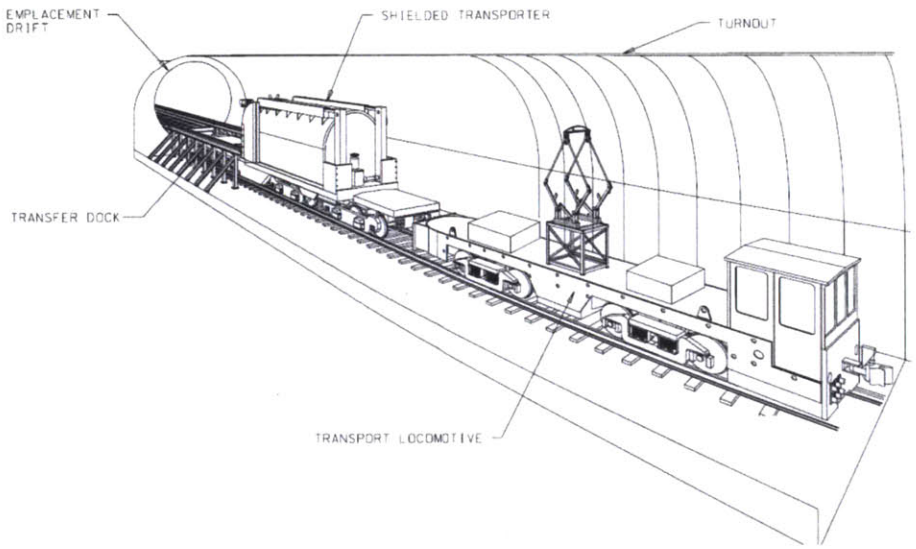

Figure 2-2. Emplacement equipment and transfer dock to emplacement gantry [20]

The human operated transport locomotive travels at 1.78 m/s (4 mph) [21]. The total distance traveled by the waste package between the surface facilities and emplacement panel is 3.54 km, while the distance from the emplacement panel to drift is conservatively approximated to be 1.964 km [21]. Thus, the minimum locomotive time is approximately 3 hours, while the worker is exposed to a low radiation field (2.5 mrem/hr) for almost 2 hours per round trip.

An emplacement gantry, capable of lifting and lowering an unshielded waste package must be transported and installed into a drift before the final filling process can occur. After being installed, the emplacement gantry can receive the waste packages from the shielded transporter. Remote operation via camera and other sensors during the final emplacement process prevents further radiation doses but does not eliminate the risk of human error and accidental drop [22]. Overall, the maximum total individual dose to an emplacement crew

worker was conservatively estimated to be 1890 mrem/year [21]. Risk of derailing, delivery of power (battery), loss of vehicle control, contamination of equipment surfaces and loss of rail integrity (debris on the railways) were also design basis safety issues. Restrictions on the waste emplacement gantry designed for Yucca Mountain repository are listed in Table 2-1 and a conceptual design of the gantry is shown in Figure 2-3.

Table 2-1. General Requirements imposed on the Yucca Mountain emplacement gantry [22]

Operational and Environmental Requirement	**Metric**
Maximum weight of waste packages	73.02 metric tons (161,000 lbs)
Maximum traveling length along drift	808 meters (2651 ft)
Drift diameter	4.8768 meters (16 ft)
Maximum speed of equipment	0.76 m/s (1.7 mph)
Maximum hoist speed of waste package*	0.0305 m/s (6 ft/min)
Maximum ambient temperature (with ventilation)	50 °C (122 °F)
Radiation field at package surface	600.7 rem/hr
Radiation field at bottom lid of package	1290 rem/hr

*Slow hoist speed designated for loads between 70 and 99 tons

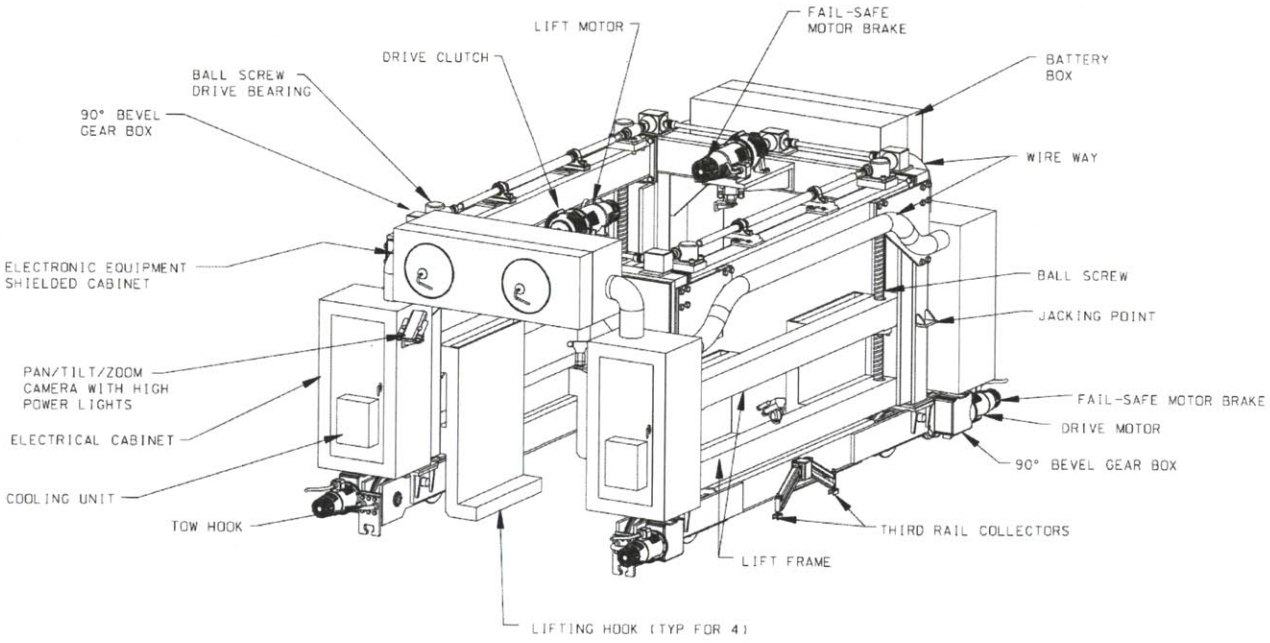

Figure 2-3. Proposed design for the Yucca mountain waste package emplacement gantry[20].

The maximum speed of the remote controlled emplacement gantry is quite small (0.76 m/s) and the maximum distance traveled by the vehicle within the emplacement drift is ~800 meters). Thus, the emplacement gantry movement adds at least another half hour to the loading process. It should be noted that at the time of repository closure (50 years after emplacement and ventilated cooling), the entire loading process must be repeated for the titanium drip shields, which are individually linked together above the waste packages using a similar machine to the emplacement gantry.

2.2.2. Discussion and Comparison to Deep Boreholes

Overall, including inspections and maintenance it was estimated to take between four and eight hours to emplace or retrieve a single waste package (21 PWR assemblies) [21]. This is consistent with a maximum emplacement rate of 600 waste packages per year using two emplacement crews with four workers each. Therefore an estimate of the average loading time for Yucca mountain is one assembly every 10-20 minutes.

The single trip distance traveled in Yucca Mountain is slightly greater than the distance that the waste packages must travel in deep boreholes (3 km). However, 21 (PWR) assemblies are contained in a single waste package, whereas with DBWD, each assembly is loaded into an individual canister, which greatly increases the total number of packages to be emplaced.

Another large factor to consider is that emplacement within deep boreholes is a hoisting process, and therefore would be more accurately described by the 0.0305 m/s vertical speed designated for heavy loads. Emplacement at an average depth of 3 km at this rate would take 27 hours for a single trip down.

2.3. Previously Suggested Emplacement Methods for DBWD

2.3.1. SKB Emplacement in Very Deep Holes (VDH)

A 1989 SKB feasibility study of the VDH concept estimates the time and costs required to emplace canisters in various borehole designs [23]. The process involves using the original drilling rig to force the canister through a viscous "deployment mud". As seen in Table 2-2, the minimum total drilling and deployment time occurs with a borehole drilled with a diameter of 375 mm to a depth of 4 km, with a deployment zone between 2-4 km.

Table 2-2. Borehole options investigated by SKB and time requirements of each stage [23].

Option	Max. depth (km)	Emplacement zone length (km)	Hole diameter at emplacement zone (mm)	Time for drilling of hole (days)	Time for investigation of drilled hole (days)	Time for deployment (days)	Total time required (days)
A	4	2	800	435	100	365	900
B	5.5	2.5	375	319	100	365	784
C	4	2	375	200	100	365	665

The SKB paper estimated the costs for these options, taking into account rig mobilization, construction materials, billing rates, engineering contingency funds and fuel costs. The results are summarized in Table 2-3.

Table 2-3. Borehole options investigated by SKB and overall cost requirements of each stage in 1989 dollars, taken from Appendix 4 of [23].

Option	Daily cost for drilling and investigation period	Daily cost for deployment period	Total cost for drilling and investigation ($M)	Total Cost for deployment period ($M)	Total cost ($M)
A	$77,769	$57,329	41.606	21.925	60.532
B	$48,061	$32,563	20.137	11.885	32.023
C	$48,061*	$32,563*	14.418	11.885	26.304

*The calculations for Option C are not explicitly shown in the reference, but for this table it is assumed that the daily costs would be the same as for Option B, which is the same diameter.

Adjusting these estimates to present dollars is complex because of the opposing effects of inflation, drilling technology improvement, and fuel prices on the cost of drilling and lining boreholes. With the intent to improve the accuracy of predictions based on EGS well costs, MIT surveyed deep drilling projects (in oil and natural gas fields) and developed a drilling cost index; however the indices are only reported up to 2003 [24]. The index takes into account the key metric of depth, and the cost data is smoothed using a 3 year moving average. Figure 2-4 shows the historical trend of the MIT depth dependent (MITDD) drilling cost indices, adjusted for inflation.

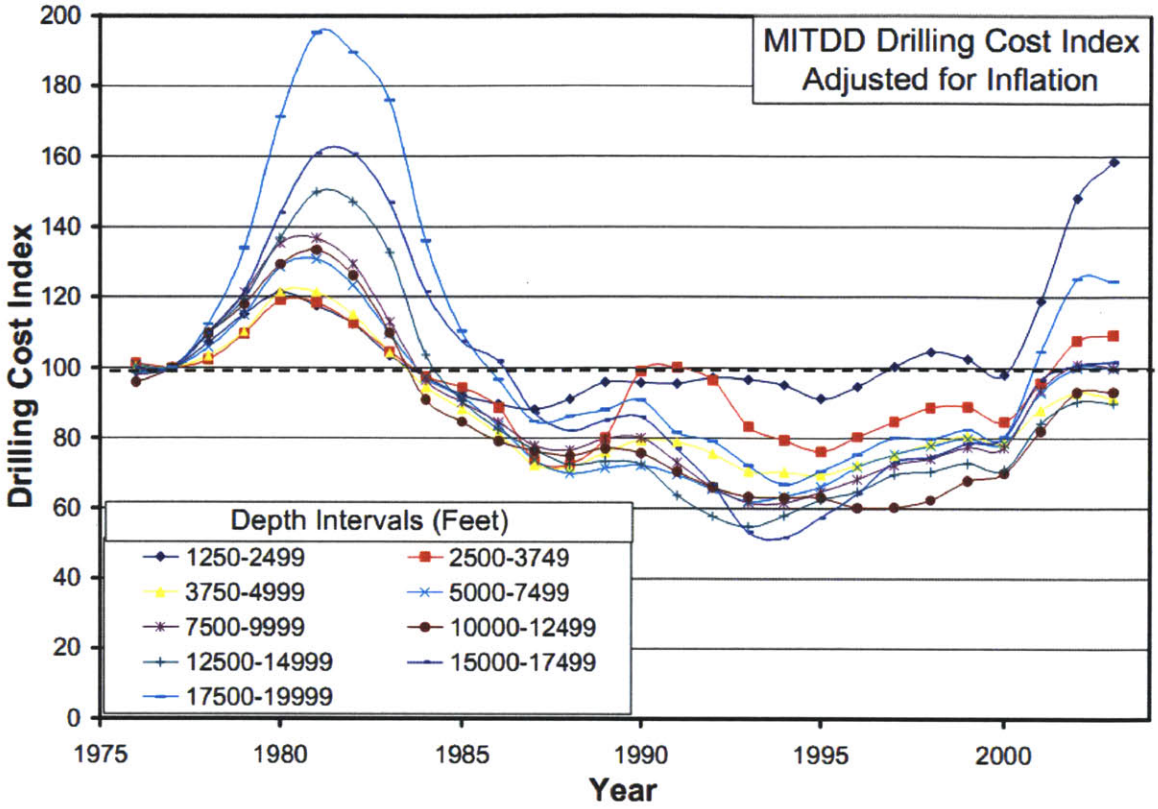

Figure 2-4. MIT depth dependent (MITDD) drilling cost index, adjusted for inflation to year 2003 US $, using the GDP deflator index (1977=100) [24].

The price of fossil fuels, which affects the demand and operating cost for rigs, has a strong correlation with the cost of drilling and emplacement operations, as shown in Figure 2-5.

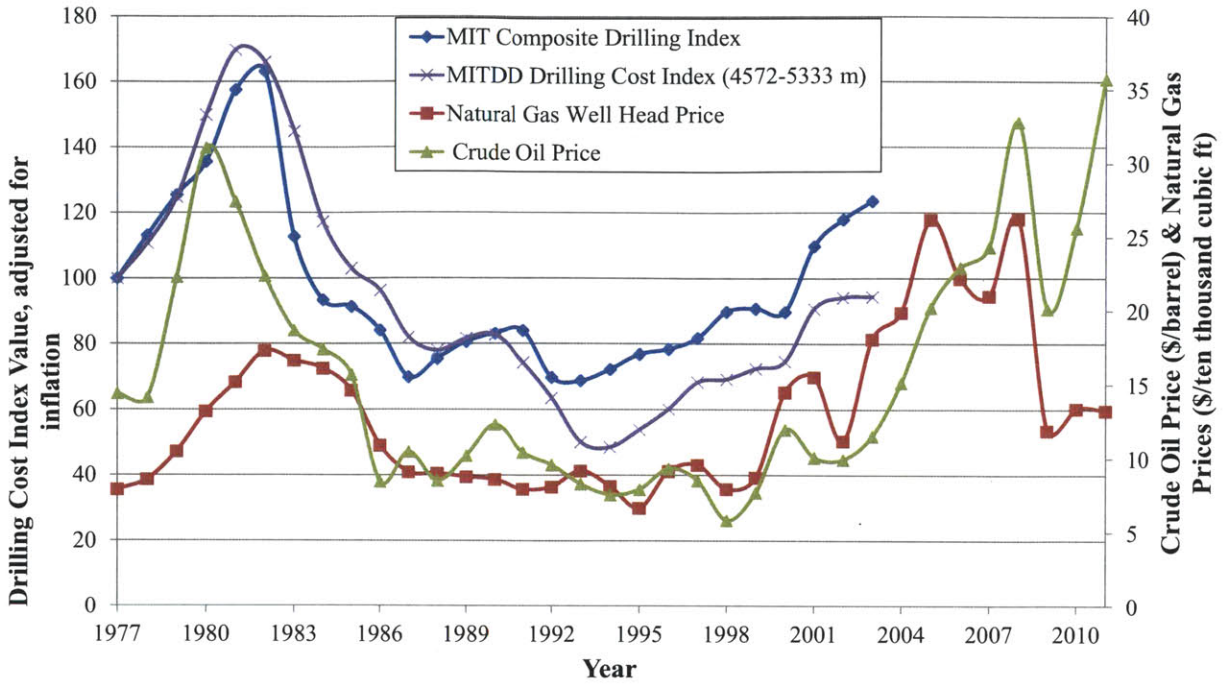

Figure 2-5. MIT drilling cost index vs. crude oil and natural gas prices[24]-[28]. Prices and the drilling index are both adjusted for inflation using the GDP deflator index (1977=100).

The MIT composite drilling cost shown in Figure 2-5 is a composite of all the depth dependent indices. However, the MITDD index for holes drilled to depths between 4572-5333 meters is the most relevant index for this deep borehole study. The current drilling cost index was estimated using a linear correlation between the inflation adjusted crude oil and natural gas prices with the inflation adjusted drilling index. The MITDD drilling cost index was shown to be well fitted by the first-order multiple regression shown in Equation (2-1),

$$MITDD(t) = NG(t) \cdot 2.438 + OIL(t) \cdot 4.019 + 13.7429 \qquad (2\text{-}1)$$

where *MITDD (t)* is the inflation adjusted drilling cost index for a given year, *NG(t)* is the inflation adjusted (to 1977) price of natural gas at the wellhead in tens of thousands of $/ft^3$, *OIL(t)* is the inflation adjusted (to 1977) price of crude oil in $/barrel. The accuracy of the regression is graphed in Figure 2-6 and tabulated in Table 2-4.

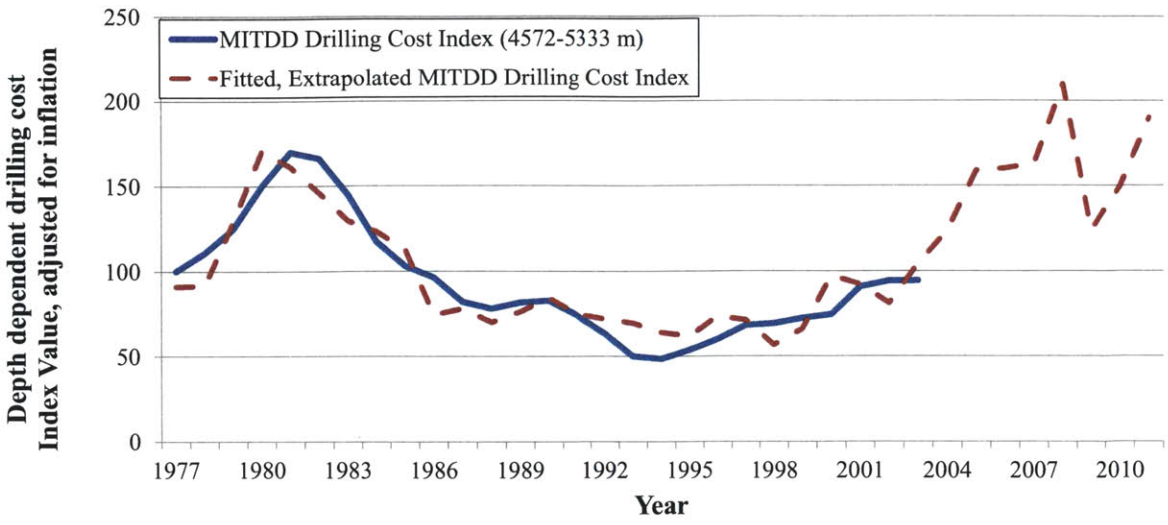

Figure 2-6. Fitted and extrapolated MITDD drilling cost index based on Eq. (2-1) for a borehole depth of 4572-5333 m, plotted against the historical MITDD index data given in [24].

Table 2-4. Tabulated results of Figure 2-6.

Year	MITDD (4572-5333m)	MITDD (4572-5333m), extrapolated using Eq. (2-1)
1989	81.61713	76.13355
1990	82.78544	84.1852
1991	74.1574	74.97812
1992	63.47384	72.03206
1993	50.08678	69.47312
1994	48.51939	64.00517
1995	53.83501	61.85471
1996	60.08529	73.46802
1997	68.24467	71.27343
1998	69.16327	56.57291
1999	72.41705	65.98714
2000	74.61545	97.21308
2001	90.7573	92.18686
2002	94.18135	81.08706
2003	94.38468	104.2887
2004		123.1865
2005		158.9213
2006		160.0463
2007		162.7703
2008		209.63
2009		123.8824
2010		149.4246
2011		182.2067

The current (April 2011) price in 2011 $ of crude oil is $106/barrel, while the price of natural gas is $40.8/ ten thousand ft^3, and those prices are expected to stay level or rise over the next year, due to increasing demand from developing countries and supply shocks resulting from unrest in Middle East and North African countries[25],[27],[28]. A comparison of the index between the years of 1989 to 2011 show that the costs for drilling wells deeper than 1000 m have trended to be much higher. The ratio of the extrapolated MITDD index for 2011 to the MITDD index for 1989 is 2.23. Using the cost index multiplier, the results from Table 2-3 can be adjusted to present estimates for the drillings costs, shown in Table 2-5.

Table 2-5. Borehole options investigated by SKB and overall cost requirements of each stage in present dollars, adjusted using an extrapolated MITDD drilling cost index.

Option	Daily cost for drilling and investigation period	Daily cost for deployment period	Total cost for drilling and investigation ($M)	Total cost for deployment period ($M)	Total cost ($M)
A	$173,424.87	$127,843.67	$92.78	$46.66	$139.45
B	$107,176.03	$72,615.49	$44.91	$26.50	$71.41
C	$107,176.03	$72,615.49	$32.15	$26.50	$58.66

A more recent SKB engineering study conducted in year 2000 [29] estimates a significantly lower drilling time and cost for an Option C type borehole to 4 km (with a more than doubled diameter of 838.2 mm). This discrepancy might result from the fact that it does not include contingency funds or accurately take into account the fuel costs for operating the rig. The study assumed a billing rate of 20,500 € (year 2000)/day, which is approximately equal to $20,500/day (year 2000 $). Adjusting these prices using the MITDD values using Table 2-4 the billing rate becomes $50,063/day. Table 2-6 presents the cost conclusions of the engineering study [29].

Table 2-6. Summary of time and costs included in the SKB engineering study of VDH [29].

Period	Time Required	Costs
Drilling (including drill bits, foam, casing costs)	137 days	4.65 M €, year 2000 (11.355 M $, adjusted using MITDD)
Time for logging testing or pilot hole drilling	Not included	Not included
Emplacement	Not included	Not included

For deployment, the study details a similar technique as previously described by SKB. First the borehole is drained of the drilling foam (liquid used during the drilling phase to facilitate the removal of drilled rock and debris). Then the borehole is completely filled with deployment mud. The deployment mud was described to have as high density as possible so that it functions as a buffer. Using the original drilling rig, the canisters (with Kevlar or plastic longitudinal fins attached) are connected to the drill rod and forced through deployment mud until they reach the 4km deep deployment zone. Eight shearing pins, used to ensure that accidental release is impossible, break when the rig provides the appropriate set down weight of 18 metric tons thereby releasing the canisters. Special grease is inserted into the canister's fishing neck, to ensure that retrieval is possible using the same method. This study did not go into the details of time or cost for this process. Figure 2-7 presents an engineering design drawing of the proposed canister emplacement mechanisms.

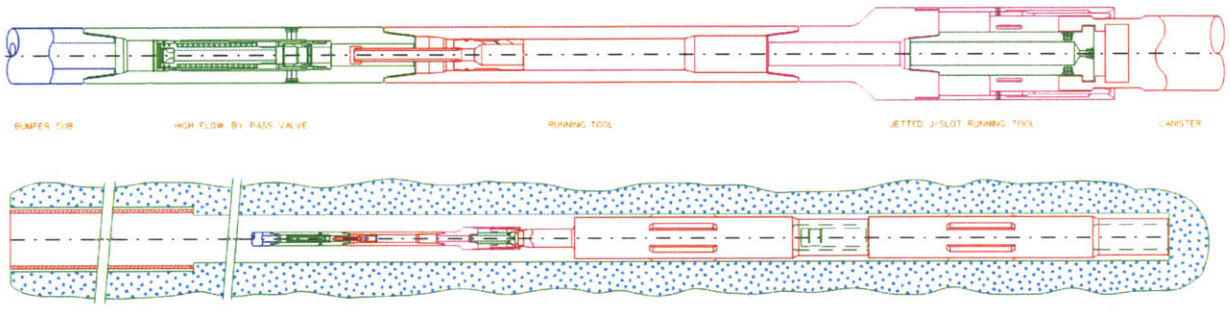

Figure 2-7. Schematic of canister emplacement tools described by SKB's engineering feasibility study[29]. The lower drawing depicts two canisters with longitudinal fins attached to each other.

2.3.2. MIT Emplacement Method Issue- Structural

Evaluations completed at MIT [12],[17], consistent with oil and natural gas experience and previous investigations of DBWD [30] , suggested the use of steel cables to lower canisters into the borehole. The theses assume that all 400 canisters would be connected and lowered as a single 2 km drill string, and this results in small loading times for each lateral (<50 days), compared to SKB's estimates for an equivalent length of waste emplacement. Additional engineering margins and structural issues involved for this technique may be an issue. For example, assuming the canisters are connected via threaded connections (as drill string sections typically are) the tensile stresses calculated in Gibb's thesis [17] do not take into account stress

concentration factors in fittings. Considerable research has been conducted on the stress concentration profiles resulting in drill string connections, because failure of borehole casings is extremely risky and costly to the oil industry[31]-[34]. The studies report that 80% of accidents and failures occur from the stresses in the threaded region, and highlight it as the weakest point in oil tubing and casing. The analyses indicate maximum stress concentration factors (SCF) under axial loading vary within a range of 3.29 to 8.56, depending on the pin or box thread profile. Figure 2-8 displays the standard thread profiles of interest and depicts the distribution of stresses.

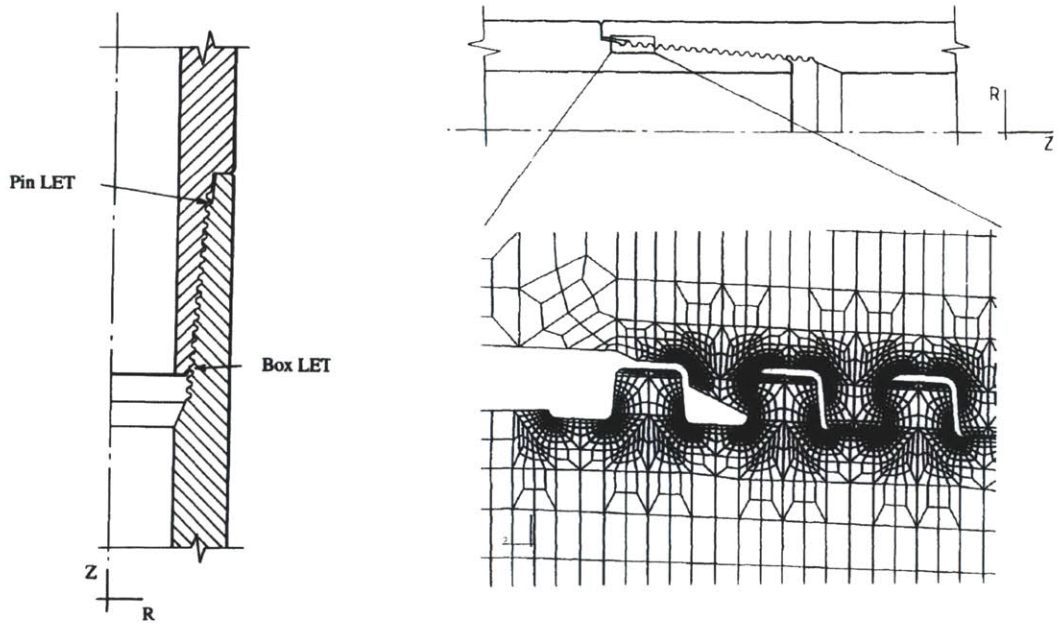

Figure 2-8. Cross sectional diagram of a standard drill string threaded connection and finite element analysis (FEA) model of stress distribution [31].

Another variable determining the failure of the threads is the torque sustained by the connection of pipes, a scenario analyzed in Figure 2-9.

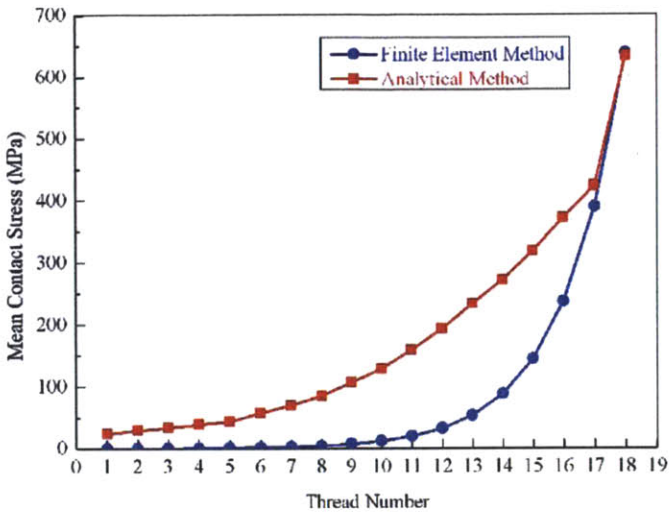

Figure 2-9. Depiction of mean contact stresses experienced by individual pipe threads. Obtained by analytical and finite element analysis in ANSYS models of an American Petroleum Institute (API) 88.9 mm round threaded drillstring connection [34].

Note that at higher thread numbers, the mean contact stress exceeds the minimum yield strength of the most API steels, resulting in partial deflection of the innermost threads. Table 2-7 presents the material properties of standardized steels used in oil wells.

Table 2-7. API Steel Specifications [35]

Grade	Minimum Yield Strength (MPa)	Minimum Tensile Strength (MPa)
H40	276	414
J55	380	520
K55	380	655
N80	550	690
L80	550	655
C90	620	690
T95	655	725
P110	760	860

Other SCF's to consider result from the welding of lids to the canisters [36][37]. The process of welding the metal container to maintain a seal is required for any repository canister design, and furthermore, residual stresses can result from the differential cooling of the welded metals. Overall, SCF's from joints, welds and additional thermal stresses all contribute to reduce the

maximum theoretical length of a waste string based on tensile stress. These SCF's on the threaded connections would also apply when calculating the crushing strength or compression limits of the waste canister column, a significant and limiting factor in the deep borehole canister design (it was one of the initial motivations for the Gibb's multi branch design) [17].

2.3.3. MIT Emplacement Method Issue- Speed

Emplacement of canisters requires three steps –loading, lowering and retrieval of the string- each of which can occur at different speeds. The process of loading a canister is similar to loading or attaching a drill bit, which could in theory occur quite quickly given the expertise the oil industry has developed. However, the difficulty of dealing with the radiation fields and heat production should not be underestimated. Gibbs' thesis on multi-branch boreholes assumes a loading rate of 5 canisters/hour, waste lowering speed of 175 m/hr (0.04861 m/s) and a retrieval speed of 350 m/hr (0.08466 m/s) [17], and serves as a lower bound estimate for the winch speed of waste deployment. An upper bound estimate for the speed assumes that individual canisters can be lowered as fast as a high capacity deep ocean winch, which operates at approximately 2 m/s [38]. A summary of estimates for the waste canister trip times based on assumed winch speeds is shown in Table 2-8, while estimates for the billing rates are shown in Table 2-9.

Table 2-8. Summary of trip times calculated for varying assumptions of the possible lowering speed of a single canister to an average depth of 3 km.

Assumption Description	Comments	Lowering Speed	Retrieval Speed	Lowering trip time	Retrieval trip time	Round trip time
Lower bound on speed	Lowering speed of canister string assumed in Gibbs' multibranch thesis [17]	0.04861 m/s (574 ft/hr)	0.0972 m/s (1148 ft/hr)	17.14 hrs	8.57 hrs	25.71 hrs
Median estimate on speed	Lowering speed of drill string segments, used by Sandia in an EGS drilling study [9]	0.08466 m/s (1000 ft/hr)	0.08466 m/s (1000 ft/hr)	9.84 hrs	9.84 hrs	19.68 hrs
Upper bound on speed	Typical Ocean winch [38]	2.0 m/s (4.47 mph)	2.0 m/s (4.47 mph)	0.416 hrs (25 min)	0.416 hrs (25 min)	0.833 hrs (50 min)

Table 2-9. Estimated billing rates during the emplacement process, assuming an 8 hr work day.

Source	Descriptions	Billing rate	Billing rate
Multi-branch borehole emplacement[17]	Billing rate (emplacement)	$4,830/hr	$38,640/day
Multi-branch borehole emplacement[17]	Billing rate (emplacement, while waste is at surface being loaded and radiation worker supervision is required)	$10,500/hr	$84,000/day
SKB 1989 VDH assessment[23]	Billing rate of original drill rig plus fuel cost.	$1,556/hr (year 1989 dollars) -$3,469/hr*	$12,445/day (year 1989 dollars) -$27,750/day*
SKB 2000 VDH assessment[29]	Billing rate of rig	-$6,257/hr*	-$50,063/day*

*(adjusted to present costs using MITDD, Table 2-4)

Overall, the billing rates lie in the range of $3,469/hr to $6,257/hr for normal emplacement operations. The average value of the three estimates is $4,852/hr. Gibbs assumes that a billing rate of $10,500/hr is appropriate during loading of the canister onto the drill string, which requires additional radiation worker supervision. The total time and cost, combining assumed loading times, winch speeds and billing rates are shown in Table 2-10.

Table 2-10. Summary of total loading times and costs for 400 canisters loaded per hole, with an average value billing rate of $4,852/hr and a 10 minute loading period (with radiation worker billing rate of $10,500/hr) for each canister.

Assumption Description	Total trip time	Total time loading of canisters onto rig	Radiation worker labor loading cost	Total Trip Cost ($M)	Total cost ($M)	Cost/kg HM emplaced ($/kg HM)
Lower Bound (of lowering speed)	10268 hrs	66 hrs	$700,000	50.237	50.937	$254.68
Median estimate (of lowering speed)	7874 hrs	66 hrs	$700,000	38.53	39.23	$196.1
Upper Bound (of lowering speed)	333 hrs	66 hrs	$700,000	1.94	2.64	$13.20

With the upper bound winch speed of 2.0 m/s, a one-at-a-time approach could require as little as 400 hours to lower 400 canisters into a single borehole. However, the single canister approach may also take as long as 10,353 hours, which when divided by 8 hours for a single work day, is 1285 work days. Using the average value billing rate, the operational cost of loading a single borehole in this fashion is between $2.64 million and $50.9 million. Even with a conservatively high winch speed, the emplacement cost is still the same order of magnitude as the drilling costs. Dividing the operation cost by the total waste contained in a borehole, the deployment stage cost per unit mass is approximately $13-$254/kg of heavy metal (HM). In total, a single crane would take 11-472 years to stack canisters in all 400 boreholes needed for an 80,000 MTHM capacity repository.

Alternatively, conservatively assume that 20 waste canisters could be connected and disregard the structural and handling difficulties associated with a 100 meter tall, 40 metric ton radioactive column. When lowered as a single drill-string segment (at the lower bound and median speeds, appropriate for drill strings) the total operational loading cost is still on the order of millions of dollars, as shown in Table 2-11.

Table 2-11. Summary of total loading times and costs for 400 canisters loaded per hole, with 20 canisters connected and lowered together. Assumes the average value billing rate of $4,852/hr and a 10 minute connection period (with radiation worker billing rate of $10,500/hr) for each canister.

Assumption Description	Total trip time	Total time loading of canisters onto rig	Radiation worker labor loading cost	Total Trip Cost ($M)	Total cost ($M)	Cost/kg HM emplaced ($/kg HM)
Lower Bound (of lowering speed)	514 hrs	66 hrs	$700,000	2.49	3.1957	$15.97
Median estimate (of lowering speed)	393 hrs	66 hrs	$700,000	1.9105	2.6105	$13.05

Figure 2-10 compiles the total cost information from Table 2-10 and Table 2-11 and presents it in bar graph form.

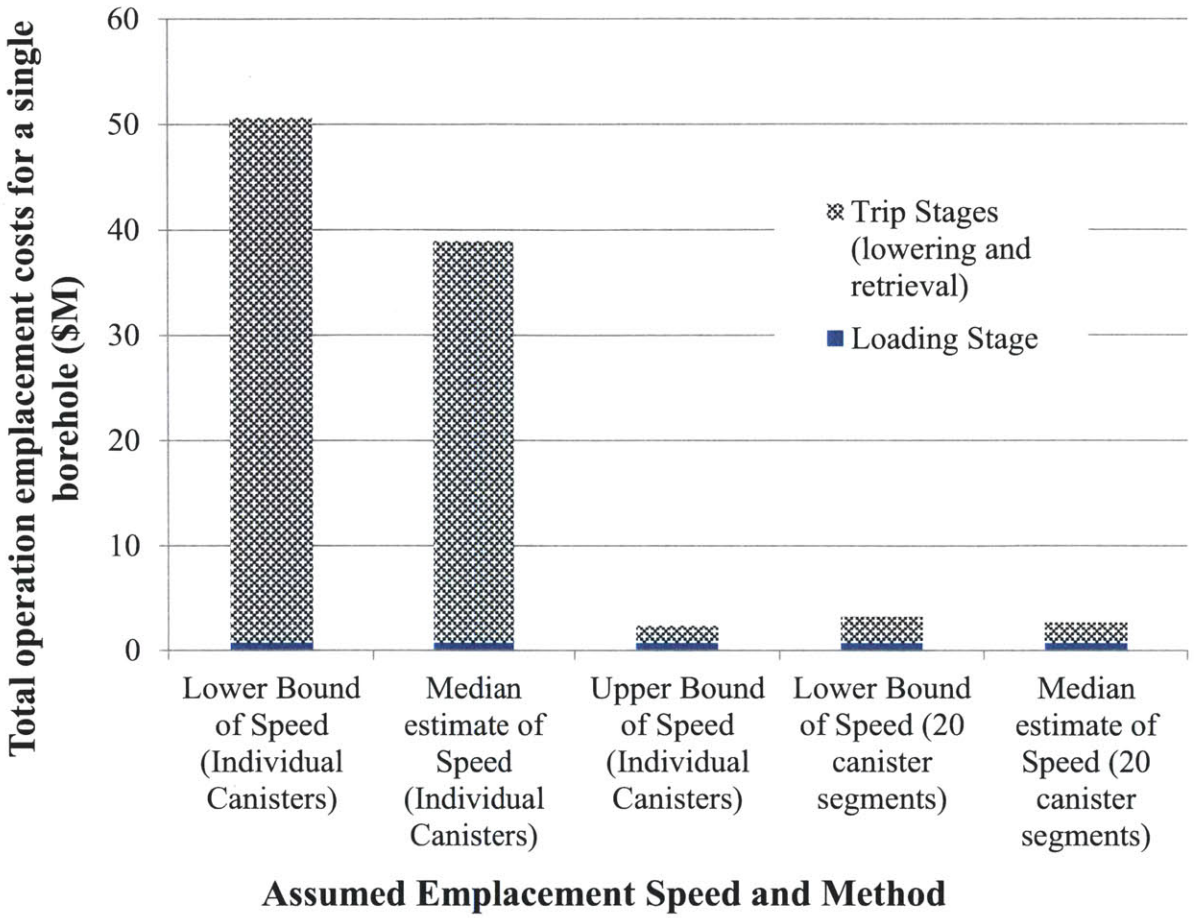

Figure 2-10. Overview of total emplacement costs ($M) calculated using various assumptions on the lowering speed and number of canisters connected.

The conclusion from analyzing the various methods is that 2-3 million dollars is a minimum loading cost for a borehole, using optimistic assumptions for either the lowering speed or capability to connect canisters. If interconnection of canisters is not feasible, and winch speeds are typical of current drill rigs, the costs are increased by an order of magnitude. These costs are similar to those calculated by SKB, which assumed a deployment period of 365 days and a minimum deployment cost of $11.8 million (1989 $). When this cost is converted to present dollars using the extrapolated drilling index, it becomes $26.31 million.

2.4. Chapter Summary

The challenges faced when designing an emplacement method for nuclear waste are exemplified by the well documented cases of the Yucca mountain repository and SKB's borehole repository, which are discussed in terms of methods, costs, equipment and logistics. The cost of emplacement is highly dependent on the billing rate ($/unit time), and a comparison of three studies is made to obtain an average billing rate of $4,852/hr, for a typical drill rig used during deep borehole operations. To accurately convert the cost estimates from the comprehensive- but decades old- SKB feasibility studies on VDH, an extrapolated drilling cost index is developed. A critical analysis is completed on the structural and time issues inherent in a drill string method for lowering waste into boreholes. The costs for the drill string method are estimated to be on the order of millions to tens millions of dollars, the same as drilling costs which have recently been focused on as a dominating factor borehole repository economics.

3. Proposed Emplacement Method

3.1. Chapter Introduction

Economics and safety are the two primary driving forces in the nuclear industry. As a result, it is desirable to reduce the cost, complexity and number of components needed for the emplacement system to operate reliably. A recent study suggested that the DBWD could provide a significant cost reduction over currently accepted disposal strategies (mined repositories), from reduced operation and emplacement costs [13]. This study attempts to improve the expense, speed and safety of the DBWD program by proposing a much less complex rig and process for the deployment stage.

3.2. Drop-in Method Description

The suggested alternative is fundamentally simple- fill the borehole with water, line up the canister above the column of water, and release the canister in a controlled manner. Water is suggested as a fluid because it is cost effective, abundant, non-toxic, and simple to transport and dispose. Additionally, it is transparent, which allows for the use of cameras (with a light source) for down-hole inspections and operations. Overall the method is suited to a vertical, fully-lined borehole where the diameter and direction of the hole and canister are constant. The certainty in geometric and hydraulic parameters provides certainty in the passively determined drag forces and thus velocity. As a precaution, an unfueled/waste-free canister which reports its velocity and location could be dropped first, to ensure that the borehole has been lined correctly and there are no unexpected angles or obstructions. This confirmation could also be achieved by lowering a wired camera, radar or other measurement device to manually inspect the integrity of the borehole lining. Based on drilling experience, the directional accuracy of the borehole lining is not expected to be an issue. For example, when the KTB borehole- drilled in Germany- reached a depth of 7.5 km, the borehole had only deviated from its original axis by 12 meters [39].

3.3. Reference Canister Design

The optimal canister and borehole design is a function of many factors, such as the cost of drilling, cost of materials, structural factors, corrosion issues, and plug and granite composition and performance. Although the factors involving cost have been estimated and discussed

numerous times previously, the remaining issues require significant research for a borehole design to be finalized. As a starting point upon which to test the feasibility of the drop-in concept, the canister design for a vertical borehole was taken from Hoag's MIT thesis [12]. Sandia National Lab's (SNL) investigation of deep borehole cost and performance also uses Hoag's design as a reference [13]. The most relevant properties of the design are depicted in Figure 3-1.

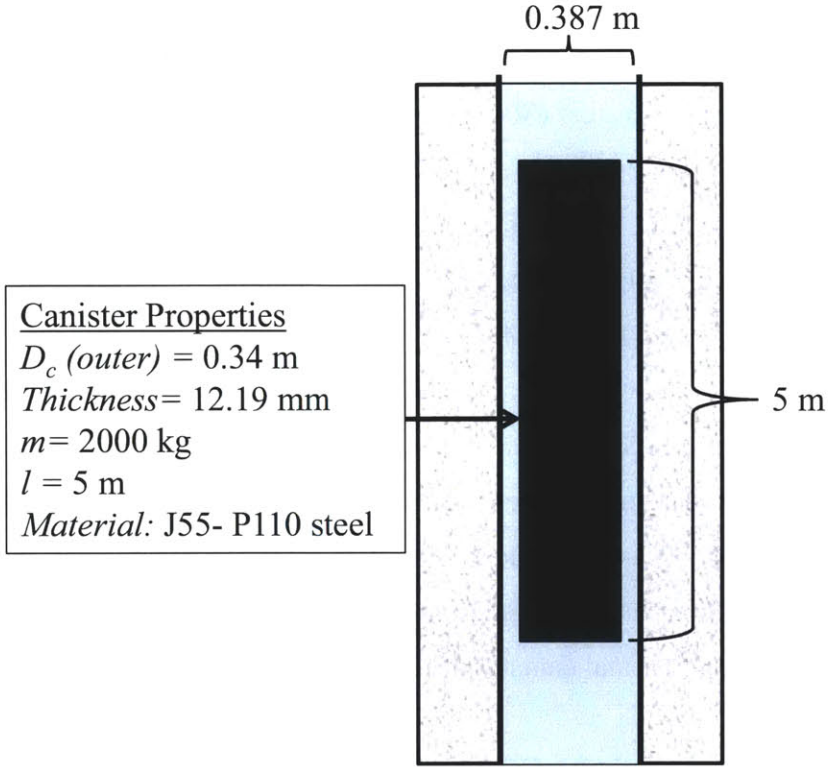

Figure 3-1. Cross sectional view of the proposed emplacement method, based on Hoag's design for the pipe lining and canister dimensions [12] Not to scale. Note that the gap between the canister and the lining is an annulus with a thickness of 2.35 cm.

Hoag's design is based on structural, thermal and other geometric criteria to comply with oil and nuclear industry standards. Firstly, the diameter of the canister was chosen to be the minimum diameter standard oil casing that would fit a 303mm diagonally wide, fully intact PWR assembly. The length is not a limiting factor, and a standard oilfield casing is assumed to be cut in half to be 5 meters long (to contain a 4.059 m or 4.476 m long PWR or BWR assembly, respectively). The constituents and their masses are summarized in Table 3-1.

Table 3-1. Reference borehole canister components and masses [12]

Component	Description	Mass
Spent Fuel	PWR assembly	600-700 kg (of which 500 kg is heavy metal)
Fill particles	Silicon carbide for crushing resistance	600-700 kg
Casing and lids	P110 (API) steel	700 kg
Total		**2000 kg**

To ensure interim retrievability and waste containment within the canister (at least during the emplacement phase), the structural limits of the canister must be analyzed. The bottom canister in the 2 km column of waste canisters (800 MT) experiences substantial axial compressive stresses and hydrostatic pressures. Hoag and Gibbs suggested that filler material such as silicon carbide particles be inserted into the canister prior to sealing, improving crushing resistance (and heat transfer), but further investigations would need to experimentally verify this [12],[17]. More recently, Driscoll has suggested the use of a cast iron insert within the same diameter casing [40]. Although each canister would be significantly heavier (3600 kg, including interstitial sand) the bottom-most canister would experience an axial compressive stress of 260 MPa, which is a factor of two to three less than the reported yield and tensile strength of ASTM A339 and A395 steels. Future investigations may continue to modify the canister design because of the tradeoff that occurs between cost, corrosion resistance and strength of canister materials. In the face of uncertainty with regards to the final canister design, Hoag's design is used as the reference.

3.4. Suggested Handling Procedure

First, at a centralized facility, assemblies must be unloaded from arriving transportation casks and loaded individually into DWBD canisters (a process that typically is completed underwater for radiation protection). The canister would then be filled with interstitial particles (for crush resistance) and/or a cover gas such as helium to increase heat transfer and reduce corrosion. Finally the lids are welded shut and inspected through non-destructive evaluation techniques (NDE) [41]. Overall the initial cask loading process would very similar to that of the Yucca mountain repository. A depiction of the Yucca mountain canister loading and welding facility is shown in Figure 3-2.

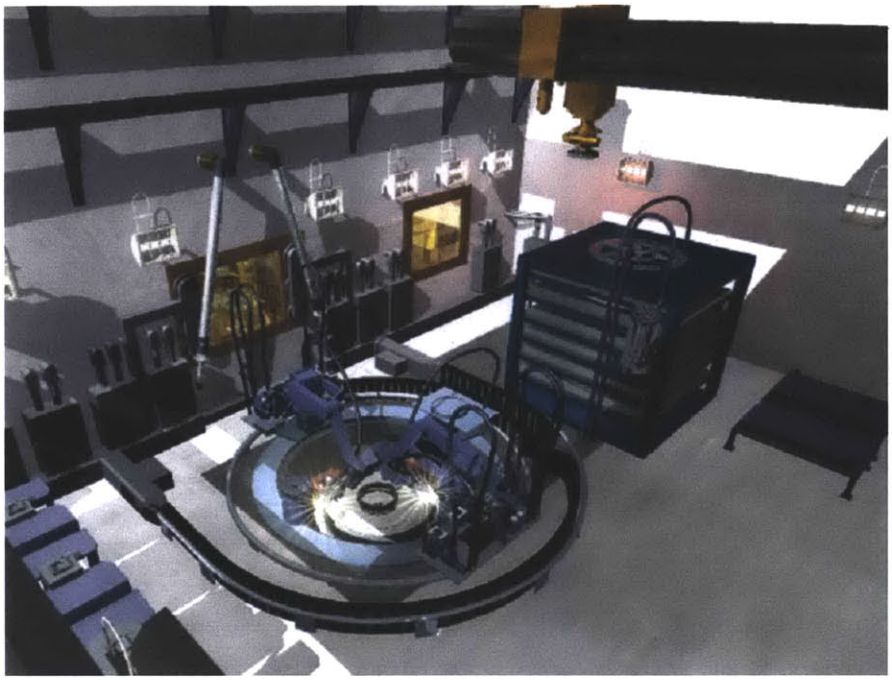

Figure 3-2. An illustration of the Yucca Mountain waste package closure system, robotically welding a waste package lid in place [41]

After sealing and inspection, the waste canister must be transferred into a shielded cask, for safe transportation from the central facility to the borehole for emplacement. The shielding cask is further discussed in Section 6.2. Transferring the cask to the borehole requires a remote controlled truck (preferred) or rail machine, capable of maneuvering a shielded concrete cask. The design could borrow from the Yucca mountain rail transporter shown in Figure 2-2 or other vertical emplacement gantries suggested for shallow mined repositories. In this case the cask will be lighter and easier to handle because it only contains a single assembly (~10 vs. 50 metric tons). Instead of having a separate emplacement gantry to lower the waste, the two machines can be integrated to save time and reduce complexity. Compared to the originally proposed drilling rig, a drop-in concept rig will be relatively simple. One possible truck loading mechanism, similar to a vertical emplacement method proposed for salt repositories [42], is depicted in Figure 3-3, Figure 3-4, and Figure 3-5.

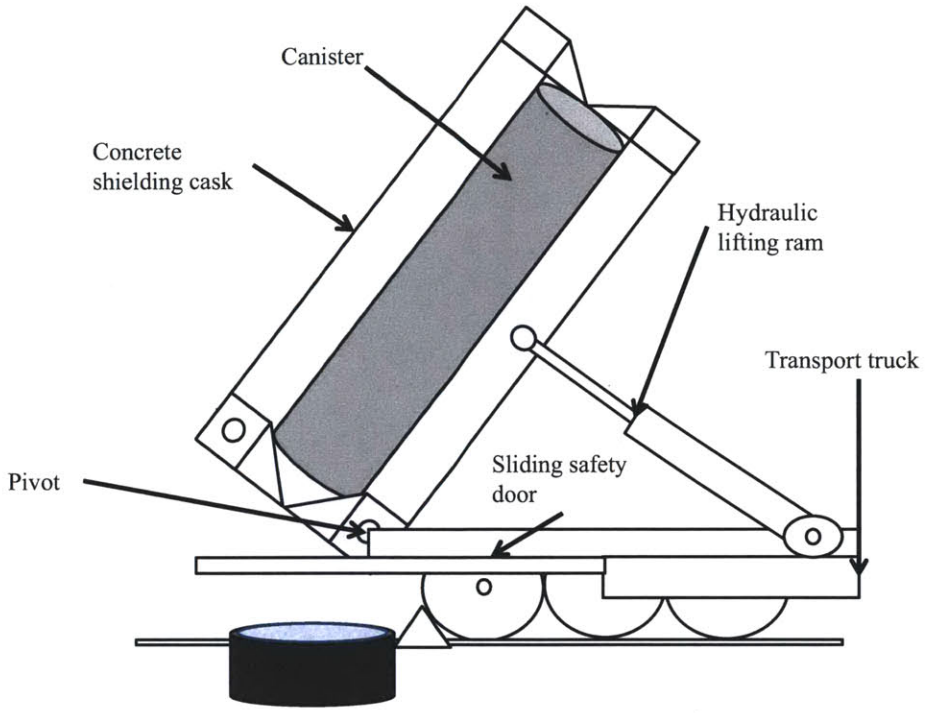

Figure 3-3. Diagram of the lifting step of a proposed emplacement method.

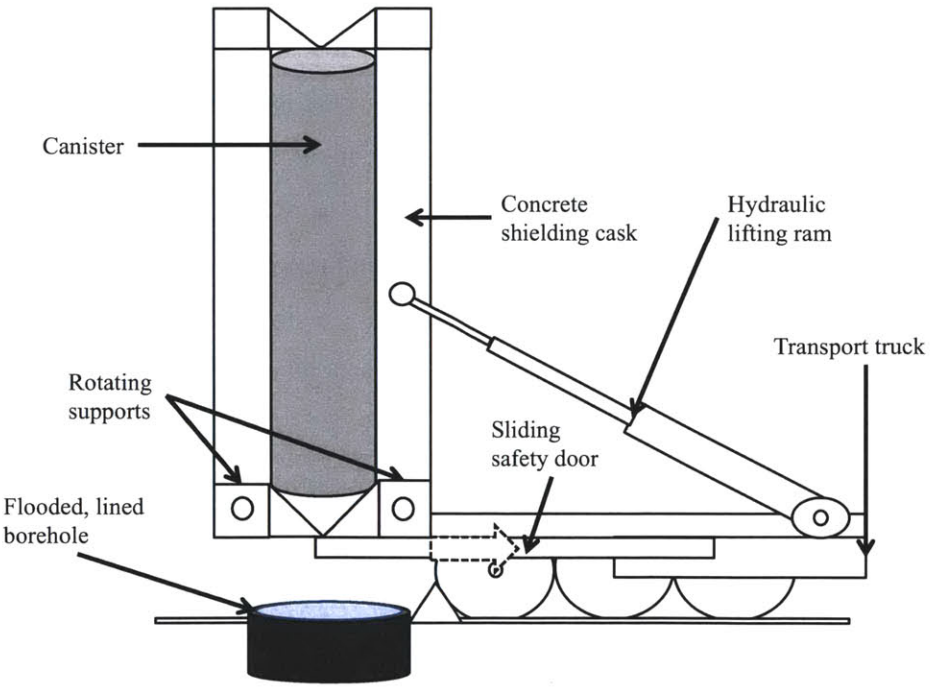

Figure 3-4. Diagram of intermediate step of a proposed emplacement method.

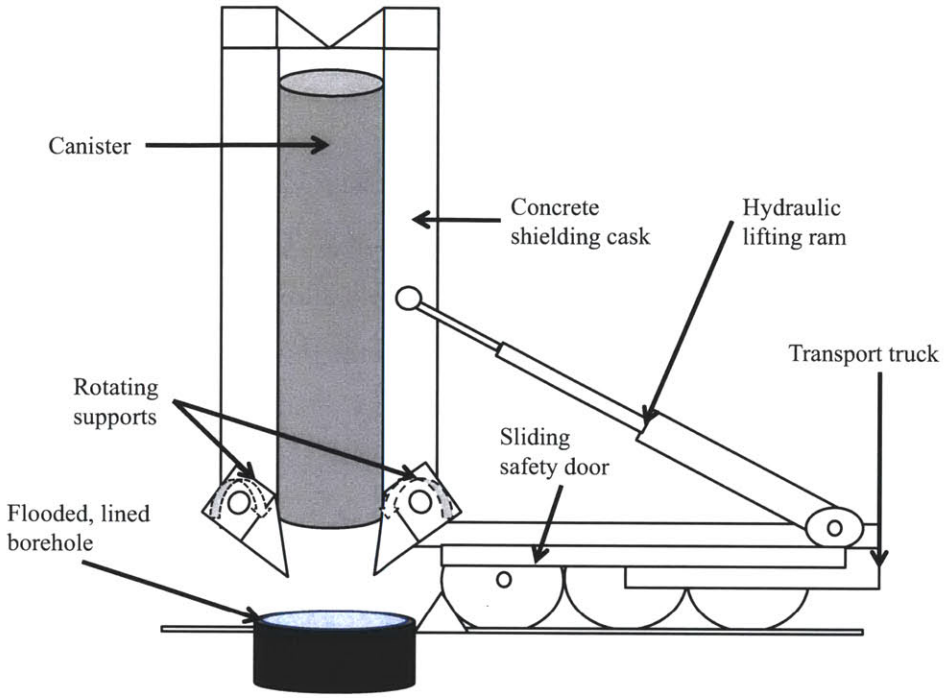

Figure 3-5. Diagram of the final lowering step of a proposed emplacement method.

As the canister is lifted up from the transporter bed, a safety door beneath the concrete cask serves as an extra layer of safety preventing accidental release of the canister. After the cask is fully lifted and lined up above the borehole, the sliding safety door begins to retract, and the supports that hold the canister within the cask begin to rotate. The rotating support system is also a redundantly safe system, because if one side of the support fails (releases completely), the other support maintains the canister within the cask, and is still capable of lowering it in a controlled fashion.

3.5. Chapter Summary

This study is motivated by a desire to reduce radiation handling requirements and expedite the repository emplacement process for nuclear waste. A simple drop-in method is proposed, and in the face of uncertainty regarding the optimal borehole canister design, a reference canister design is chosen for analysis. Finally, an emplacement mechanism for transporting and releasing the canisters with shielding is proposed. The design keeps a strong emphasis on redundant or passively safety features to prevent accidental drops, and is feasible with current technology.

4. Analytical Modeling of Proposed Emplacement Method

4.1. Chapter Introduction

A main goal of this study was to demonstrate that the canister will reach a safe terminal velocity and that the impact will not damage the canister significantly. The nature of the problem (steady state fluid flow) lends itself to an analytical solution, which allows for much better understanding of the important variables, compared to numerical modeling. Furthermore an analytical solution improves the design process of experiments and scalability of additional safety features, such as drag inducing components. This chapter outlines the approach and simplifying assumptions made in deriving a closed form solution of the canister velocity.

4.2.Assumptions and Equations

The analytic model is based on solving force balance and momentum equations, assuming steady state, incompressible fluid flow. A force balance diagram is depicted in Figure 4-1.

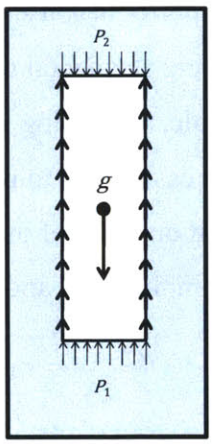

Figure 4-1. Depiction of gravitational, shear and pressure based forces that act on the canister as it falls at terminal velocity.

The force balance on the canister can be written as Eq. (4-1)

$$P_1 - P_2 = \rho_C g l - \frac{\rho_f V_f^{\,2}}{2} f\left(\frac{l}{D_C}\right) \tag{4-1}$$

where P_1 is the liquid pressure acting on the top surface of the canister, P_2 is the liquid pressure acting on the bottom surface of the canister, ρ_c is the density of the canister, ρ_f is the density of the fluid, V_f is the average fluid velocity, g is the gravitational constant, f is the friction factor, l is the length of the canister and D_c is the diameter of the canister. The momentum equation for the fluid, taking into account form and frictional pressure drops, is written as Eq.(4-2),

$$P_1 - P_2 = \frac{\rho_f {V_f}^2}{2}\left(f\frac{l}{D_h} + K_{form}\right) + \rho_f g l \tag{4-2}$$

where K_{form} is the form loss coefficient associated with the flow geometry, D_h is the hydraulic diameter (equivalent to twice the size of the annular gap).

4.2.1. Closed Boundary Condition

In this expected condition, the volume of the water beneath the canister was assumed to be constrained (and unable to flow in any direction besides through the annulus). In addition, the water was considered to be incompressible. Therefore, as the canister moves downwards, the water volume it displaces will be forced to flow through the annulus. The continuity relation yields Eq. (4-3) (see Appendix A.3),

$$\frac{V_f}{V_C} = \frac{{D_C}^2}{D_h(2D_C + D_h)} = V_{ratio} \tag{4-3}$$

where V_f and V_c are the magnitudes of the canister and fluid velocities, respectively. For Hoag's canister design [12], V_{ratio} is approximately 3.4 (the ratio of the average velocity of the fluid in the annulus to the velocity of the canister is 3.4). However, the fluid travels in the opposite direction of the canister. The relative velocity of the fluid to the canister surface is greater than the fluid's velocity in the stationary frame of reference. If the latter were assumed as the velocity of the water in the gap, it would significantly underestimate the frictional forces on the canister. To take this into account, the reference frame is shifted by a constant velocity, such that the velocity of the canister in the new reference frame is zero. This is acceptable because the standard momentum, continuity and energy equations apply in any frame of reference, as long as

the frame is not accelerating. The calculation of the friction factor in the annulus will be slightly overestimated in this frame of reference, because the outer pipe has a small velocity that is in the same direction as the water flowing in it. No correlation could be found that describes the friction factor in an annulus with a moving boundary. By intuition, it is postulated that most of the shearing will occur near the surface of the canister, and thus it is more important to accurately model that phenomena/region. Furthermore, the experimental data will support or disprove this simplifying assumption. Eliminating P_1 - P_2 from Eqs. (4-1), (4-2) and (4-3), (see Appendix A.3) the expression for terminal velocity for the canister in this case is Eq. (4-4):

$$V_C = \sqrt{\frac{2gl\left(\frac{\rho_c}{\rho_f} - 1\right)}{\left[f\left(\frac{l}{D_h} + \frac{l}{D_c}\right) + K_{form}\right](V_{ratio} + 1)^2}} \tag{4-4}$$

V_{ratio} depends only on geometry, and is given by Eq. (4-30). The friction factor f can be calculated using the Colebrook equation iteratively, but a closed form expression such as the Swamee-Jain correlation could alternatively be used [43]. K_{form} is the loss coefficient for a sudden contraction and sudden expansion resulting from the bottom and top edges of the canister, respectively, shown in Eq. (4-5) [44],

$$\sum K_{form} = K_{sudden\ contraction} + K_{sudden\ expansion} = 0.5 + 1 = 1.5 \tag{4-5}$$

4.2.2. Open Boundary Condition

Analysis was completed to address a potential accident scenario of the drop-in concept. This condition postulates that the bottom of the borehole is not sealed or lined properly. In this case, the volume of the water beneath the canister is assumed to be free to flow downwards (or into another volume besides the borehole). Therefore, as the canister moves downwards, the water displaced by the canister is not forced to flow through the annulus. This scenario is practically impossible for at least two reasons: (i) a massive rupture of the borehole lining is extremely unlikely, and (ii) there is no large free volume available for water displacement in granite. Despite this the scenario was still analyzed as a bounding case. Here, there is no simple

relationship between V_c and V_w. In this situation, analysis of the boundary layer and velocity distributions are critical to understanding the shear forces on the canister. If the boundary layer is small compared to the actual gap, then the solution can be approximated by estimating the canister's velocity in a large pool of water. Under these conditions of external flow, the canister terminal velocity can be derived by using its coefficient of drag, approximately 1 for this case [44], and force balance, which gives Eq. (4-6) (see Appendix A.4 for derivation),

$$V_c = \sqrt{2gl\left(\frac{\rho_c}{\rho_f} - 1\right)} \tag{4-6}$$

Plugging in the values from the reference canister design [12], a physically feasible canister terminal velocity of 18.3 m/s was obtained, with a Re_{axial} of 6.6 x 10^6. The maximum size of the boundary layer is calculated using Eq. (4-7) [43],

$$\delta = 0.16l(Re_{axial})^{-1/7} = 8.49\ cm \tag{4-7}$$

In this case, the boundary layer is nearly 4 times larger than the actual gap that it is constrained to fit in. Therefore, the assumption of external flow is not valid, and can only be used to obtain an upper bound estimate of the canister velocity. In reality, viscous effects in the boundary are more important because the boundary layer is forced to fit in such a small gap.

The most accurate approach estimated the velocity distribution in the gap using Von Karman's Universal Law [43]. Using the no-slip boundary condition, the velocity was constrained to be a maximum (and equal to V_c) at the surface of the canister, and zero at the outer lining diameter. With this approximate velocity distribution, a friction factor for flow in the annulus was derived (see Appendix A.4) to be Eq. (4-8),

$$\sqrt{\frac{1}{f}} = 0.8626\ln\left(\mathrm{Re}\sqrt{f}\right) - 0.588 \tag{4-8}$$

Combining Eq. (4-8) with the approximated velocity distribution and force balance expressions, Eq. (4-1) and Eq. (4-2), gives Eq. (4-9),

$$V_c = (1 + 0.8626\sqrt{f}) \sqrt{\frac{2gl\left(\frac{\rho_c}{\rho_f} - 1\right)}{\left(f\left(\frac{l}{D_h} + \frac{l}{D_c}\right) + K_{form}\right)}} \tag{4-9}$$

4.3. Discussion of Solutions

For the closed boundary condition, substituting the reference canister properties into Eq. (4-4) and using surface water conditions yielded a modest canister velocity of 2.37 m/s. The friction factor f was calculated iteratively using the Colebrook correlation [43] to be 1.30 x 10^{-2}. K_{form} was calculated from tables [44] to be 1.5 (as the canister causes a sudden contraction and expansion of the flowing fluid). Assuming a granite and water temperature of 120° C at the bottom of the borehole (hydrostatic pressure prevents boiling), the estimate for the terminal velocity rises slightly to 2.6 m/s. Overall, this approach is conservative because the friction factor was calculated assuming the canister and pipe are hydraulically smooth.

For the open boundary condition, using the reference canister design and iteratively solving Eq. (4-9) gives a canister velocity of 11.51 m/s. The terminal velocity in this extremely conservative bounding case can be put into perspective by considering the fact that the same velocity would be achieved if the canister was dropped in air from a height of only 6.75 meters (only 20% longer than the total length of the canister). In reality, the canisters, which are designed to withstand very high compressive stresses, will be engineered to sustain such velocities, in case of accidental drop during transportation (see Section 6.3 for more analysis).

4.4. Dimensional Analysis

Scaling of fluid dynamics phenomena involved in the canister free fall is needed for the design and interpretation of the experiments described in the next chapter. Scaling must be based on dimensional analysis to ensure that it simulates the fluid flow of an actual borehole as closely as possible. The relevant design variables were found from inspection of Eq. (4-4) and Eq. (4-9) and are presented in Table 4-1 and graphically depicted in Figure 4-2.

Table 4-1. Definition of all relevant variables and their respective dimensions, where M stands for Mass, L stands for Length, and T stands for Time.

Abbreviation	Description of Variable	Dimensions
D_c	Diameter of Canister	L
t	Gap Thickness	L
D_h	Hydraulic Diameter*	L
l	Length of Canister	L
ρ_c	Density of Canister	$M/(L^3)$
ρ_f	Density of Fluid	$M/(L^3)$
μ	Viscosity of Fluid	$M/(LT)$
g	Gravitational Constant	L/T^2
ε	Surface Roughness	L
V_f	Velocity of Fluid	L/T

**Note that the Hydraulic Diameter for a concentric annulus is equivalent to $2t$.*

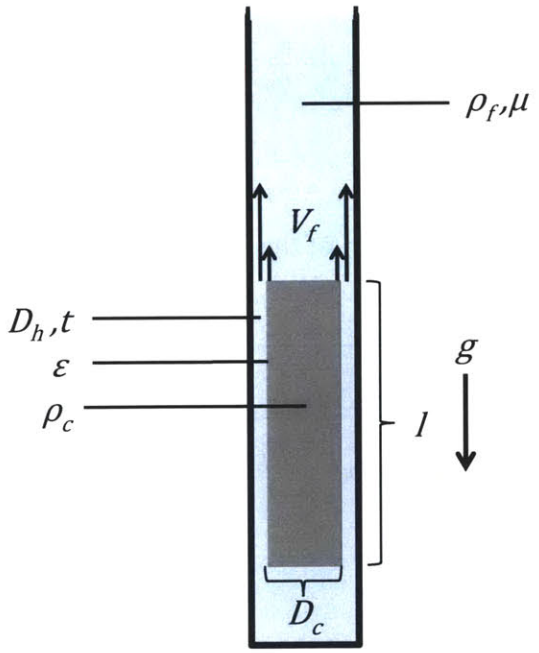

Figure 4-2. Diagram of all variables required to calculate the terminal velocity of the canister falling in a pipe of fluid. Variables are defined in Table 4-1.

Since there are 8 independent variables and 3 dimensions, there are 5 dimensionless parameters that describe the system. They are the Reynolds number (Re), which implicitly represents the velocity of the canister, and thus is the dependent variable,

$$Re = \frac{\rho_f V_f D_h}{\mu} \tag{4-10}$$

the geometric and material property ratios,

$$\frac{\varepsilon}{D_h}, \frac{l}{D_h}, \frac{D_c}{D_h}, \tag{4-11}$$

and the Archimedes number (*Ar)* which captures the buoyancy effects,

$$Ar = \frac{\rho_f(\rho_c - \rho_f)gD_h{}^3}{\mu^2} \tag{4-12}$$

Then the Buckingham Pi Theorem ensures the functional dependence captured by Eq. (4-13),

$$Re=f\left(Ar, \frac{\varepsilon}{D_h}, \frac{l}{D_h}, \frac{D_c}{D_h}\right) \tag{4-13}$$

Further manipulation of Eq. (4-4) (see Appendix A.5) yielded a direct confirmation of the Buckingham Pi Theorem- a dimensionless form of the solution, Eq. (4-14),

$$Re = \sqrt{\frac{Ar\left(2\frac{l}{D_h}\right)}{f\left(\frac{l}{D_h} + \frac{l}{D_c}\right) + K_{form}}} \tag{4-14}$$

4.5. Chapter Summary

Direct analytical solutions were obtained for both the expected closed and unlikely open boundary condition for the fluid. Solution of the open boundary condition involved approximating the velocity profile for the boundary layer. A dimensional analysis was also completed and verified, through further manipulation of the analytical solution into a dimensionless form. Overall the analysis makes few approximations regarding the fluid flow and reveals a remarkably simple functional form of the canister and fluid properties. The result is completely consistent with intuition that a greater difference in canister and fluid density (captured by higher values of the *Ar* number) increases canister and thus fluid velocity. The friction factor parameter (which contains surface roughness effects) and form loss coefficients directly reduce the terminal velocity of the canister.

5. Experiments

5.1. Chapter Introduction

Experimental design, setup, and execution were a large component of this study and necessary to demonstrate that the assumptions within the analytical modeling process and predictions for terminal velocity (summarized in Section 4) do not oversimplify the process. Furthermore, experiments allow for more complex investigations of drag-inducing and safety features.

5.2. Design Considerations

5.2.1. Controlled Variables

From Eq. (4-14) it is clear that the most important, controlled, independent variable is the Archimedes number (*Ar*), which is determined by the specific density of the canister, the geometric ratios, and the fluid properties. The two simplest ways to vary this are to adjust the mass of the canister and viscosity or type of the fluid. In addition to the *Ar*, the friction factor (*f*) can be increased by roughening the surface of the canister, and K_{form} can be increased by adding form losses to the fluid flow. Table 5-1 presents a summary of the controlled variables and methods for variation.

Table 5-1. Summary of independent variables for the borehole emplacement experiment.

Independent Variable	Dimensionless Group	Method of Variation
Density Ratio (Density of Canister/Density of Fluid)	*Ar*	Change the mass of canister by adding or removing lead pellets.
Viscosity of fill fluid	*Ar*	Change the fluid properties via temperature or by choosing another fluid.
Roughness of canister	*f*	Roughen the outside of the canister by attaching sandpaper.
Form losses of canister	K_{form}	Attach items which restrict fluid flow.

5.2.2. Canister Size

The experiment was initially designed to meet a number of space, cost, safety and time restrictions. Vertical space constraints (the 3 meter height of a single story of the laboratory)

were ensured by numerically integrating the force balance and momentum equations (see Appendix A.6). This gives an estimate for velocity profile and distance traveled of the scaled canister, as a function of time and verifies the assumption of steady state flow in of Eq. (4-4) and Eq. (4-14). For the purpose of cost and ease of cutting, the canister and lining was constrained to standard plastic piping dimensions. Acrylic was chosen as the material for the outer lining to allow for observation of the canister during the drop test. Since plastic piping was used, lead particles were chosen to increase the total density of the canister and compensate for the low density of plastic. The lead pellets were sealed within the plastic canister using an adjustable and removable rubber plug, so that the same canister could be used multiple times with varying amounts of lead shot. The mass of the canister had to be low enough such that it was still possible to safely lift by hand, to expedite modification, removal and transportation of the canister between tests. This limited the canister mass to approximately 15 kg. Using a total specific density of approximately 4 (the same specific density of a full scale canister) and retaining geometric similarity (l/D_c), an estimate of 1 meter was obtained for the appropriate length of the canister. The closest diameters of standard piping that could be obtained to conserve the aspect ratio (l/D_h), was a 3¼ inch outer diameter (OD) acrylic pipe to simulate the outer canister, and a 2 5/8 inch OD plastic pipe to simulate the inner canister. The dimensions of the standard pipes used are shown Table 5-2 and depicted in Figure 5-1.

Table 5-2. Summary of standard pipes and measured dimensions, (+/- 0.021 cm)

Standard Pipe description (nominal)	**Measured Outer Diameter**	**Measured Inner Diameter**	**Thickness**
2 5/8 inch (OD) Plastic Pipe- Canister	**6.69* cm** (2.635 inches)	5.662 cm (2.229 inches)	0.499 cm (0.203 inches)
3 ¼ inch (OD) cast acrylic pipe- Lining	8.279 cm (3.2595 inches)	**7.6327* cm** (3.0005 inches)	0.3175 cm (0.125 inches)

*The bolded quantities are the relevant dimensions that affect the velocity of the canister.

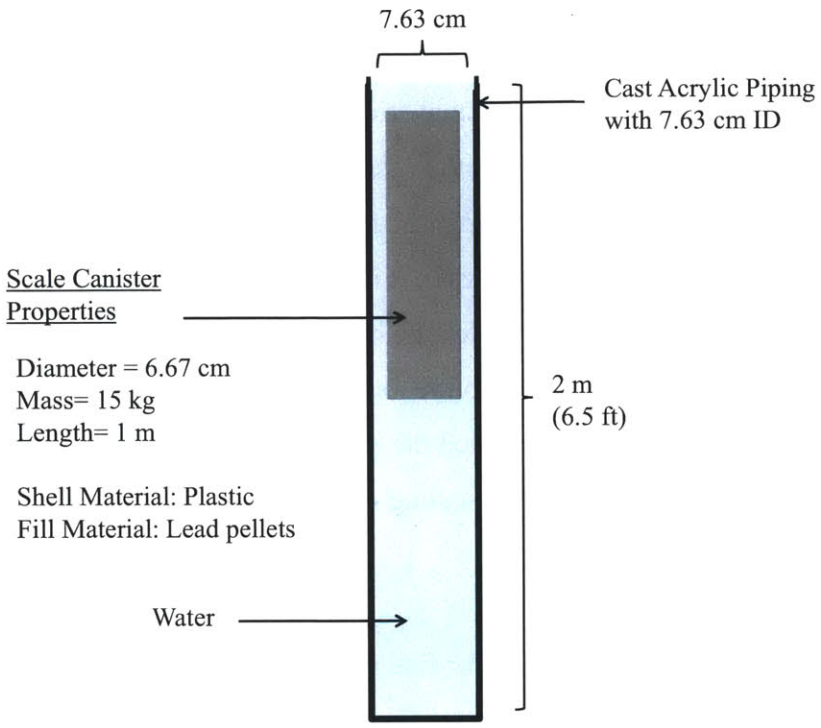

Figure 5-1. Materials and relevant dimensions of the initially designed experimental setup.

Using the dimensions provided above, an estimate for the vertical distance required was obtained and is graphed in Figure 5-2.

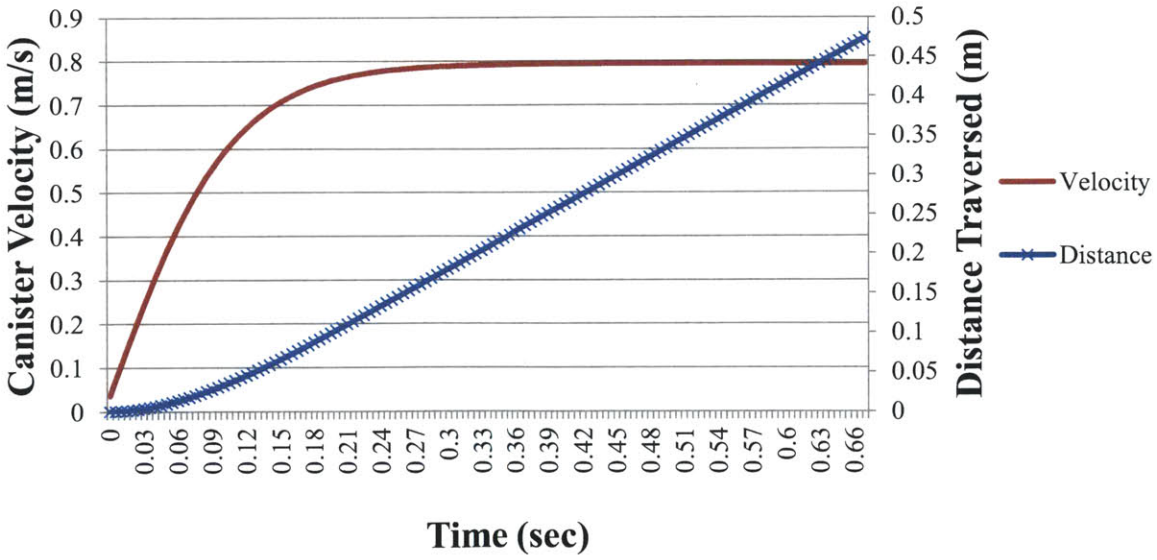

Figure 5-2. Results of numerical integration of force balance equations for a 14.79 kg canister with diameter of 0.067 m, length of 0.983 m and lining diameter of 0.07632 m dropped in water.

Notice that this canister design reaches terminal velocity quite quickly (within 0.3 seconds) and within a short distance (0.2 m). Overall, the analysis produced a lower bound on the height required, because the model assumed a constant friction factor (for ease of computation), steady state and fully developed flow, which is not the case when the canister is accelerating from rest. This is because the fluid experiences greater shear forces and higher friction factors in the developing regions and at lower Reynolds when it is accelerating [44], implying that the model would produce lower than actual estimates for the height required for terminal velocity. With a multiplicative safety factor of two applied to the total distance required to reach terminal velocity (0.4 m) , the experimental design still satisfied the initial space requirements. Overall this corresponded to an approximate geometric scaling of 5 to 1.

5.2.3. Materials and Fluids

Inspection of the *Ar* reveals that since a factor five reduction of D_h occurs, the viscosity of the fluid should be decreased by a factor 11.18 to retain complete dimensional similarity with the full scale canister. Figure 5-3 confirms that a higher *Ar* is achieved with lower viscosity fluids, and presents a comparison of the alternative fluids and their effects on the *Ar* and *Re*.

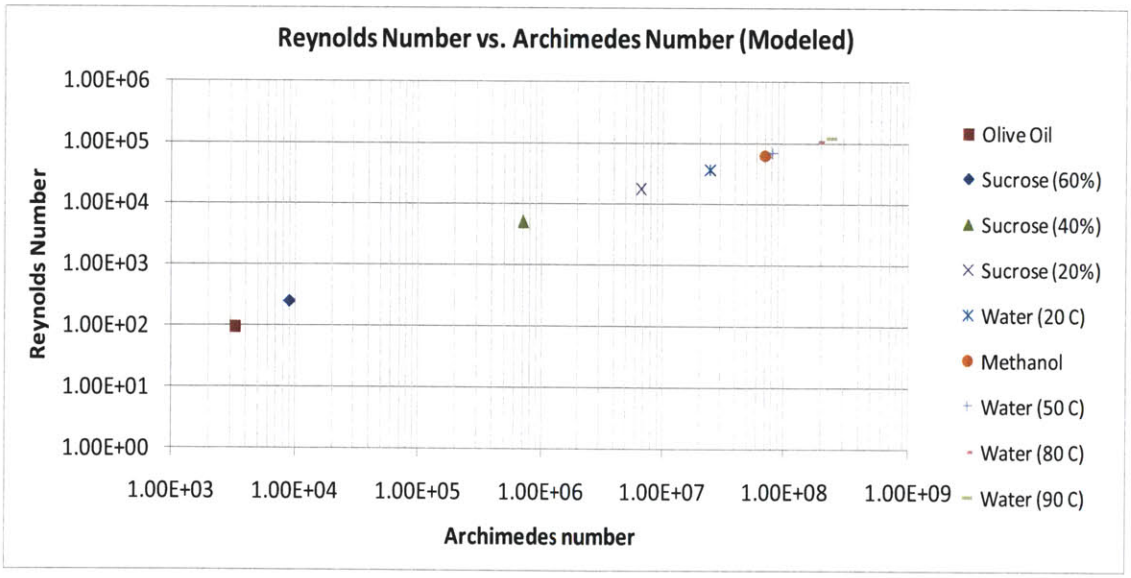

Figure 5-3. Log-log plot demonstrating of the effect of fluid choice on Archimedes and Reynolds numbers (and thus terminal velocity) for the reference, experimental scale canister.

Obtaining suitable fluids with much lower viscosities than water is difficult, especially considering that the viscosity of water can be reduced substantially simply by increasing temperature. Table 3 summarizes the comparison of fluids with lower viscosities.

Table 5-3. Comparison of alternative fluids lower viscosity than the reference case, room temperature water.

Fluid	**Relative Viscosity (Compared to 25° C water)**	**Pros**	**Cons**
60° C Water	0.475	-Cheap -Easy to clean/dispose	-Use of thermometer -Scalding hazard -Need to insulate pipe -Plastic melting/swelling
Gasoline	0.46	- Cheap	-Inhalation hazard -Flammability
Methanol	0.65		-Inhalation hazard, skin hazard -Flammability -Highly toxic if ingested -Dissolves plastics

Water was chosen as the fluid fill, and the difficulty of dealing with higher temperatures was concluded to be much less than the danger of dealing with toxic or flammable chemicals that may be incompatible with plastic (which would prevent reuse of the canister and lining).

5.2.4. Instrumentation and Procedure

The mass of the canister was determined by using a Pelouze PE5 2.2 kg capacity (+/- 0.5 g) digital scale to measure the mass of the components of the canister (each bag of lead shot, canister, end plugs) and summing them together. Velocity was measured using a light-weight nylon fishing line attached to the top of the simulated canisters and wound around a Vernier rotary motion meter's pulley. The rotational velocity of the meter was recorded using Vernier's Logger pro™ software, specifically designed for use with that rotary motion sensor. This minimized costs and post processing of data (especially compared to a conventional method of using a high speed camera) and allowed for a very high level of accuracy and repeatability. The sensor is depicted in Figure 5-4.

Figure 5-4. Photos of the Vernier rotary motion sensor used in the experiments.

The sensor and software recorded position, velocity and acceleration at a rate up to 100 hertz (1/second) within 1 degree of rotation. The middle 29 mm groove diameter was used, and this corresponds to a positional accuracy of 0.253mm.

At the start of the experiment, the canister was lifted to the surface of the water by hand using the pulley and high strength rope that was tied to the top of the canister. The canister was held at the surface for a period of 10-20 seconds to minimize the effects of upwardly flowing water that result from the lifting the canister. The rope was abruptly released and the canister was allowed to fall freely. Care was taken to ensure that the high strength rope could travel without obstruction into the pulley, to prevent jamming and reduce friction effects. The terminal velocity was calculated by determining the time interval over which velocity remained relatively constant and averaging the velocity values in said interval. Temperature (and thus viscosity) was varied by adding insulation to the pipe and beginning the experiment with >90° C water. Over the course of many hours as the temperature fell slowly, the canister was repeatedly dropped and the temperature and velocities were recorded. The low friction sensor pulley and a series of tests eliminated nylon string issues from concern (see Appendix B.5). Figure 5-5 presents the conceptual design diagram of the measurement setup, while Figure 5-6 is a labeled photo of the actual experimental setup.

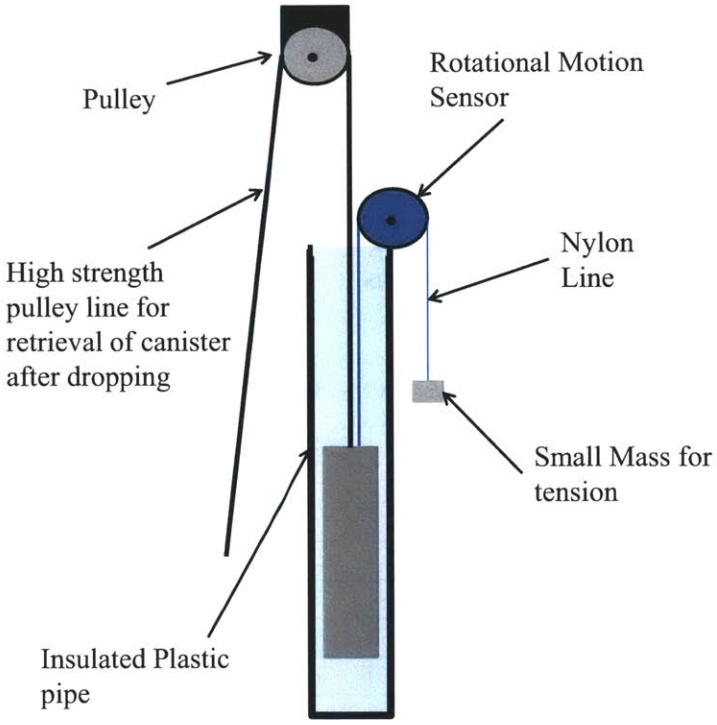

Figure 5-5. Conceptual design of the experimental setup.

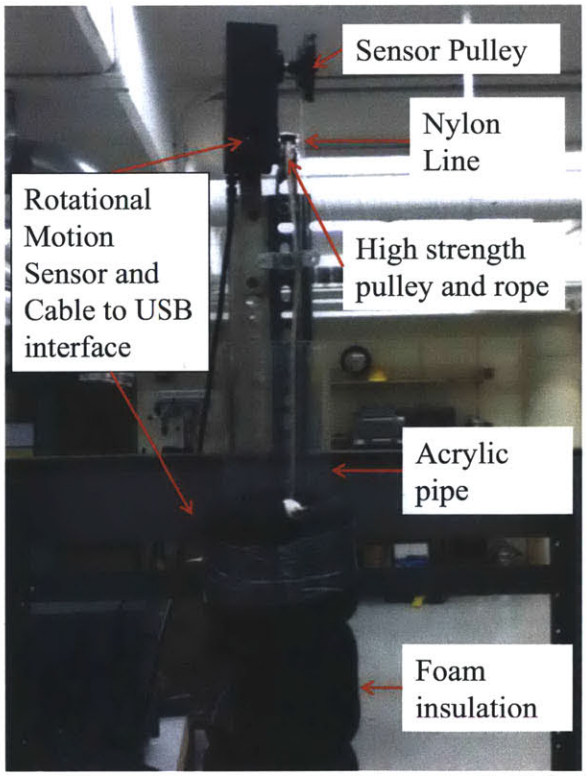

Figure 5-6. Photo of the attached pulleys, rotary motion sensor and insulated acrylic pipe.

5.3. Results

5.3.1. Dimensional Similitude of Experiment

The test facility scaled down all geometric and material parameters approximately by a factor of 5, to fit in the lab space. Table 5-4 presents a comparison of the geometric and mass parameters of the full and experimental scale canister designs.

Table 5-4. Comparison of parameters between the full scale and experimental scale canisters.

Parameter	Full Scale	Experiment
Canister Length (m)	5	0.983
Canister Diameter (m)	0.34	6.70×10^{-2}
Lining Diameter (m)	0.387	7.63×10^{-2}
Hydraulic Diameter (m)	0.047	9.22×10^{-3}
Canister Volume (m^3)	0.4539	3.465×10^{-3}
Canister Mass (kg)	2000	14.79
Canister Density (kg/m^3)	4405	4264
Surface roughness (micrometers)	46*	1.5*
Water Dynamic Viscosity (Pa-s)	1.00×10^{-3}	1.00×10^{-3}
Water Density (kg/m^3)	1000	1000

*Surface roughness parameter from [43], for smooth steel and plastic respectively.

A comparison of the dimensionless parameters is shown in Table 5-5.

Table 5-5. Dynamic similitude of experimental parameters, during tests that varied *Ar*.

Dimensionless Groups	Full Scale	Experimental
Ar	3.46×10^{9}	$1.7 \times 10^{7} - 2.5 \times 10^{8}$
$\frac{\varepsilon}{D_h}$*	9.78×10^{-4}	1.63×10^{-4}
$\frac{l}{D_h}$	106.4	106.6
$\frac{D_c}{D_h}$	7.23	7.26
$\frac{\rho_c}{\rho_f}$	4.4	2.4 – 4.3
Re, predicted using Eq. (4-14)	4.24×10^{5}	$2.4 \times 10^{4} - 1.1 \times 10^{5}$

*Roughness values for reference, smooth case. Section 5.4.2 discusses the effect of additional roughness.

The similarity of dimensionless parameters is quite good, especially considering the restrictions on space and pipe size availability that were met. The only dimensionless parameter that is significantly lower is the *Ar*, and Section 5.3.2 investigates this relationship to prove that the analytical results can be extrapolated accurately into that region.

5.3.2. Effect of the Archimedes Number (*Ar*) on Reynolds Number (*Re*)

Initial experiments varied *Ar* by changing the mass of the canister, while using 22.5° C water. Figure 5-7 presents a comparison of the modeled vs. experimental results for the first experiments completed using a 14.79 kg reference sized experimental canister on May 26, 2010.

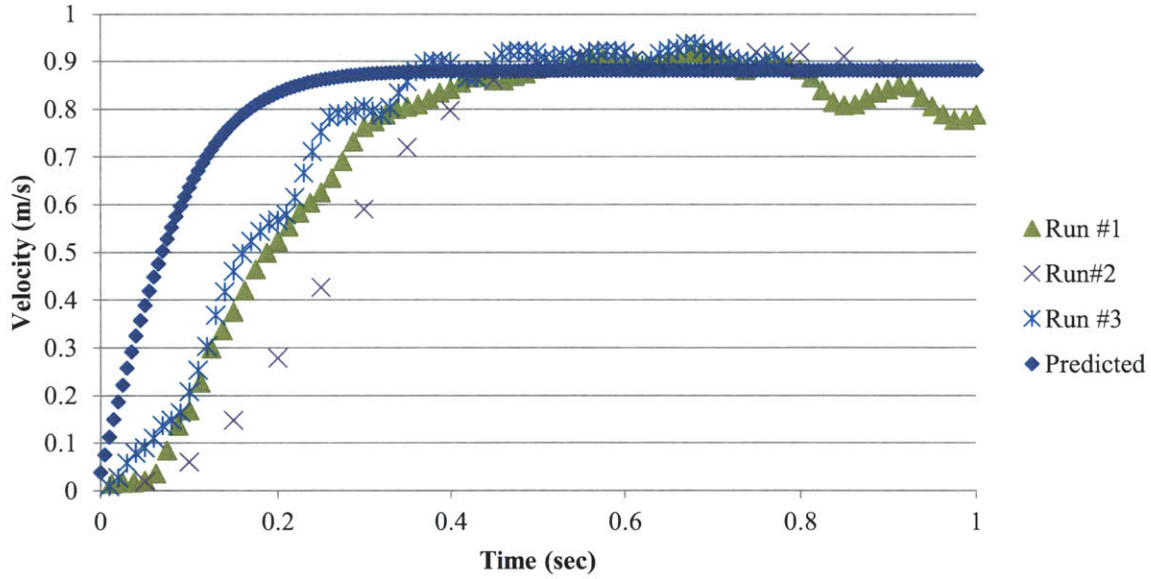

Figure 5-7. Experimental results from the first set of experiments on May 14, 2010 using a 14.79 kg canister. Note that run #1 was recorded at 80 hz, run #2 was recorded at 20 hz, and run #3 was recorded at 100 hz.

The runs converge very closely to a predicted terminal velocity of 0.889 m/s, although there is some oscillation about that value. The sensor was tested at multiple sampling rates (20, 80, 100 hz) to ensure that the sample rate did not have an effect on the accuracy of the sensor reading. Note that even though there were only 3 separate drop tests, each run constituted multiple measurements of the terminal velocity. For example with run #3, within the region of terminal

velocity (between 0.36 seconds and 0.8 seconds), 43 samples are taken. The averaged terminal velocity over all 93 samples taken in the regions of terminal velocity is 0.89 m/s.

A total of 33 room temperature (22.5° C) drop tests were conducted with canister masses of 8.19 kg, 10.39, 12.59 and 14.79 kg (see Appendix B.2 for graphs). Furthermore, an additional 29 drop tests occurring in water temperatures between 48° and 92° C, using a 14.40 kg canister, yielded results over a much broader range of *Ar*. The results of all the tests are summarized in Figure 5-8.

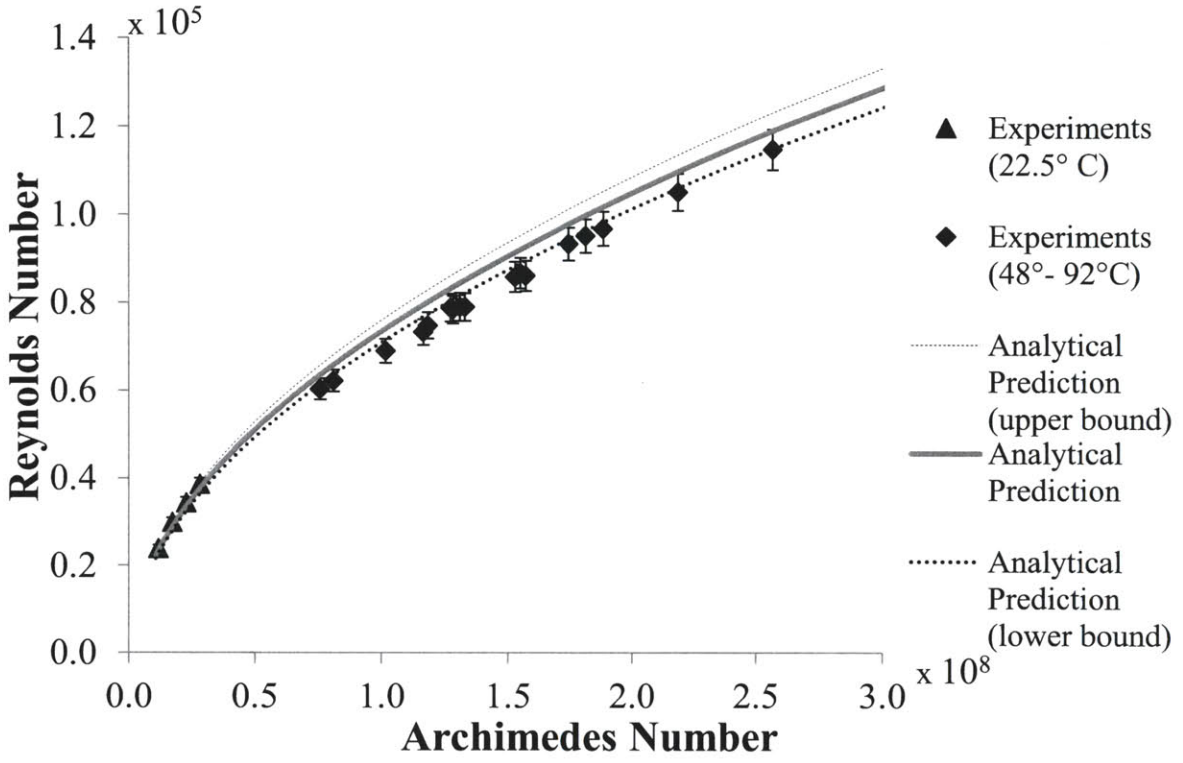

Figure 5-8. Summary of all 62 borehole drop experiments completed to investigate the relationship between the Reynolds number and Archimedes number for the fluid flow.

The error analysis and bounds are described in Appendix B.5. Overall, the model captures the viscosity dependence of the canister velocity accurately. An identified, but difficult to measure and quantify source of error is the differential thermal expansion of the canister, which can change hydraulic diameter -a crucial parameter in the terminal velocity expression. In fact, when the canister was taken out after extended immersion in the fluid which had reached 48° C, the diameter had increased by 0.5 mm. However, the inner diameter of the lining within the zone

exposed to hot water could not be measured to obtain an accurate estimate of the total change in hydraulic diameter.

5.3.3. Analytical Model Verification

Regression is a common method to analyze and draw out relationships in data. For the series of runs described in Section 5.3.2, the canister dimensions and form losses stayed constant and Eq. (4-14) can be simplified in form to Eq. (5-1).

$$Re = C\sqrt{Ar} = C(Ar)^{0.5} \tag{5-1}$$

where C is defined by Eq.(5-2).

$$C = \sqrt{\frac{\left(2\frac{l}{D_h}\right)}{f\left(\frac{l}{D_h} + \frac{l}{D_c}\right) + K_{form}}} \tag{5-2}$$

The friction factor varies slightly with the temperature of the fluid and the speed of the canister, between 1.7×10^{-2} and 2.2×10^{-2}. Substituting the constant experimental canister values of l, D_h, K_{form}, and relatively constant value of f into Eq.(5-2) reveals that C varies between 7.12 and 7.79. Figure 5-9 plots the same experimental data as Figure 5-8, in terms of $\ln(Ar)$ vs. $\ln(Re)$.

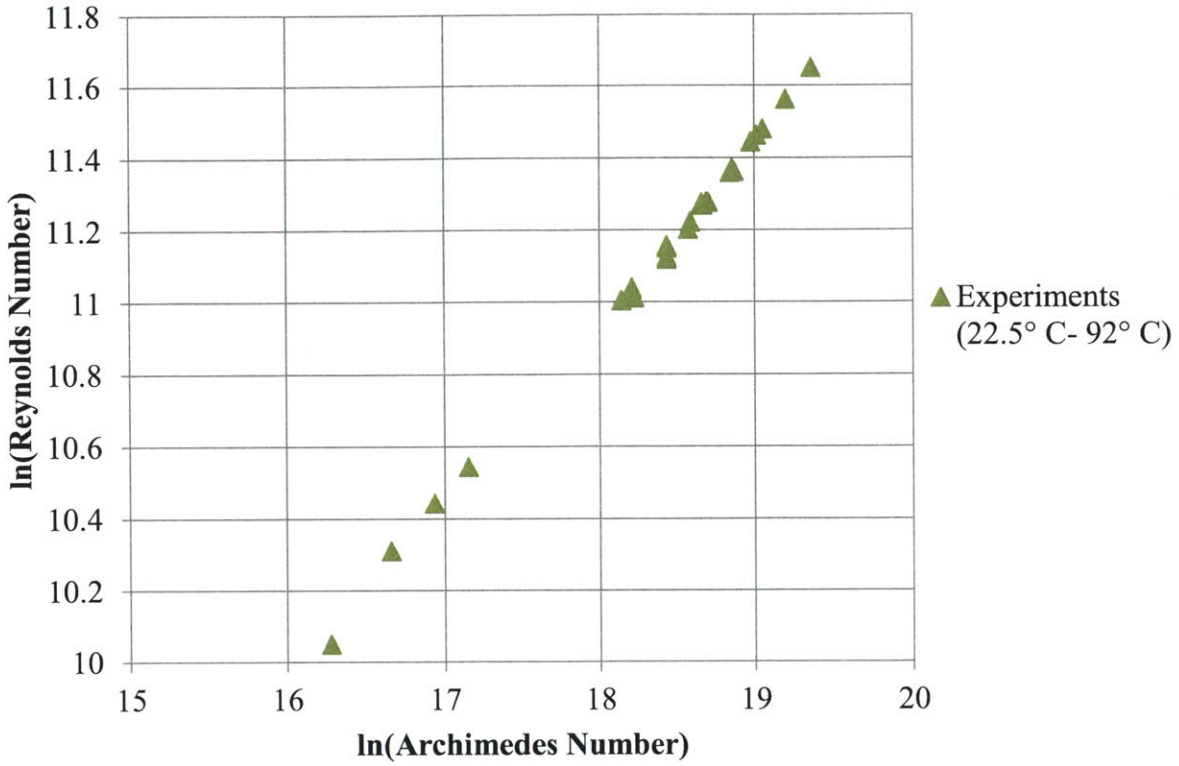

Figure 5-9. Plot of the experimental drop data demonstrating the underlying relationship of ln(*Ar)* vs. ln(*Re).* Data obtained through a total of 62 drop tests with variation of water temperature between 22.5° and 92° C, and canister density between 2363 and 4264 kg/m^3.

With an $R^2 = 0.997$, the graph is fitted by the line described by Eq.(5-3),

$$\ln(Re) = 0.493 \ln(Ar) + 2.0615$$
$$\ln(Re) = \ln(Ar^{0.493}) + 2.0615 \tag{5-3}$$

raising both sides by the power of an exponential,

$$e^{\ln(Re)} = e^{\ln(Ar^{0.493})+2.0615}$$
$$Re = e^{2.0615} Ar^{0.493} \tag{5-4}$$

which produces Eq. (5-5)

$$Re = 7.85\, Ar^{0.493} \tag{5-5}$$

These regression parameters are very close to the analytically derived curve parameters, in terms of the constant (7.85 vs. 7.45) and exponent of the Archimedes number (0.493 vs. 0.5). This further validates the analytical, dimensionless expression for terminal velocity, Eq. (4-14).

5.4. Additional Investigations

5.4.1. Effect of Drag Inducing Features

Additional experiments were completed to determine the effect of a drag inducing feature (in this case a rubber disc axially protruding 6.66 cm in front of the canister). The drag inducing feature is shown in Figure 5-10.

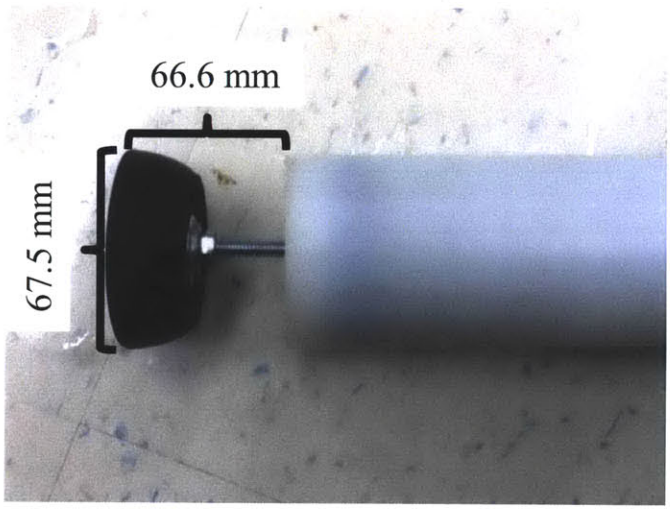

Figure 5-10. Drag inducing feature (plug) of the simulated borehole canister, showing the diameter and the axial distance from the canister.

The plug was adjusted to have a diameter as similar as possible to the canister. With the same diameter as the canister, the plug is modeled with the exact same continuity, velocity ratio, and momentum relations as the canister. In short, this allows it to be modeled as an additional form loss to the fluid flow- (see the term "K_{form}" in Eq. (4-14)).

Secondly, the plug extended beyond the canister by approximately the diameter of the canister. It was postulated that this would be an appropriate, yet minimal length that would still have an effect. An analogy to consider is the situation of a protruding pipe into a pool, which has a separate entry effect (form loss), if the length that it protrudes is greater than half the

diameter of the pipe, because of separation of the boundary layer [45]. In practical terms, the plug protrusion length should be minimized because even 6.66 cm of plug length becomes 0.33 meters when scaled up. When stacked 400 times for each canister, the plugs begin to detract from valuable vertical space within the borehole. This approximately square symmetry also allows for the designed form loss to easily be scaled up.

If the disc is modeled as a sudden contraction and expansion it provides an additional K_{form} of 0.5 + 1=1.5 [44]. However, the plug provides a gradual expansion, so the second term would tend to be less than one. Overall this leads to a predicted total K_{form} in the range of 2 to 3. In six experiments run at water temperatures between 72°C and 77.5°C, the modified canister's terminal velocity was more than 10% lower than the unmodified canister velocity in previous experiments. The results are these tests shown in Figure 5-11, with the data from Figure 5-9 also shown for reference.

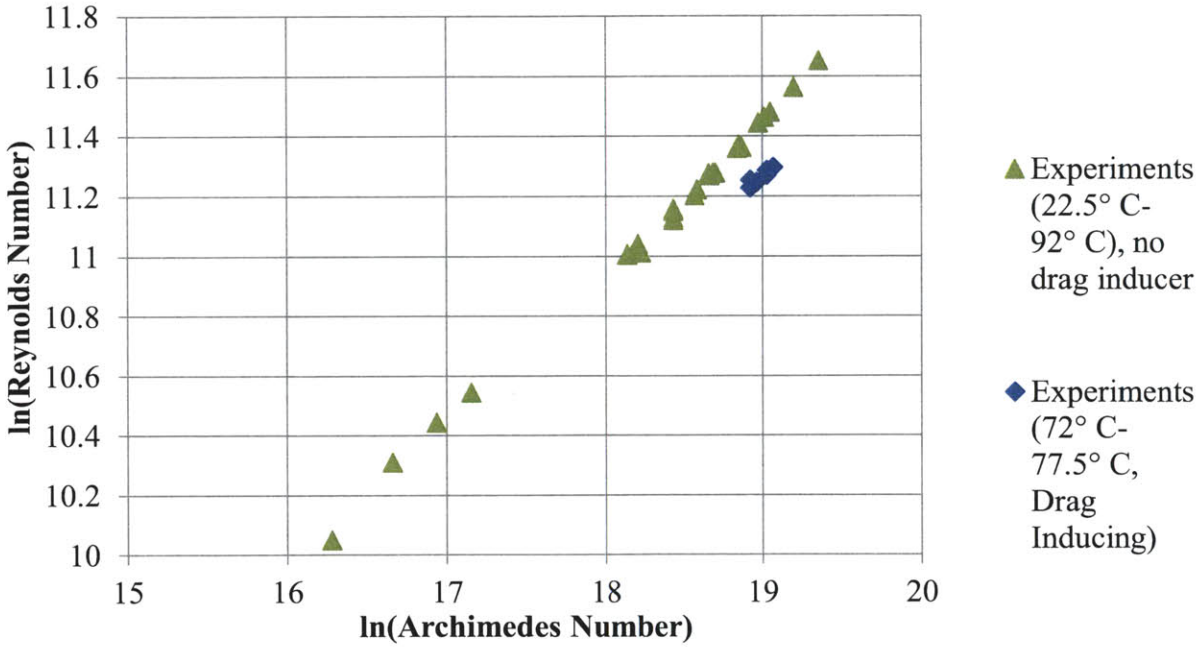

Figure 5-11. Plot of the experimental drop data demonstrating the underlying relationship of ln(*Ar*)vs ln (*Re*), with the effect of an added form loss. Drag inducing data obtained through 6 drop tests with variation of water temperature between 72.5.5° and 77° C, with a canister density 4335 kg/m^3.

Notice a downward shift in the line resulting from the form loss; however, the slope appears to be similar. Repeating a similar regression process as in Section 5.3.2, with an $R^2 = 0.78$, the graph is fitted by the line described by Eq.(5-6),

$$\ln(Re) = 0.4924 \ln(Ar) + 1.91 \quad (5\text{-}6)$$

to produce Eq. (5-7),

$$Re = 6.753\, Ar^{0.4924} \quad (5\text{-}7)$$

Once again, the exponent (which theoretically should be 0.5) is quite accurate. Using a friction factor of 1.83 x 10^{-2} and substituting in the canister's properties into Eq. (5-2), K_{form} is calculated to be 2.45 (expected to be range of 2 to 3). Therefore, it was concluded that the analytical model accurately accounts for the effect of additional drag-inducing features, and that a drag-inducing feature can be effective in reducing the velocity of the canister.

5.4.2. Effect of Surface Roughness

The friction factor has a very strong dependence on the surface roughness. For example, on a standard Moody diagram, if the relative roughness is great enough (greater than 0.05), the friction factor is almost solely determined by the relative roughness and is only minimally affected by the Reynolds number. From this it was postulated that increasing the roughness of the canister could greatly reduce the terminal velocity. The simplest method to increase the roughness of the test canister involves using standardized sandpaper. Understanding the surface roughness of such paper is important in the designing the experiment. The average particle sizes of various standard sandpapers have been reported [43]. Investigations of the relationships between the many measures of surface roughness indicate that the roughness value ε (also referred to as k_s) can be approximated by the average particle size as in Eq. (5-8) [46],

$$k_s = 1.23 d_{50} \quad (5\text{-}8)$$

Figure 5-12. presents the particle size and roughness values across the entire range of commercially available standard U.S. ANSI 74 sandpaper grits

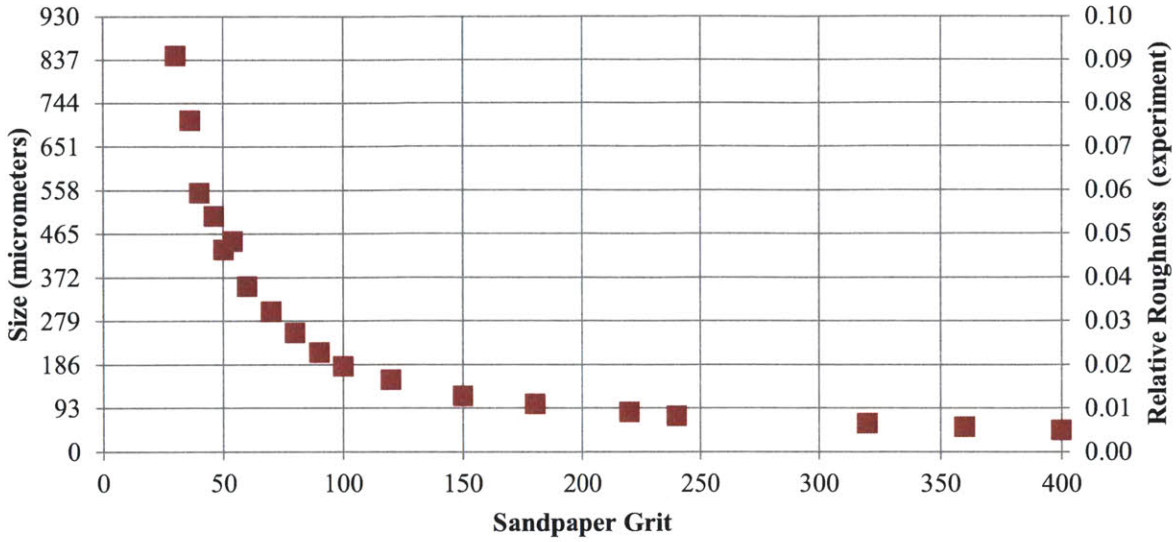

Figure 5-12. Average particle size and relative roughness (k_s/D_h) as a function of sandpaper grit (ANSI 74 standards), for the experimental scale canister. Particle sizes compiled from [47],[48] and k_s calculated using Eq. (5-8).

According to Figure 5-12 the "fully rough" relative roughness of 0.05 can be achieved at the experimental scale using the roughest commercial sandpaper (50 grit). The minimum grit of adhesive sandpaper that was available for purchase was 60 and 80 grit. According to Figure 5-12, 60 and 80 grit sandpaper have particle sizes of 271 and 195 microns respectively, corresponding to a predicted relative roughness of 0.0379 and 0.022 respectively. Confocal microscope analysis (see Appendix B.4) indicated that the surface roughness for the 60 and 80 grit adhesive sandpapers was 412 and 311 microns, respectively. This corresponds to a relative roughness of 0.049 and 0.038. This is slightly larger than those reported above [43].

The first set of tests involved 60 grit sandpaper attached to the surface of the test canister, with drag inducing plugs, to provide a dramatic contrast with previous experiments by maximizing the effects of roughness and form loss combined. A photo of the canister in this configuration is shown in Figure 5-13.

Figure 5-13. Photo of the canister with attached 60 grit sandpaper and drag inducing plug.

The results of the drop tests involving this canister setup are summarized in Figure 5-14.

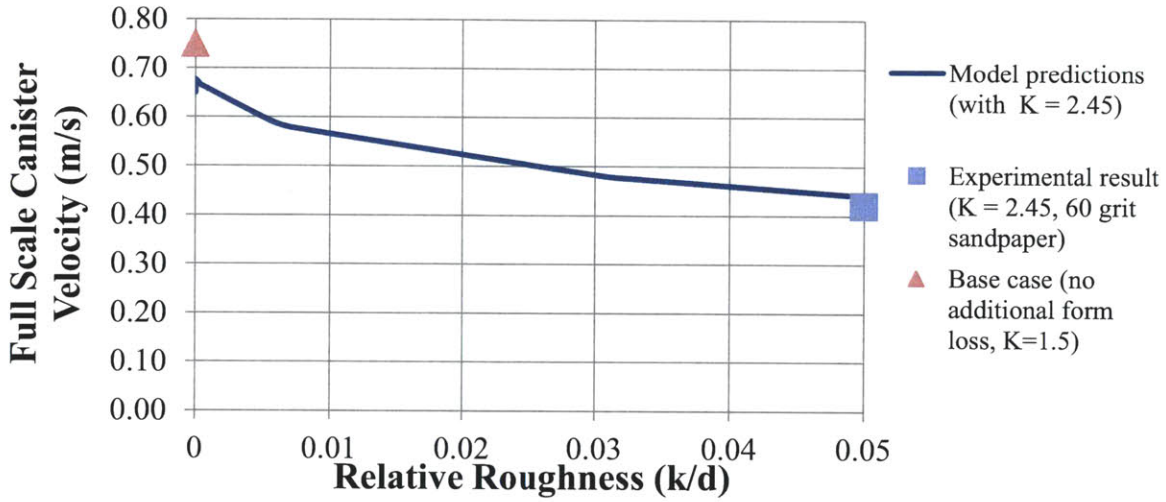

Figure 5-14. Experimental result, averaged from 6 drop tests of a 15.025 kg canister with 60 grit sandpaper and drag inducing plug attached. Note that the sandpaper increased the diameter of the canister slightly to 6.80 cm.

Figure 5-14 conveys that for the experiment, almost a 50% reduction in velocity (from the base case) can result from the use of a hydraulically rough surface and additional form loss. The second set of tests involved 80 grit sandpaper attached to the test canister, without the drag inducing plug. The results are shown in Figure 5-15.

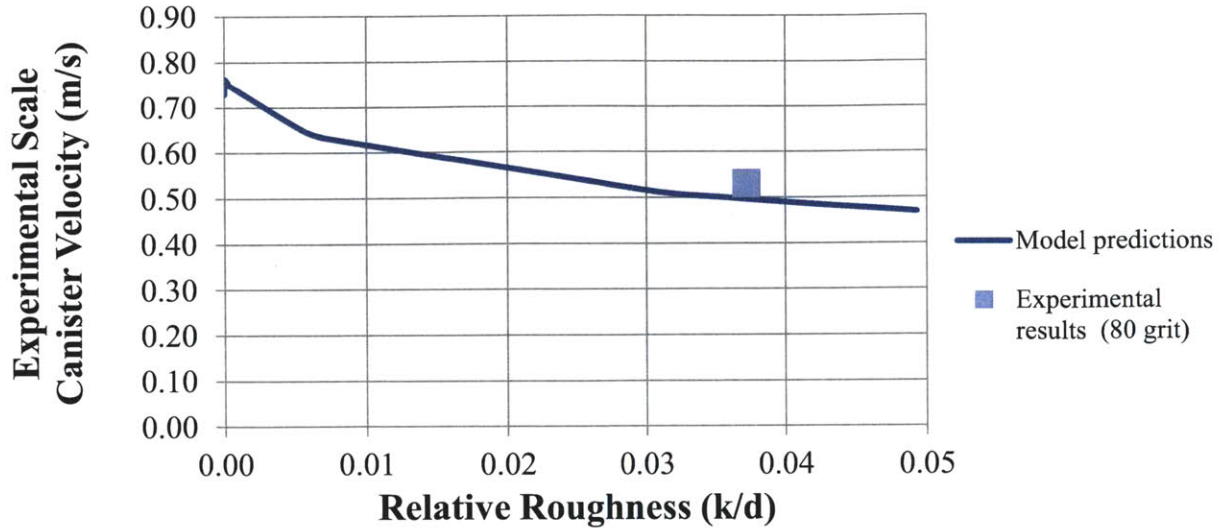

Figure 5-15. Experimental result, averaged from 7 drop tests of a 14.963 kg canister with 60 grit sandpaper attached. Note that the sandpaper increased the diameter of the canister slightly to 6.80 cm.

The results show that the model's use of standard pipe flow equations can accurately take into account varying levels of increased surface roughness and form loss.

5.5. Chapter Summary

An appropriately sized and low cost experimental setup was designed to validate the analytical model and investigate form and friction loss effects. The design allowed for easy modification of the canister, surface, and fluid properties, and tests could be repeated in quick succession. In total, 81 successful drop tests provided experimental data over a wide range of conditions. The data confirms the model's ability to take into account changes over a wide range of fluid properties. Increased form and frictional losses were confirmed as feasible methods of reducing the canister's velocity, and the analytical model was flexible enough to take these safety options into account.

6. Feasibility of Proposed Emplacement Method

6.1. Chapter Introduction

The proposed emplacement method can be analyzed critically in accordance with the same criteria as the other suggested emplacement methods in Chapter 2. As with many nuclear waste projects, the most important issues are structural (which determines the integrity of the waste barrier), time, cost, and equipment requirements. The analytical model and experiments made assumptions on the state of the canister during emplacement (no heat generation taken into account), so other conditions such as the temperature profile of the canister during transport and emplacement are also important to prove that the model is still valid.

6.2. Thermal Issues

Previous analyses at MIT have shown the down-hole temperature profiles of the canister to be safe, after emplacement and closure of the repository [12][49]. Hoag's analysis is dominated by heat transfer effects across the gap between the canister and the borehole lining. However, thermal analysis during canister transport to the hole and during the emplacement may be important for the drop-in method. For example, if the canister surface temperature exceeds 100° C, when the canister is initially dropped into a flooded borehole, the surrounding water would boil. If film boiling occurred (highly unlikely given the low heat flux) this would create a gas layer around the canister, resulting in an increase in terminal velocity above expected values. Without film boiling, two phase flow occurs and the pressure drop actually increases, reducing the terminal velocity of the canister. Another issue is that excessive canister temperatures and rapid quenching would result in a thermal shock to the structural integrity of the canister. The decay heat for 60 GW-day/MTU burnup fuel can be described by an inverse power law relationship as in Eq. (6-1) [12] :

$$q' = \frac{2200}{t^{0.75}} \tag{6-1}$$

where t is years from discharge from the reactor and q' is the linear heat generation in W/m. The reference, square, 17x17 pin PWR assembly contains 0.5 MTU, is 4.2 m tall and has a

diagonal width 0.303m [12]. Hoag's thermal analysis yielded a homogenous conductivity and effective diameter of 0.2417 m for the fuel assembly (with interstitial sand), greatly simplifying this study's thermal analysis. Outside of the canister, this analysis differs because it introduces the insulating effects and heat conduction of a radiation shield – assumed to be a 0.5 m thick concrete cask. For reference, a concrete dry cask storage system which contains 21 PWR assemblies has cask body walls with a thickness of 0.38 meters [50], so 0.5 meter is a conservatively high approximation for the thickness required for radiation attenuation. A diagram of the homogenized assembly, steel casing, and concrete cask configuration is shown in Figure 6-1.

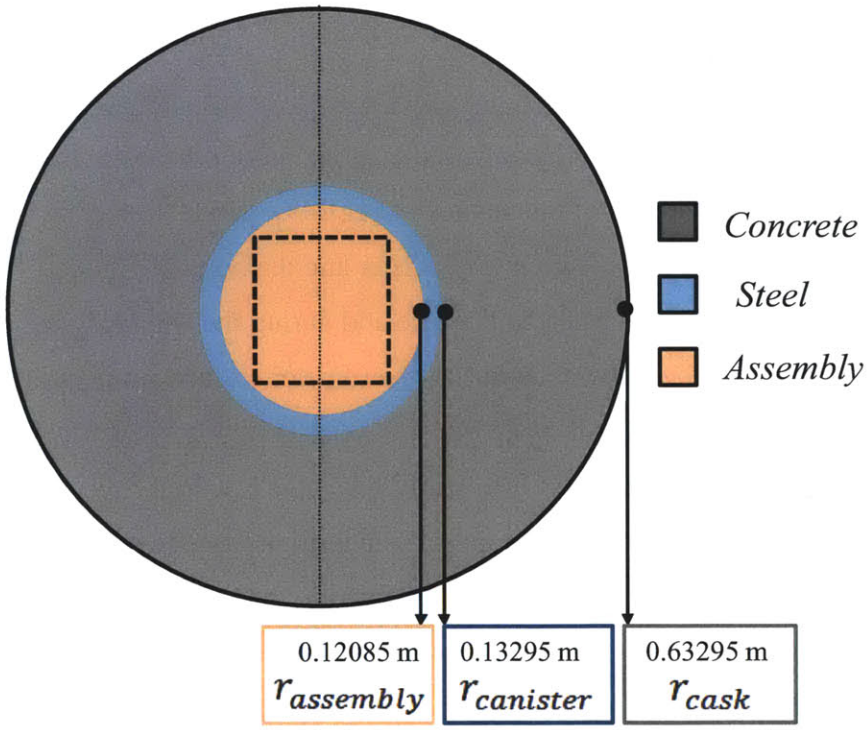

Figure 6-1. Schematic of the geometry and materials for the proposed emplacement radiation shield (cask), containing the canister and fuel assembly. Not to scale.

Where $r_{assembly}$ is the homogenized fuel assembly effective radius, $r_{canister}$ is the steel canister outer radius, and r_{cask} is the cask outer radius. Using the assumed material values (see Table C-1) and solving the heat transfer equations (see Appendix C.2) the surface temperatures for each region are obtained. Figure 6-2 shows the canister decay heat, surface temperature, and centerline temperature versus the number of years the fuel assembly has been removed from the reactor.

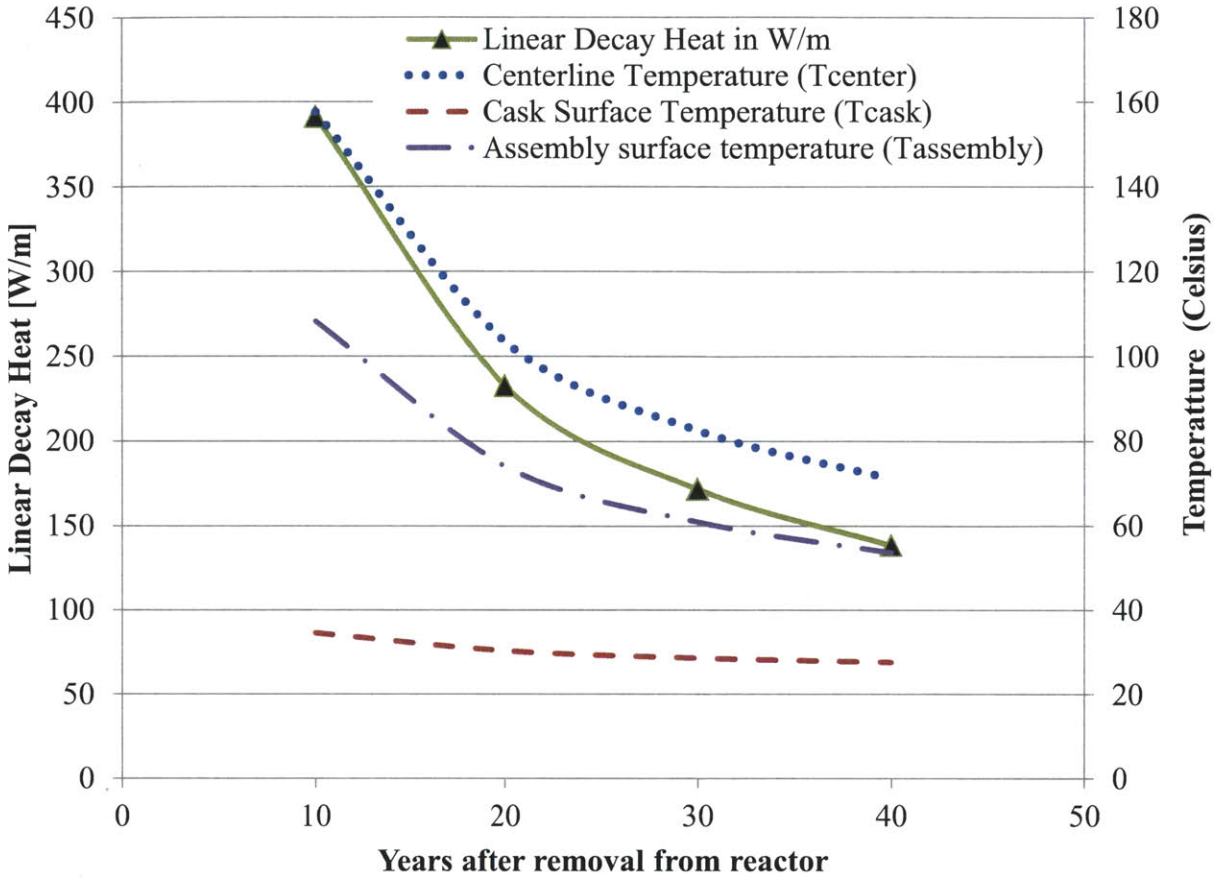

Figure 6-2. The linear decay heat, maximum fuel centerline temperature, cask surface temperature and (homogenized) assembly surface temperature as a function of time in years.

The internal, continuous temperature distributions for various linear heat generation rates (based on derivations completed in Appendix C.3) are shown in Figure 6-3. The greatest temperature difference occurs within a 0.5 m concrete cask, which acts as an insulator. The 12 mm (0.5 in) thick steel lining causes a negligible temperature difference (<0.2°C).

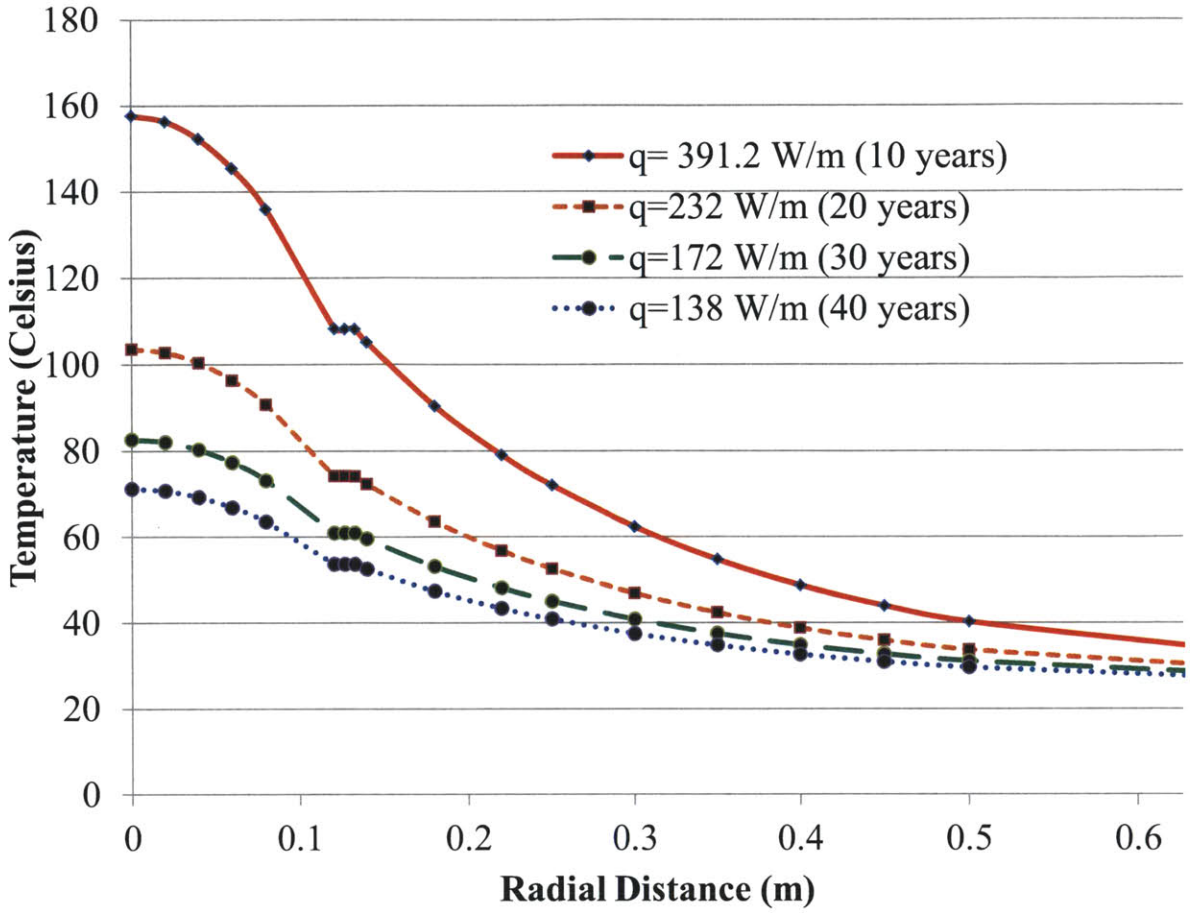

Figure 6-3. Temperature profiles within the assembly, canister and cask for a range of fuel ages between 10 and 40 years.

The thermal analysis indicates that under expected conditions, the canister will experience safe assembly surface and centerline temperatures, even with a conservatively thick 0.5 m concrete shielding. In the case of very young fuel (10 years), the assembly surface temperature will be 108 °C. This may initially cause boiling at the surface when the canister emplaced into the water filled borehole, but this surface temperature will drop quickly as it transitions to new heat transfer boundary conditions with larger heat transfer coefficients (forced convection with water). Secondly, the hydrostatic pressure of the water in the borehole increases the boiling point of the fluid with depth. By the time the canister reaches the point of impact within the 2-4 km tall column of water, even if it is still at 108° C, the water surrounding it will no longer be at its boiling point. Lastly, it is expected that by the time a waste repository could be licensed, the

vast majority of fuel will be greater than 10 years old. With 30 year old fuel (a more reasonable estimate for the average age of the fuel), the assembly and canister surface temperature is 61°C. Furthermore, if needed, the canister surface could be cooled in a controlled and gradual fashion by forced convection using a water spray prior to drop in.

The previously described analytical model assumes that the fluid within the borehole is at rest. Boreholes in deep granite are not expected to have pressurized aquifers or other flow features that would produce significant upward flow gradients under ambient conditions [13]. Even if flowing conditions could be induced (for example during the initial thermal equilibration and expansion of the flood water), the upwardly flowing currents would reduce the velocity of the canister. It is difficult to conceive of a scenario that would cause unexpected downward currents that may accelerate the canister.

6.3. Structural Issues

The strength of the DBWD canister at impact is one issue, as breach of the canister during emplacement may cause a leak of radioactive materials to the surface facility and workers. At the bottom of the borehole, the canister is predicted to be moving at a maximum of speed 2.6 m/s, which could easily be mitigated with an engineered bumper or other energy absorber. A highly applicable experience is the Department of Energy (DOE) spent nuclear fuel (SNF) design process for a waste canister. A substantial amount of analytical and experimental work was commissioned by the DOE to develop a versatile, standardized, robust canister for the interim storage, transportation and final disposal of spent nuclear fuel (SNF)[51]-[53]. The studies combined full scale experimental drop tests and computational (FEA) methods to analyze the potential damage to the canister. The primary design intent was to have an easy to handle canister that could accept numerous types of SNF with good corrosion resistance. Although additional safety functions (such as radiological shielding and long term storage) are intended to be provided through other components within the storage facilities, the DOE SNF canister is required independently to provide a containment that maintains integrity even in the event of an accidental drop. The safety and impact analysis from the DOE SNF canister design are summarized below, and can be adopted in the finalization of a deep borehole canister design.

Both Hoag's and the DOE SNF designs use standard casings or piping components for the canister, and are similar in overall size and mass. However, the DOE design differs by several factors to improve corrosion resistance, impact absorption and ease of handling:

- 316L stainless steel body constructed of standard SA-312 piping.
- Lower heads comprised of ASME flanged and dished, SA-2401 316 L stainless steel.
-Protruding skirts to provide energy absorption and plastic deformation.
-Lifting rings located within the outer end of each skirt
-Interior impact plates on the top and bottom of the canister

A diagram of the additional safety factors is shown in Figure 6-4.

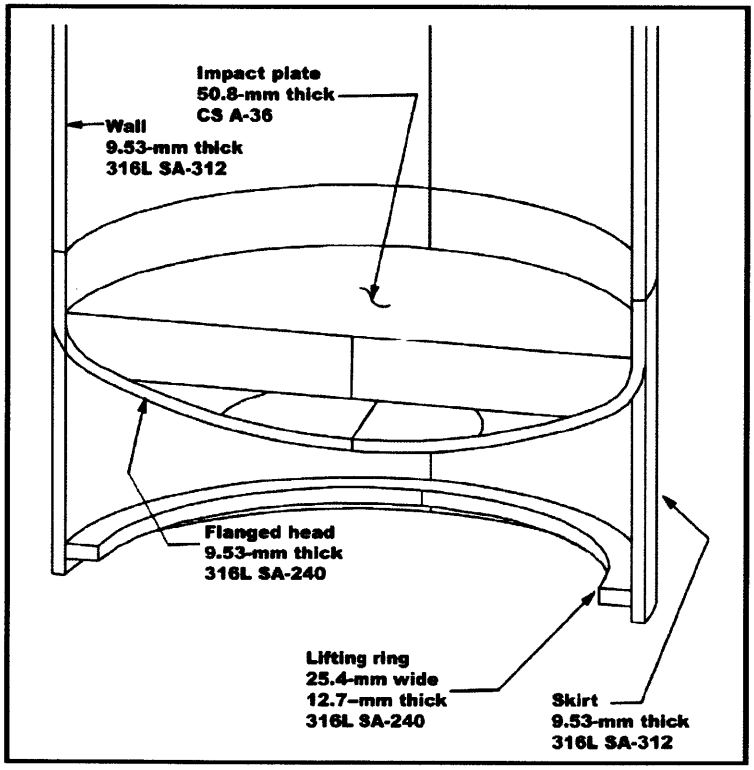

Figure 6-4. Additional designed safety features of a DOE SNF canister [51].

A comparison of the typical canister geometries and properties is presented in Table 6-1.

Table 6-1. Comparison of canister geometry and material properties between a DBWD canister and a DOE SNF canister [52].

Canister Design	Canister Material	Outer Diameter -D_c- (mm)	Inner diameter (mm)	Wall thickness –t- (mm)	Length (m)	Typical Mass (kg)	Overall Density (kg/m^3)
Hoag	Drill Casings-J55-P110 Steel	339.7	315.32	12.19	5	2000	4400
DOE SNF	SA-312 Pipe-316L Stainless	457	437.9	9.53 (nominal)	4.5	3626	3626

A total of nine, full scale DOE SNF canisters were dropped from a height of 9m (30 ft) in various orientations onto an unyielding surface to test the containment integrity of the design. Pressure and leak testing confirmed that the canister's seal was maintained in all cases. The orientation that resulted in the maximum peak equivalent plastic strain (on the skirts and lifting rings) was when the canister was dropped at an offset angle of 6 degrees from vertical. When the canister dropped in a horizontally flat orientation, the skirt did not provide protection. However, in this case the impact energy is distributed along entire length of the canister, and only minimal deformation took place. An image of a deformed skirt is shown in Figure 6-5.

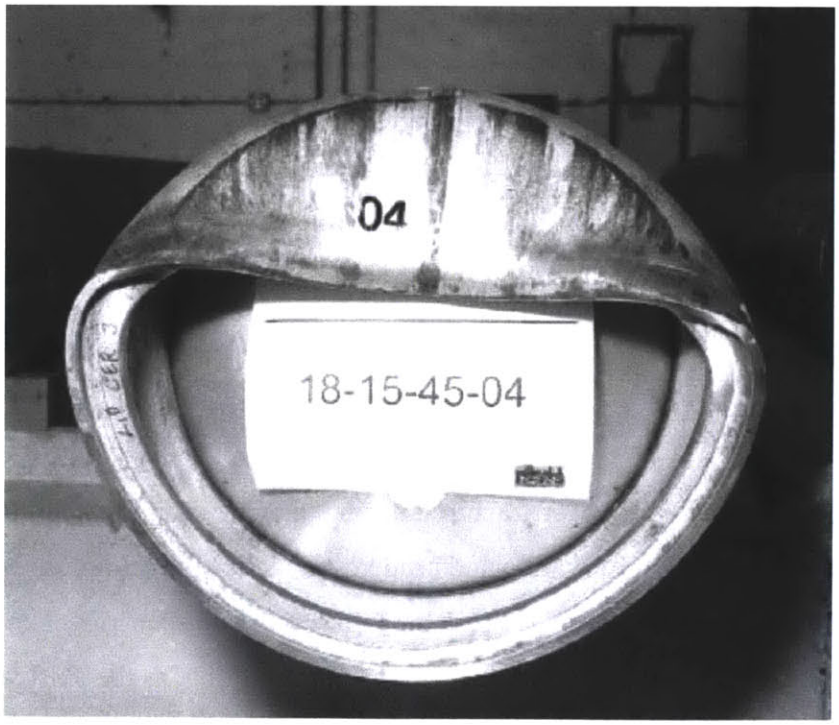

Figure 6-5. Deformed end of a DOE SNF canister after a drop test from 9 meters at an angle of 45 degrees [52].

The deforming skirt could be incorporated into Hoag's canister design easily, and would provide an additional level of safety to the canister when it impacts at the bottom of the borehole. The protruding cup shape also adds a form loss to fluid flow, thereby reducing velocity. Using scaling arguments and the data from the DOE SNF drop tests, it can be argued that Hoag's canister will be safe when impacting at the expected velocity of (2.6 m/s). It is postulated that the primary variables affecting the plastic strain in this case are the wall thickness, skirt diameter and length, impact energy and material yield strength. These parameters are chosen because they are similar parameters investigated using the Charpy impact test, a high strain rate test which determines the amount of energy absorbed by a material during impact and fracture. With the Charpy impact test, the geometry of the specimens are standardized and kept constant such that the yield strength and fracture toughness of the material can directly be correlated to the energy of fracture. In this case, the impact energy is the kinetic energy of the canister at impact, and is a function of the mass of the canister and the impact velocity. The length of the canister would seem to be irrelevant because the plastic deformation is locally confined to the skirt. Thus the length of the skirt is an important parameter. A comparison of the impact parameters of Hoag's canister and the DOE SNF canister are presented in Table 6-2.

Table 6-2. Comparison of impact parameters between a DBWD canister and a DOE SNF canister [52].

Canister Design	t/D_c	**Drop Height (m)**	**Impact velocity (m/s)**	**Mass (kg)**	**Impact energy (joules)**	**Skirt Impact Area (m^2)**	**Minimum Work of Fracture (joules/m^2)**
DOE SNF	2.084×10^{-2}	9	13.28	3626	2.4×10^{5}	1.36×10^{-2}	1.77×10^{7}
Hoag	3.629×10^{-2}	n/a	2.6	2000	6.75×10^{3}	1.27×10^{-2}	5.31×10^{5}

The DOE SNF canister and skirt never fractured during the nine drop tests completed, and the results provide an extremely conservative and crude estimate for the minimum work of fracture or impact strength that the skirt provides in such a high strain rate scenario. The results indicate that Hoag's canister would provide more than sufficient protection, as the skirt would experience a lower work of fracture (energy/area) by two orders of magnitude, while having a larger t/D_c (the typical parameter of interest in structural, shell geometry situations). One difference is that

the DBWD canisters will be repeatedly stressed (from successive impacts of canisters above). However, the energy of these repeated impacts is spread over an increasing number of canisters and skirts. Therefore the successive impacts result in much lower stresses on the first canister compared to the stresses it experiences during its initial collision on the unyielding borehole floor. Furthermore, the number of fatigue cycles (a maximum of 400 from each canister impact) is not sufficient to significantly reduce the strength of the steel, a process which typically requires tens of thousands of fatigue cycles.

6.4. Drag Inducing Features at Full Scale

The comprehensive analytical and experimental work described thus far gives a high level of confidence in the predictions of the full scale canister's velocity. Although the predicted velocity of 2.4 m/s is not particularly challenging, Section 5.4.2 discussed relatively simple methods to reduce this further, through increased canister surface roughness. Figure 6-6 summarizes the predictions of the analytical model for the full scale canister with varying surfaces and levels of roughness.

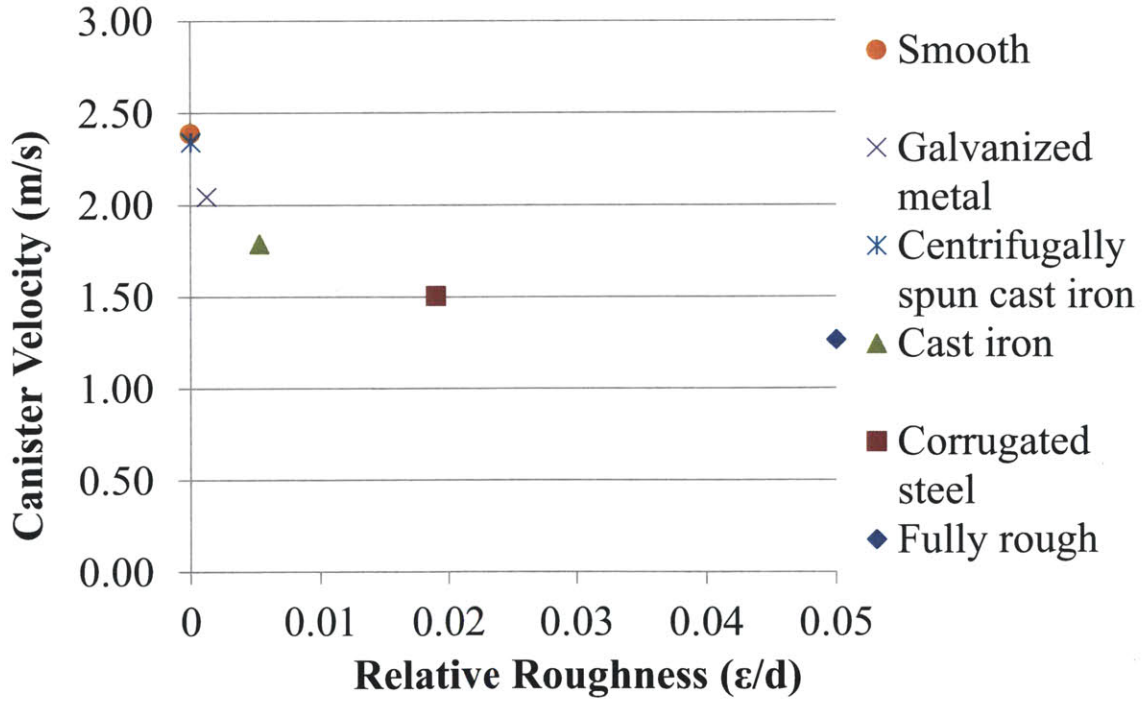

Figure 6-6. Predicted full scale terminal velocity vs. relative roughness for various commonly used metals [43].

The results indicate that if the canister surface was fully rough (ε/d >0.05), the velocity could be reduced by almost 50% to 1.26 m/s. However, none of the metals that have been suggested for the canister are normally that rough. Increasing the roughness of the metal canister's surface (through machining or sand blasting) leads to an increased surface area exposed to corrosion. Therefore another method of modifying the canister surface roughness, by using glue or corrosion resistant epoxy to attach sand particles directly to the surface, may be preferable. In fact, specialized epoxy coatings are frequently applied to pressure vessels and pipes to increase chemical resistance. This would result in a very similar approach to Nikuradse's sand grain tests, proven during his famous investigation of the effect of pipe surface roughness on pressure drops [54]. Since D_h for the full scale case is 4.73 cm, using Eq. (5-8), the average particle size would be 1.92 mm.

Another experimentally proven method to reduce the canister's velocity is the use of drag-inducing features. When combined with increased surface roughness, the canister showed a dramatic reduction in velocity. Figure 6-7 presents a summary of predictions for the full scale canister's velocity over a range of increased surface roughness's and form loss.

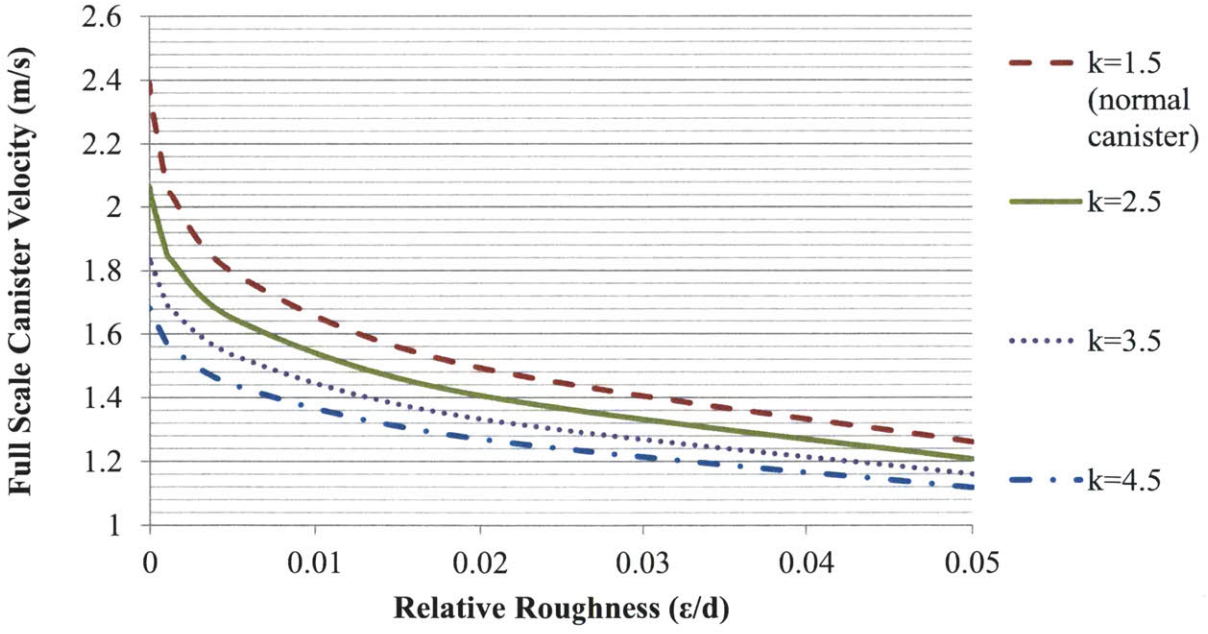

Figure 6-7. Predicted full scale terminal velocity vs. relative roughness and form loss coefficient (k).

The primary conclusion from Figure 6-7 is that if a fully rough canister surface has been attained, the additional form losses only make a small difference. A form loss coefficient of 3.5 may be feasible with drag-inducing plugs on the top and bottom of the canister. To achieve a greater form loss coefficient, it is likely that a parachute or similar apparatus would be required. The surface roughness approach is preferred, because it has fewer failure modes than the form loss method (the plugs may break off causing the canister to jam or the parachute may not deploy). In summary, this analysis shows that even if 2.6 m/s is considered threatening to the integrity of the canister, the methods of adding form and friction losses are feasible to lower the speed even further.

6.5. Backfill Process

Although the reference borehole repository design assumes an air gap between the canister and the lining, other deep borehole designs such as SKB's include buffers such as bentonite clay to retard the movement of radionuclides. Alternatively for the sake of retrievability, graphite could be inserted into the annulus to lubricate the movement of the canisters during a retrieval effort. When considering an emplacement method, it is important to keep these options considered and open.

If bentonite is desired, one option is to use bentonite as the mud during initial drilling of the hole. In this case, since the viscosity of a bentonite mud is higher than that of pure water, the terminal velocity of the canister would be greatly reduced. If the desired composition of bentonite is too viscous or highly dense for a drop-in method to work, the bentonite slurry could subsequently be pumped into the annulus, using the same methods that are used to insert cement and grout into the annulus between the lining and the rock wall. Figure 6-8 illustrates the piping configuration used during this process.

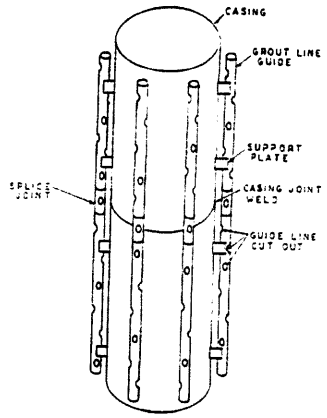

Figure 6-8. Depiction of pipes used to grout casings into a borehole [23].

The bentonite slurry could be inserted at the bottom of the borehole, and would displace the water as it is pumped in. Graphite powder could be inserted in a similar method. To ensure a uniform annulus over the entire height of stacked canisters, longitudinal centralizing fins can be attached along the sides the canister. An SKB engineering study suggests that centralizers be approximately 1 m in length, 15 mm in width, and the outer diameter 15 mm less than the internal diameter of the casing[29]. The feasibility of this method also depends on the desired composition of bentonite.

6.6. Economics

The primary economic benefit of the proposed drop-in method is that it does not require the original rig (with billing rates of $4850/hr). The time and equipment for the lowering and retrieval stages are essentially eliminated from the emplacement process, leaving only the loading period. The analysis completed in Section 2.3 assumed that the loading period required 10 minutes per canister, with radiation worker billing rate of $10,500/hr. Assuming that this time requirement and billing rate are also appropriate for the loading stage of the drop-in method produces an upper bound estimate on cost, because this method does not require the massive drilling rig. Therefore, for an entire borehole with 400 canisters, this results in an estimated total emplacement cost of $700,000, resulting in per kg cost of $3.5/kg HM. The costs compared graphically with the drill string method estimates in Figure 2-10.

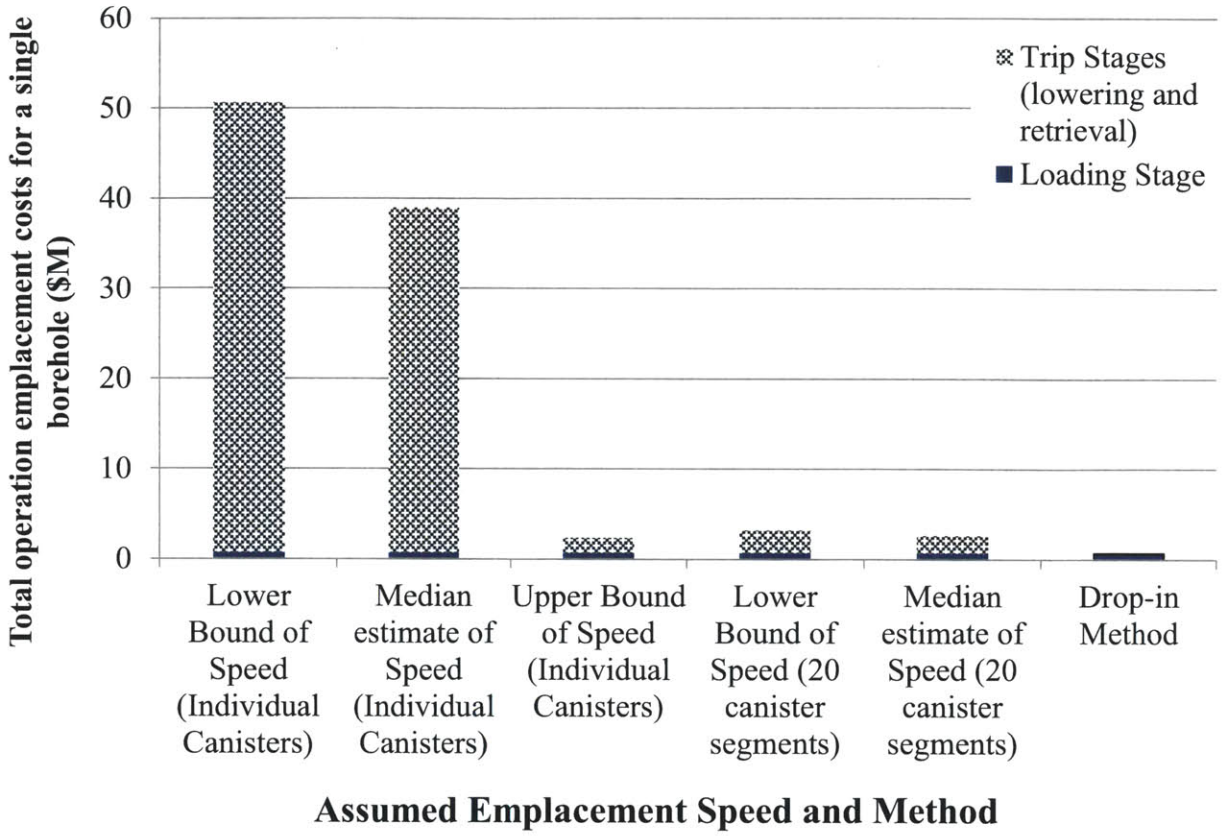

Figure 6-9. Overview of total emplacement costs ($M) calculated using various assumptions on the lowering speed and number of canisters connected, compared to the drop- method.

For the drop-in method, cameras could be periodically lowered to ensure that the canisters are stacking correctly, but this is not expected to be necessary after every single drop. Furthermore, a camera can be presumably lowered much faster and with less equipment than a 5 ton canister, so the inspection process should not be overly time consuming or costly.

In conclusion, the minimum cost for the drill string method is $2.31 million, while a drop-in method is estimated to cost $700,000. Therefore the drop-in method provides an impressive 70% cost reduction over the drill string method, even when using the most optimistic assumptions for the achievable speed drill string method. An added benefit is that with the drop-in method, drilling of the next borehole can proceed while canisters are emplaced in the first borehole, greatly expediting repository construction.

6.7. Retrievability

The option to retrieve waste emplaced in geological repositories is a long-standing question for all nuclear waste management programs. The demand for such a feature is primarily political and social in nature and in many cases has manifested itself in laws and regulations on repository design. A compelling long term safety case for disposal must be made to a very high level of confidence (independent of the option of retrieval); however, retrievability still contributes to confidence in safety [55].

The Nuclear Regulatory Commission's (NRC) definition of retrievability is almost identical to those outlined in 10 CFR 60.111(b) and 10 CFR 63.111(e): "A repository must be designed such that any or all of the emplaced waste could be retrieved on a reasonable schedule starting at any time up to 50 years after the waste emplacement operations are initiated." [56]. Here the key undefined term is "reasonable", because technically any waste emplaced in a stationary repository could be retrieved - the question is how much money can be "reasonably" spent. The NRC has specified that waste retrieval is not meant to facilitate economic reuse of materials, and it is to be exercised only in an unusual event to protect public health and safety [56] . However, the 1982 Nuclear Waste Policy Act (NWPA) has an expanded definition of retrievability, with the stipulation that repositories be designed to permit the recovery of the economically valuable contents of the spent fuel, within an appropriate period, as yet undefined by the DOE. This brings up the distinction between "readily retrievable" and "retrievable", where the former implies open access to disposal rooms and the possibility economic recovery of materials, and the latter allows for backfilling of disposal rooms, possibly resulting in large costs and time during a retrieval operation.

Overall, it has not yet been clarified whether the repository should be designed to facilitate retrieval of the disposed waste, or only that no action during emplacement should obstruct retrieval. With Yucca Mountain, a 50 year retrieval period was not an issue, because of the ease of keeping drifts open in unsaturated tuff for an extended period. The lack of clarity of regulations on retrievability is an important issue to deep boreholes and (other repository designs such as plastic salt domes, which close shafts over time). Some could argue that it is too difficult to retrieve waste from deep boreholes, and that the DBWD does not meet the criteria of retrievability. However, as the recent SKB engineering feasibility study discusses [29], techniques borrowed from the oil industry can be used to "fish" canisters from a borehole (just as

tools, drill bits, or pieces of equipment must be retrievable). The relative cost of such an operation is likely to be higher than for shallow mined repositories, but nonetheless it is possible.

On the other hand, boreholes can be made irretrievable, for example by adding silicon carbide particles to the plug, making drilling through the plug much more difficult. In many scenarios, this may be an advantage for the DBWD concept, because the level of retrievability can be tuned for specific needs. For example it has been suggested to put troublesome, geologically mobile minor actinides or fission products such as Iodine and Technetium or highly heat generating isotopes such as Americium into irretrievable boreholes [49][57]. Alternatively, in countries with unstable regimes that may change their policy on developing nuclear weapons (by reprocessing readily available spent fuel from the country's repository), it might be safer to make the waste inaccessible.

When the NWPA is amended, the decision on retrievability should be clear in scope, definition and intent. A mandate for a geologic repository with the intent of economic reuse of fuel should be looked at critically, as it may unnecessarily preclude more robust options of geologic disposal that attempt to make the waste more remote, (and thus safer from a long term radiological isolation standpoint). If economic reuse is truly a concern, then an interim (100 year) storage facility may be the preferable option to geologic disposal. However, based on current trends for the price of raw uranium vs. reprocessing costs, the reuse and reprocessing option will not be economic for many decades to come [5]-[8]. Secondly, proliferation and security concerns need to be discussed when deciding to make waste readily retrievable for such long periods. Consider that after 70 years, a spent fuel assembly loses its intrinsic safeguard to theft, a deadly dose rate of radiation) [58]. Figure 6-10 shows a graph of the dose rate of spent fuel over time and points out when the intrinsic barrier is lost.

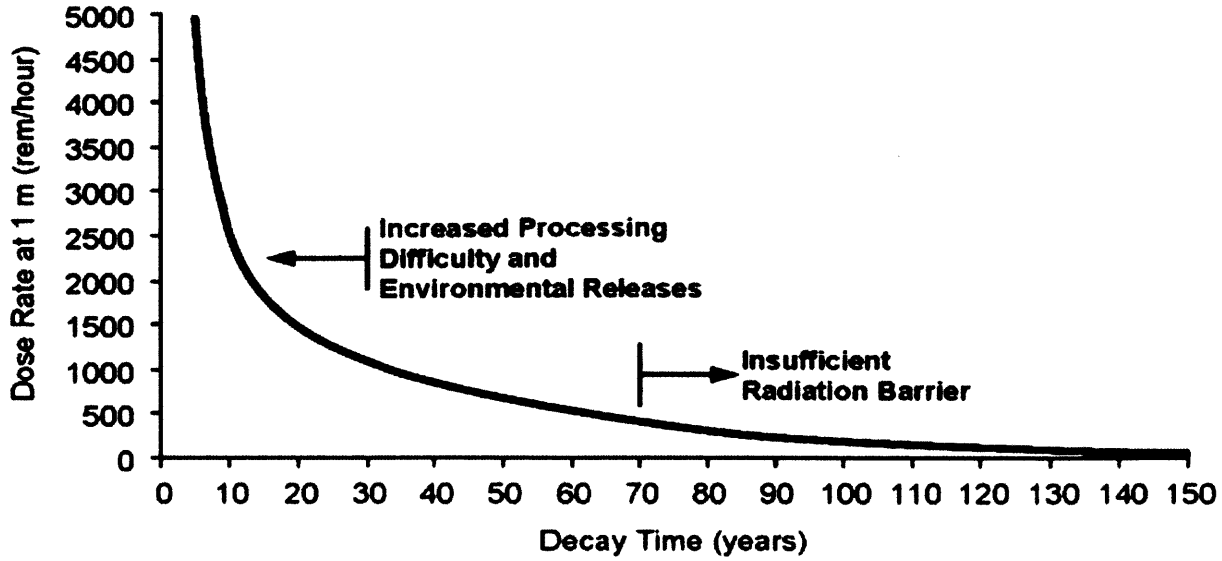

Figure 6-10. Dose rate at one meter from a Westinghouse PWR assembly with 50 GW-d/MTU burnup, as a function of time discharged from a reactor [58].

If safety (and not economic) concerns are the only reason for retrievability, the final repository selection will benefit, simply by virtue of having a greater number of design options to initially choose from. A constant effort to uphold a dual mission could impact long term repository performance [57]. In conclusion, if retrievability is limited to safety reasons, deep boreholes are fully retrievable in that context, and should be strongly considered among the alternatives to the Yucca Mountain repository.

6.8. Chapter Summary

Many factors contribute to the feasibility of nuclear waste disposal processes, but the primary concerns are based on safety and economics. The proposed method's safety is confirmed in terms of thermal and structural issues, and supporting data is drawn from prior DOE experience with the design of robust waste canisters. The issue of backfill with buffers or lubricants (not yet fully designed or resolved) is discussed in the context of water flooded borehole conditions. A cost comparison between the drop-in and drill-string methods shows that the former is clearly favored, even when the drill-string method is assumed to have optimistically fast lowering speeds. Finally, the policy implications of retrievability requirements with respect to DBWD and other repositories are outlined, and DBWD is concluded to be retrievable within a technical (and not necessarily economic) definition.

7. Summary, Conclusions, and Recommendations

7.1. Summary

Use of deep boreholes to contain nuclear waste has been gaining more attention as pressures to deal with nuclear waste rise. The recent earthquakes, tsunami and nuclear accidents in Fukushima, Japan have publicly highlighted the safety vulnerabilities of spent fuel pool storage, and will cause the U.S. and many other countries to look critically at how waste is stored. The public's desire to remove fuel from the onsite pools is complemented by the utilities' desire to remove fuel from their plant sites altogether, to a central facility as promised by the government. However, the Obama administration has rejected and permanently put a hold on the decades-long evaluated Yucca Mountain repository, and policy makers and scientists are back to evaluating all geologies and repository designs [2].

The complexity and cost of the emplacement procedure is a challenge to any repository concept's feasibility. A spent fuel assembly produces a high radiation field, is highly dense and produces almost 1 kW of heat. This necessitates complex shielding and handling procedures, commonly completed robotically and remotely. Particularly for DBWD, emplacement is an area of work that in the past, has received inadequate attention compared to drilling costs, canister design and thermal analysis. This study proposed and evaluated a fast procedure for emplacement of canisters which reduces mechanical and radiation handling requirements. The proposed method is to release the canisters into a water-flooded borehole with its velocity moderated by drag forces developed in the fluid flow process. An analytical model, dimensional analysis, and $1/5^{th}$ scale experiments were successfully completed.

7.2. Conclusions

The reference canister design is a 0.34 meter OD steel drill casing, which when inserted into the lining results in an annular gap of 2.35 cm. When the borehole is flooded with water and the canister is released, the water in the gap is forced to travel in the opposing direction of the canister. Using basic fluid conservation and force equations, it was derived that the water would move at 3.36 times the speed of the canister. This generates large shear forces and a pressure drop in the fluid, slowing the canister down. Combined with dimensional analysis, the analytical solutions produced a very simple relation to describe the velocity of fluid and canister in terms of

fundamental parameters describing the geometry, buoyancy and friction factor of the canister and fluid flow (see Eq. (4-14)). The model was validated by 81 successful drop tests and produces a predicted a maximum velocity of 2.4-2.6 m/s (5.3-5.8 mph) for the full scale case. Further tests increased canister surface roughness and form losses, as a means to reduce the velocity of the canister even further. The results showed that if a hydraulically rough surface could be achieved on the full scale canister (through the attachment of 1.92mm particles to the surface) the canister's velocity could be reduced by almost 50% to 1.25 m/s. A basic structural analysis and comparison showed that this energy could easily be absorbed with a metal skirt attached to the front of the canister. An economic study based on previously documented billing rates and drill string lowering speeds concluded that the drop-in method drastically reduces the cost and time of emplacement compared to a drill string method, by at least 70%. Overall, the costs of emplacement for this method are estimated to be $700,000 per borehole, or $3.5/kg HM, which is a very small fraction of the total $400 kg/HM appropriated for waste disposal. The primary source of savings is the fact that the drilling rig does not have to be employed while the canisters are traveling down the borehole (on average 3km). It is concluded that emplacement in deep boreholes deserves serious investigation among the repository alternatives, as an economically feasible and highly isolating method of disposing of waste.

7.3. Recommended Future Work

7.3.1. Discounted Economic Analysis of Borehole Construction and Emplacement

A key differentiator of DBWD is that it is modular, as opposed to all other mined repository designs which rely on significant upfront investment to establish. With boreholes, only as many holes as are currently needed are drilled (the economically optimal solution). Boreholes can be drilled and filled sequentially, as opposed to being mined all at once, and filled all at once. This allows for investments to be delayed as far into the future as possible. Economic comparisons between deep boreholes with other repositories should incorporate the time value of money and use a non-zero discount rate. It should also take into account the probability that the repository fails politically and the investment must be recouped. In the case of a mined repository, if the licensing fails after the initial mines have been dug, there is no way to recoup the massive investment (as was the case with Yucca mountain). However, if a similar event occurs with a DBWD design, the sunk cost would be the drilling and site characterization costs for a single

borehole. Lastly, this modularity and cost effectiveness at small scales would be very beneficial in the case that U.S. decided on having many regional repositories rather than a single large repository. These effects might also make borehole disposal attractive for smaller national nuclear power programs.

7.3.2. Comparison of Radiation and Handling Risks with Other Repository Designs

One consequence of the limited of diameter boreholes (necessary to reduce drilling costs) is that it necessitates the insertion of each assembly into an individual canister. This tends to increase the number of transfers, thus risk of accidental drop. For example, Yucca mountain multipurpose waste packages were designed and suitable for transportation, aging and direct disposal (TAD). Based on a simple probabilistic analysis, the total number of transfers was not expected to result in an accidental drop [59]. A preliminary survey of these probabilities is shown in Table 7-1, and a reasonable estimate is 1×10^{-5} failures/transfer.

Table 7-1. Summary of various estimates of failure probabilities during handling of spent fuel.

Probability	Comments	Source
5.6×10^{-5}	Heavy load drop rate (>30 MT) at commercial plants, after 1980	NUREG- 1774 [60]
1×10^{-5} to 1.5×10^{-4}	Probability of load drops based on Navy data	NUREG-0612 [61]
1×10^{-5}	Failure (drop) rate used by the DOE in the probabilistic hazard analysis (PHA) in the license application (LA) for Yucca mountain.	[59]
1- 5%	Failure of crane operator to follow a given procedure, estimated based on Navy data	NUREG-0612 [61]
5.6×10^{-6}	Combined equipment failure rate per demand, estimated for the TRUDOCK crane system at the Waste Isolation Pilot Plant (WIPP)	[62]

If a similar approach [59] is applied to DBWD, assuming 2 transfers per assembly (one out of transportation cask, one into waste canister) and a 100 MTHM repository is required (resulting in appx. 240,000 canisters), multiple drops are expected to occur. Figure 7-1 shows the estimated probability distribution of drops during loading of a deep borehole repository.

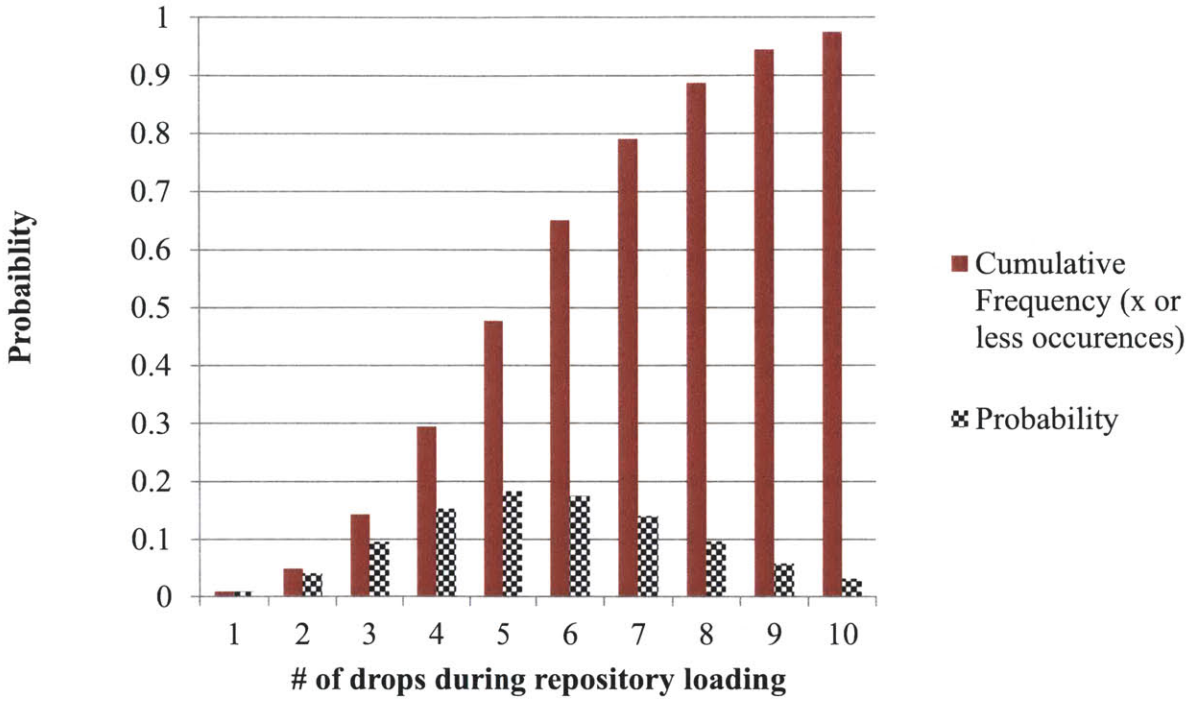

Figure 7-1. Estimated number of drops during the loading of a 100 MTHM deep borehole respository, assuming a binomial distribution of failures and a failure rate of 1×10^{-5}.

Future work could examine the consequences of such accidental drops, in terms of radiological risk to workers and offsite dose consequences. Methods of integrating storage and transportation canister design with disposal canister design could also be investigated to minimize the number of transfers required. Furthermore, the understanding of human error with respect to crane failures should be expanded, and quantified in the context of a SNF repository. The risk of accidental drop can also be applied to further demonstrate the benefit of the drop-in method over the drill string method, which is only feasible if canisters can be interconnected or lowered at very high speeds.

References

[1] Key Attributes, Challenges, and Costs for the Yucca Mountain Repository and Two Potential Alternatives, U.S Government Accountability Office, 2009.

[2] F.D. Hansen, E. Hardin, and A. Orrell, Geologic Disposal Options in the USA, Proceedings of the International High Level Waste Conference. Albuquerque, NM: 2011.

[3] J. Inhofe, Yucca Mountain: The Most Studied Real Estate on the Planet, U.S. Senate Committee on Environment and Public Works, 2006.

[4] K. Cawley, The federal government's responsibilities and liabilities under the Nuclear Waste Policy Act, Presented before the Committee on the Budget of the U.S. House of Representatives, 2009.

[5] S. Ansolabehere, J. Deutch, and M. Driscoll, The Future of Nuclear Power: An Interdisciplinary MIT Study, Cambridge, MA: Massachusetts Institute of Technology, 2010.

[6] M. Kazimi, E. Moniz, and C. Forsberg, The Future of the Nuclear Fuel Cycle, MIT, 2010.

[7] M. Bunn, J. Holdren, and S. Fetter, "The Economics of Reprocessing versus Direct Disposal of Spent Nuclear Fuel," Fuel Cycle and Management, vol. 150, Jun. 2005.

[8] J. Deutch, C. Forsberg, and A. Kadak, Update to the MIT 2003 Future of Nuclear Power: An Interdisciplinary MIT Study, Cambridge, MA: Massachusetts Institute of Technology, 2009.

[9] Y. Polsky and L. Capuano et al, Enhanced Geothermal Systems (EGS) Well Construction Technology Evaluation Report, Sandia National Laboratory, 2008.

[10] J. Tester and B. Anderson, The Future of Geothermal Energy, Cambridge, MA: Massachusetts Institute of Technology, 2006.

[11] N. Chapman and F. Gibb, "A Truly Final Waste Management Solution," Radwaste Solutions, vol. 10, Aug. 2003.

[12] C. Hoag, "Canister Design for Deep Borehole Disposal of Nuclear Waste," S.B Thesis, MIT Department of Nuclear Science and Engineering, 2006.

[13] P. Brady, B. Arnold, and G. Freeze, Deep Borehole disposal of High level Radioactive waste, Albuquerque, NM: 2009.

[14] B. Arnold, P. Swift, and P. Brady, "Radwaste Management: Deep Boreholes," Nuclear Engineering International, vol. 55, Feb. 2010.

[15] Project on Alternative Systems Study (PASS), SKB TR-93-04, 1993.

[16] K. Jensen and M. Driscoll, Policy Issues Associated with Deep Borehole HLW Disposal, Proceedings of the International High Level Waste Conference. Albuquerque, NM: 2011.

[17] J. Gibbs, "Feasibility of Lateral Emplacement in Very Deep Borehole Disposal of High Level Nuclear Waste," Naval Engineer and Nuclear Engineer Thesis, MIT, 2010.

[18] S. Kubota, S. Suzuki, and K. Ishiguro, Improvement of Repository Concepts for Realistic Underground Environmental Conditions in Japan, Proceedings of the International High Level Waste Conference. Albuquerque, NM: 2011.

[19] F. Kendorksi, "Review and Critique of Drip Shield Concept and Retrieval Concept Planned for the Yucca Mountain Project, Nevada," Nov. 2005.

[20] F. Bierich and M. Prytherch, Concepts for Waste Retrieval and Alternate Storage of Radioactive Waste, Las Vegas, Nevada: Bechtel SAIC Company LLC, 2005.

[21] V. Arakali, E. Faillace, and A. Linden, Subsurface Facility Worker Dose Assessment, Office for Civilian Radioactive Waste Management, 2004.

[22] R. Thornly, Emplacement Gantry Gap Analysis Study, Las Vegas, Nevada: Bechtel SAIC Company LLC, 2005.
[23] C. Julin and H. Sandstedt, Storage of nuclear waste in very deep boreholes: Feasibility study and assessment of economic potential.Part I Geological Considerations. Part II Overall facilities plan and cost analysis, SKB, 1989.
[24] C. Augustine, J. Tester, and B. Anderson, "A Comparison of Geothermal with Oil and Gas Well Drilling Costs," Proceedings of the Thirty First Workshop on Geothermal Reservoir Engineering. Stanford, CA: 2006.
[25] Natural Gas- Data- U.S Prices, U.S Energy Information Administration. Accessed at http://www.eia.doe.gov/dnav/ng/ng_pri_sum_dcu_nus_m.htm on April 28,, 2011.
[26] U.S Energy Information Administration, Petroleum and Other liquids- Annual Cushing, OK West Texas Intermediate (WTI) Crude oil spot price, 2011.
[27] U.S Energy Information Administration, "Petroleum and Other liquids- World Crude Oil Prices," 2011.
[28] U.S Energy Information Administration, "Short-Term Energy and Summer Fuels Outlook," Apr. 2011.
[29] T. Harrison, Very Deep Borehole: Deutag's opinion on boring, canister emplacement and retrievability, SKB, 2000.
[30] Woodward Clyde Consultants, Very Deep Hole Systems Engineering Studies, Battelle Memorial Institue, 1983.
[31] K. Macdonald and W. Deans, "Stress analysis of drillstring threaded connections using the finite element method," Engineering Failure Analysis, vol. 2, Mar. 1995, pp. 1-30.
[32] A. Tafreshi and W. Dover, "Stress analysis of drillstring threaded connections using the finite element method," International Journal of Fatigue, vol. 15, 1993, pp. 429-438.
[33] M. Veidt and A. Berezovski, "Design and Application Of A Drill Pipe Fatigue Test Facility," Structural Integrity and Failure, 2004.
[34] S.-J. Chen, Q. An, Y. Zhang, and L.-X. Gao, "Loading Analysis on the Thread Teeth in Cylindrical Pipe Thread Connection," Journal of Pressure Vessel Technology, vol. 132, Jun. 2010.
[35] U.S. steel, Tubular Products, Product Descriptions, Accessed at http://www.ussteel.com/corp/tubular/tubular-soctg.asp on April,, 2011.
[36] I. Lotsberg, "Stress concentration factors at welds in pipelines and tanks subjected to internal pressure and axial force," Marine Structures, vol. 21, Apr. 2008, pp. 138-159.
[37] I. Lotsberg, "Stress concentration factors at circumferential welds in tubulars," Marine Structures, vol. 11, Jul. 1998, pp. 207-230.
[38] M. Markey, Handbook of Oceanographic Winch, Wire and Cable Technology, National Science Foundation, 2001.
[39] K. Bram, "The KTB Borehole: Germany's Superdeep Telescope into the Earth's Crust," Oilfield Review, vol. 7, Feb. 1995.
[40] M. Driscoll and K. Jensen, "Deep Borehole Attributes and Performance Requirements," MIT Nuclear Fuel Cycle Technology and Policy Program MIT-NFC-TR-113, Apr. 2010.
[41] K. Skinner, C. Shelton-Davis, and G. Housley, "Yucca Mountain Waste Package Closure System," Idaho National Lab, 2005.
[42] E.E. Hudon and J.E. McCleery, Retrieval System for Emplaced Spent Unreprocessed Fuel (SURF) in Salt Bed Depository, Lawrence Livermore Laboratory, 1979.

[43] A. Hosoi, MIT Course 2.006: Thermal Fluids Engineering Course text, Cambridge, MA: MIT, 2009.
[44] D. Kaminski and M. Jensen, Introduction to Thermal and Fluids Engineering, Hoboken, NJ: John Wiley and Sons, 2005.
[45] "Chapter 5 : Equations of Motion and Mechanical Energy, Losses Due to Sudden Contraction," Fluid Mechanics. IIT Kanpur. Accessed at http://nptel.iitm.ac.in/courses/Webcourse-contents/IIT-KANPUR/FLUID-MECHANICS/lecture-14/14-7_losses_sudden_contract.htm on May 5, 2011.
[46] M. Marriot and R. Jayaratne, "Hydraulic Roughness- Links Between Manning's Coeeficient, Nikuradse's Equivalent Sand Roughness and Bed Grain Size," Advances in Computing and Technology, University of East London: 2010.
[47] K. Orvis and H. Grissino-Mayer, "Standardizing the Reporting of Abrasive Papers Used to Surface Tree Ring Samples," Tree Ring Research, vol. 58, 2002, pp. 47-50.
[48] B. Mell, Topography and Roughness Testing of Sandpaper Surface, Irvine, California: Nanovea, 2010.
[49] C. Sizer, "Minor Actinide Waste Disposal in Deep Geological Boreholes," S.B Thesis, MIT Department of Nuclear Science and Engineering, 2006.
[50] R. Kenneally and J. Kessler, "Behavior of Spent Fuel and Safety-Related Components in Dry Cask Storage Systems," Transactions SMiRT, Washington D.C: 2001.
[51] S.D. Snow, D.K. Morton, T.E. Rahl, A.G. Ware, and N.L. Smith, Analytical Evaluation of Drop Tests Performed on Nine 18-inch Diameter Standardized DOE Spent Nuclear Fuel Canisters, Idaho National Engineering and Environmental Laboratory, 2007.
[52] R.K. Blandford, D.K. Morton, T.E. Rahl, and S.D. Snow, "Preventing Failure in Spent Nuclear Fuel Canisters," Practical Failure Analysis, vol. 3, Aug. 2003.
[53] T.L. Bridges, A.L. Lengyel, D.K. Morton, and D.L. Pincock, Standardized DOE Spent Nuclear Fuel Canister And Transportation System For Shipment To The National Repository, Waste Management Conference Tucson, AZ: Idaho National Engineering and Environmental Laboratory, 2001.
[54] J. Nikuradse, Laws of Flow in Rough Pipes, National Advisory Committee for Aeronautics, 1950.
[55] J.N. Dumont and C. Pescatore, International Retrievability Scale for Waste in Geological Disposal, Proceedings of the International High Level Waste Conference. Albuquerque, NM: 2011.
[56] R. Rechard, C. Thomas, M. Nutt, and J. Carter, Technical Lessons to Learn in Disposal of Spent Nuclear Fuel and High-Level Waste, Proceedings of the International High Level Waste Conference. Albuquerque, NM: 2011.
[57] C. Forsberg, Alternative Fuel-Cycle Repository Designs, Proceedings of the International High Level Waste Conference. Albuquerque, NM: 2011.
[58] E.D. Collins, B.B. Spencer, and M. Del Cul, Importance of Decay Time on HLW Disposal, Proceedings of the International High Level Waste Conference. Albuquerque, NM: 2011.
[59] L. et al Spradley, "Frequencies of drop events during preclosure at Yucca Mountain," Nuclear Technology, vol. 170, May. 2010.
[60] R.L. Lloyd, A Survey of Crane Operating Experience of U.S. Nuclear Power Plants from 1968 through 2002, U.S. Nuclear Regulatory Commission, 2003.
[61] H. George, Control of Heavy Loads at Nuclear Power Plants: Resolution of Generic Technical Activity, Nuclear Regulatory Commission, 1980.

[62] M. Greenfield and T. Sargent, Probability of Failure of the TRUDOCK Crane System at the Waste Isolation Pilot Plant (WIPP), Environmental Evaluation Group, 2000.
[63] P.C. Chu, "Experiment of Falling Cylinder through the Water Column," Experimental Thermal and Fluid Science, vol. 29, 2005, pp. 555-568.
[64] F. Incropera and D. DeWitt, Fundamentals of Heat and Mass Transfer, Hoboken, NJ: John Wiley and Sons, 2002.

Appendix A. Derivation of Canister Velocity Solutions

A.1 Introduction

The accuracy of the analytical derivation was crucial to gaining insights into the experimental design and scaling of the results. The models begin with simplifying assumptions and first principles of fluid flow.

A.2 Force and Momentum Balance

Summing up the forces that act on the canister when it has achieved terminal velocity, we have:

$$\sum Forces = P_1 A_C + \tau\pi D_C l - P_2 A_C - Mg = 0 \tag{A-1}$$

$$A_C = \frac{\pi}{4} {D_C}^2 \tag{A-2}$$

$$\tau = \frac{f}{8} \rho_f {V_f}^2 \tag{A-3}$$

$$M = \rho_C V = \rho_C A_C l = \rho_c \frac{\pi}{4} {D_C}^2 l \tag{A-4}$$

Combining all the expressions and solving for $P_1 - P_2$,

$$P_1 - P_2 = \rho_C g l - \frac{\rho_f {V_f}^2}{2} f\left(\frac{l}{D_C}\right) \tag{A-5}$$

Figure A-1 shows a diagram of the relevant velocities in a stationary frame of reference and control volume.

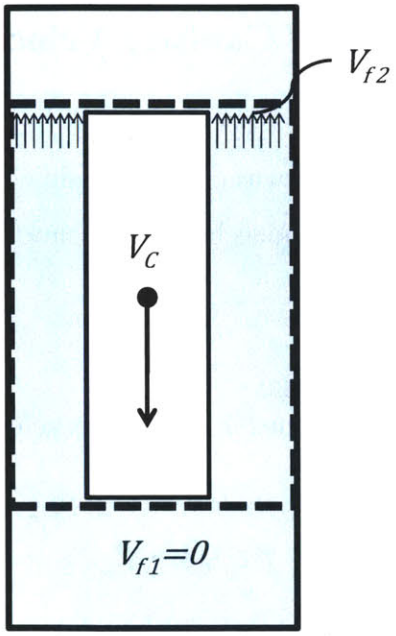

Figure A-1. Definition of canister and water velocities and control volume, with a stationary frame of reference. V_{f1}, V_{f2}, are the average velocities of the fluid at reference point 1 and 2, respectively.

To calculate the pressure drop in the annulus, it is assumed that the flow in the annulus is "fully developed" and can be described with initial and final average velocities V_{f1} and V_{f2}. This assumption is validated later by the fact that the model and experiments show the Reynolds number is in the range 10^4-10^6. To verify that entrance effects are not significant Eq. (A-6) [44] is tested,

$$\frac{Turblent\ Entry\ Length}{D_h} = 4.4(Re)^{0.6} \tag{A-6}$$

where an entry length/hydraulic diameter ratio of approximately 40 is obtained. This is small compared to the actual l/D_c, which is approximately 100, and therefore entrance effects are assumed to be negligible. Overall, the pressure drop/length in the entry region is higher than the fully developed region. Therefore, assuming fully developed flow will cause the fluid pressure drop to be underestimated (and thus the terminal velocity to be overestimated).

Using a momentum balance on the fluid which takes into account all hydraulic losses,

$$\Delta P = P_1 - P_2 = Frictional + Gravitational \tag{A-7}$$

$$= \frac{\rho_f {V_{f_2}}^2}{2}\left(f\frac{l}{D_h} + K_{form}\right) + \rho_f g(z_2 - z_1) \tag{A-8}$$

$$P_1 - P_2 = \frac{\rho_f {V_{f_2}}^2}{2}\left(f\frac{l}{D_h} + K_{form}\right) + \rho_f g l \tag{A-9}$$

A.3 Closed Boundary Condition

In order to eliminate the fluid velocity from the equations above, the continuity equations must be applied to the control volume. As the canister moves downwards, according to the closed boundary condition assumption the water volume it displaces will be forced to flow through the annulus. The continuity relation, where V_c and V_{f2} are the magnitudes of the velocities yields a ratio of fluid to canister velocity, Eq. (A-13).

$$0 = Volume\ entering - Volume\ Exiting \tag{A-10}$$

$$0 = V_{f_2} A_{C(Annulus)} - V_C A_{C(Canister)} \tag{A-11}$$

$$0 = V_{f_2}\frac{\pi}{4}\left[(D_C + D_h)^2 - {D_C}^2\right] - V_C\left(\frac{\pi}{4}{D_C}^2\right) \tag{A-12}$$

$$solving\ for\ \frac{V_{f_2}}{V_C},$$

$$\frac{V_{f_2}}{V_C} = \frac{{D_C}^2}{D_h(2D_C + D_h)} = V_{ratio} \tag{A-13}$$

The relative velocity of the water to the canister surface is greater than the water's velocity in the stationary frame of reference. Thus if the latter were assumed as the velocity of the water in the gap, it would greatly underestimate the frictional forces on the canister. To take this into account, the reference is shifted by a constant velocity. This is acceptable because the momentum, continuity and energy equations apply in any frame of reference, as long as the frame is not accelerating. The result of this frame of reference shift is shown in Figure A-2.

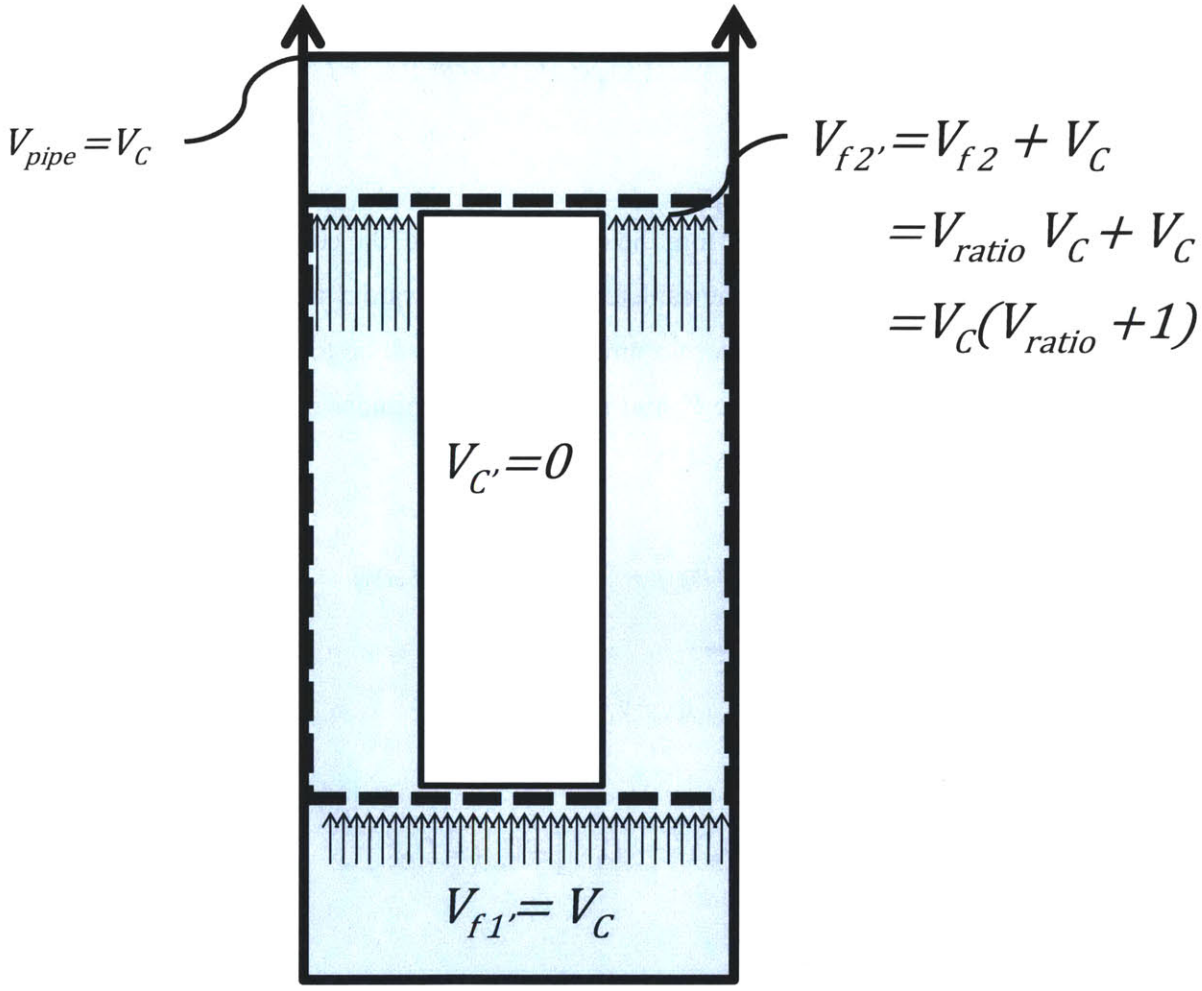

Figure A-2. Velocities in the frame of reference where the constant, terminal velocity is subtracted from all bodies. The new shifted velocities are denoted with a (').

The key relation obtained from the continuity and shift of reference frame for analysis is Eq. (A-14),

$$V_{f_{2\prime}} = V_C(V_{ratio} + 1) \tag{A-14}$$

The momentum equations and force balance equations can now be applied in this moving frame of reference, which takes into account the relative motion of the fluid and the canister. The calculation of the friction factor in the annulus will be slightly overestimated in this frame of reference, because the outer pipe has a small velocity that is in the same direction as the water flowing in it. However, because of the larger velocity gradient near the surface of the canister, most of the shearing will occur there, and thus it is more important to accurately model that phenomenon/region. Overall, these relationships conveniently allow for the elimination of all the shifted velocities, because all velocities can be represented in terms of V_c, the canister velocity in a stationary frame of reference. Eliminating $P_1 - P_2$ by combining the force balance for the canister, Eq. (A-5) and the momentum balance, Eq.(A-9),

$$\rho_c g l - \frac{\rho_f {V_{f_{2\prime}}}^2}{2}\left(f\frac{l}{D_c}\right) = \frac{\rho_f {V_{f_{2\prime}}}^2}{2}\left(f\frac{l}{D_h} + K_{form}\right) + \rho_f g l \tag{A-15}$$

$$2gl\left(\frac{\rho_c}{\rho_f} - 1\right) = {V_{f_{2\prime}}}^2\left(f\frac{l}{D_h} + K_{form} + f\frac{l}{D_c}\right) \tag{A-16}$$

substituting in $V_{f_2\prime}$, *from Eq.* (A-14),

$$2gl\left(\frac{\rho_c}{\rho_f} - 1\right) = [V_C(V_{ratio} + 1)]^2\left[f\left(\frac{l}{D_h} + \frac{l}{D_c}\right) + K_{form}\right] \tag{A-17}$$

solving for V_C,

$$2gl\left(\frac{\rho_c}{\rho_f}-1\right)=[V_C(V_{ratio}+1)]^2\left[f\left(\frac{l}{D_h}+\frac{l}{D_c}\right)+K_{form}\right] \tag{A-18}$$

$$V_C=\sqrt{\frac{2gl\left(\frac{\rho_c}{\rho_f}-1\right)}{\left[f\left(\frac{l}{D_h}+\frac{l}{D_c}\right)+K_{form}\right](V_{ratio}+1)^2}} \tag{A-19}$$

A.4 Open Boundary Condition

In this bounding and conservative condition, the volume of the water beneath the canister is assumed to be free to flow downwards. Therefore, as the canister moves downwards, the water displaced by the canister will be not forced to flow through the annulus. As a result, there will be no velocity multiplication effect (as described by V_{ratio}) and therefore V_{ratio}=1. This results in larger predicted canister velocities because the velocity gradient and shear forces on the surface of the canister are smaller. In this situation, analysis of the boundary layer will be critical to understanding the forces on the canister. In fact, if the boundary layer is small compared to the actual gap, then the solution is theoretically no different from the case in which the canister is allowed to free fall in a pool of water. Three approaches – flat plate theory, coefficient of drag, and von Karman's universal defect method are discussed.

One approach assumes that flat plate theories approximate the annular flow (in an external flow configuration, as opposed to a fully developed internal flow). Under these assumptions, the only net upward force results from skin friction (there will be no net upward force from the pressure drop of the flowing fluid). Overall, this will be shown to result in an overly conservative and unphysical estimate for the terminal velocity. The important parameter definitions are:

$$Equivalent\ Plate\ Length = l \tag{A-20}$$

$$Equivalent\ Plate\ Width = \pi D_c \tag{A-21}$$

$$Re_l = \frac{\rho_f \, l \, V_C}{\mu} \tag{A-22}$$

The turbulent coefficient of drag (C_d) (from viscous forces) and drag force (F_d) for flow across a smooth flat plate, for $Re_l > 10^7$ is given in Eq. (A-23) and Eq. (A-24) [43],

$$C_d = 0.031 Re_l^{-\frac{1}{7}} = 0.031 \left(\frac{\rho_f \, l \, V_C}{\mu}\right)^{-\frac{1}{7}} \tag{A-23}$$

$$F_D = C_D \left[\frac{\rho_f V_c^{\,2}}{2} (Width)(Length)\right] \tag{A-24}$$

Combining Eq. (A-23) and Eq. (A-24) yields Eq.(A-25)

$$F_D = C_D \left[\frac{\rho_f V_c^{\,2}}{2} \pi D_c l\right] \tag{A-25}$$

$$F_D = 0.031 \left(\frac{\rho_f \, l \, V_C}{\mu}\right)^{-1/7} \left[\frac{\rho_f V_c^{\,2}}{2} \pi D_c l\right] \tag{A-26}$$

$$F_D = 0.031 \left(\rho_f l\right)^{6/7} \left[\frac{V_c^{\,13/7}}{2} \pi D_c \mu^{1/7}\right] \tag{A-27}$$

In the steady state, according to a force balance (which assumes a zero pressure gradient from viscous losses because this is not internal flow), the upward drag force must be equivalent to the net downward force from gravity (F_g):

$$F_g = Mg = \left(\rho_c - \rho_f\right) \frac{\pi}{4} D_C^{\,2} l \, g \tag{A-28}$$

$$F_g = F_D \tag{A-29}$$

combining Eq. (A-28) and Eq. (A-29) yields Eq. (A-30),

$$(\rho_c - \rho_f)\frac{\pi}{4}{D_C}^2 l\, g = 0.031\,(\rho_f l)^{6/7}\left[\frac{{V_c}^{13/7}}{2}\pi D_c \mu^{1/7}\right] \tag{A-30}$$

solving for V_c gives Eq. (A-31),

$$V_c = \left[\frac{(\rho_c - \rho_f)D_c g\, l^{1/7}}{(0.062){\rho_f}^{6/7}\mu^{1/7}}\right]^{7/13} \tag{A-31}$$

Substituting in the geometric properties from the reference canister design (which has a surface area of only 5.34 m^2 results in a Re_l= 2.88 x 10^8, C_d= 1.9 x 10^{-3}, V_c of 54.4 m/s, which is clearly unphysical. The size of the boundary layer can be compared against the maximum size of the gap thickness of 0.0235 m [43],

$$\delta(x = l) = 0.37l\left(\frac{\rho_f v_\infty l}{\mu}\right)^{-1/5} = 0.37l(Re_l)^{-1/5} \tag{A-32}$$

where $v_\infty = V_c$. This yields a δ_{max}= 0.0375m, which is larger than the gap that the boundary layer is constrained to fit in. The unphysical result from this model; however, shows that (in this case of a hydraulically smooth pipe) skin friction losses in the boundary layer are small. Therefore drag/form losses (occurring in the wake of the canister) have an important effect that must be taken into account.

The drag coefficient for axial flow along the cylinder C_D is less dependent on the axial Reynolds number when $Re_{axial} > 10^4$, is a function of the aspect ratio *l/d,* and is shown as Eq. (A-33) [63],

$$Re_{axial} = \frac{\rho_f D_c V_C}{\mu} \tag{A-33}$$

$$C_D = 1 \ , \quad for \frac{l}{d} > 8$$

$$F_D = C_D \left[\frac{\rho_f {V_c}^2}{2} (Area) \right] \tag{A-34}$$

Substituting the area of the canister,

$$F_D = C_D \left[\frac{\rho_f {V_c}^2}{2} (\frac{\pi}{4} {D_C}^2) \right]$$

$$F_D = \left[\frac{\rho_f {V_c}^2}{8} (\pi {D_C}^2) \right] \tag{A-35}$$

Aaccounting for the force of gravity,

$$F_g = Mg = (\rho_c - \rho_f) \frac{\pi}{4} {D_C}^2 l \, g \tag{A-36}$$

According to a force balance on the canister at terminal velocity,

$$F_g = F_D \tag{A-37}$$

Combining Eq.(A-35) and Eq.(A-36) gives Eq. (A-38),

$$(\rho_c - \rho_f) \frac{\pi}{4} {D_C}^2 l \, g = \left[\frac{\rho_f {V_c}^2}{8} (\pi {D_C}^2) \right] \tag{A-38}$$

Solving for V_c,

$$V_c = \left[\frac{(\rho_c - \rho_f)2g\,l}{\rho_f}\right]^{1/2} \tag{A-39}$$

Substituting the reference values [12], a physically feasible canister terminal velocity of 18.3 m/s is obtained, with a Re_{axial} of 6.6 x 10^6. Calculating the maximum size of the boundary layer from [63] gives Eq. (A-40)

$$\delta = 0.16l(Re_{axial})^{-1/7} = 0.0849\text{m} \tag{A-40}$$

In this case, the boundary layer is nearly 4 times larger than the actual gap that it is constrained to fit in. Therefore, the assumption of external flow is not valid, and can only be used to obtain an upper bound estimate of the canister velocity. In reality, viscous effects in the boundary will be more important because the boundary layer is forced to fit in such a small gap. In addition there are actually two boundary layers (one extending from the pipe wall, where the velocity of the fluid must be zero, and the other extending from the canister, where the velocity must be equal to that of the canister). The difference in boundary layers will cause further viscous losses.

A method of getting a "best estimate" for the canister velocity in this case requires developing an approximation for the turbulent velocity distribution (using von Karman's "universal defect or "middle law" for example). Applying von Karman's "universal defect" velocity distribution (which can be used in any geometry) with the conditions that the velocity is a maximum at the surface of cylinder and zero at the outer wall:

The velocity boundary conditions apply,

$$V_x(r = R_c) = V_{max} = V_c$$
$$V_x(r = R_l) = V_x(r = (R_c + t)) = 0,$$

where R_l is the radius of the outer lining, t is the gap size, and R_c is the radius of the canister. According to the Universal Defect law [43],

$$V_{max} - V_x(y) = V^* g\left(\frac{y}{r}\right) \tag{A-41}$$

Where y is the distance from the conduit (outer pipe wall) and r is the radial distance from the centerline,

$$y = R_l - r = (R_c + t) - r \tag{A-42}$$

and g (the universal function) in the turbulent boundary is[43]:

$$V^+ = 2.44\ln(y^+) + 5 \tag{A-43}$$

Combining Eqs. (A-41), (A-42) and (A-43) gives Eq. (A-44),

$$\frac{V_x}{V^*} = 2.44\ln\left(\frac{yV^*}{\nu}\right) + 5 \quad = 2.44\ln\left(\frac{yV^*}{\nu}\right) + 5 \quad = 2.44\ln\left[\frac{(R_c + t - r)V^*}{\nu}\right] + 5 \tag{A-44}$$

Evaluating Eq. (A-44) at the surface of the canister at R_{cyl} (where $V_x = V_{max}$) gives Eq. (A-45),

$$\frac{V_{max}}{V^*} = 2.44\ln\left[\frac{(R_c + t - R_c)V^*}{\nu}\right] + 5$$

$$\frac{V_{max}}{V^*} = 2.44\ln\left(\frac{tV^*}{\nu}\right) + 5 \tag{A-45}$$

Subtracting Eq. (A-44) from Eq.(A-45) and rearranging gives Eq.(A-46),

$$\frac{V_{max} - V_x}{V^*} = 2.44\ln\left[\frac{t}{R_l - r}\right]$$

$$V_x = V_{max} - V^* \left[2.44\ln\left(\frac{t}{R_l - r}\right)\right] \tag{A-46}$$

Evaluating the average velocity in this flow geometry,

$$V_{avg} = \frac{\dot{V}}{A_c} = \frac{1}{A_c}\int_{R_c}^{R_l} V_x 2\pi r dr$$

$$= \frac{2\pi}{\pi({R_l}^2 - {R_c}^2)}\int_{R_c}^{R_l} V_x r dr$$

$$= \frac{2}{({R_l}^2 - {R_c}^2)}\int_{R_c}^{R_l}\left(V_{max} - V^*\left[2.44\ln\left(\frac{t}{R_l - r}\right)\right]\right) r dr$$

$$= \frac{2}{({R_l}^2 - {R_c}^2)}\left[\int_{R_c}^{R_l} V_{max} r dr - \int_{R_c}^{R_l} V^*\left[2.44\ln\left(\frac{t}{R_l - r}\right)\right] r dr\right]$$

$$= \frac{2}{({R_l}^2 - {R_c}^2)}\left[\int_{R_c}^{R_l}(V_{max} - V^* 2.44\ln(t)) r dr + \int_{R_c}^{R_l} V^*[2.44\ln(R_l - r)] r dr\right]$$

$$= \frac{2}{({R_l}^2 - {R_c}^2)}\left[\left(V_{max} - V^* 2.44\ln(t)\right)\frac{r^2}{2}\Big|_{R_c}^{R_l} + \int_{R_c}^{R_l} V^*[2.44\ln(R_l - r)] r dr\right]$$

$$= \frac{2}{({R_l}^2 - {R_c}^2)}\left[[V_{max} - V^* 2.44\ln(t)]\frac{{R_l}^2 - {R_c}^2}{2} + \int_{R_c}^{R_l} V^*[2.44\ln(R_l - r)] r dr\right]$$

$$V_{avg} = [V_{max} - V^* 2.44\ln(t)] + \frac{2}{({R_l}^2 - {R_c}^2)}\int_{R_c}^{R_l} V^*[2.44\ln(R_l - r)] r dr$$

$$V_{avg} = [V_{max} - V^{*}2.44\ln(t)] + \frac{4.88V^{*}}{({R_l}^2-{R_c}^2)}\left[\frac{-{R_l}^2}{2} ln(r-R_l) + \frac{r^2}{2} ln(R_l - r) - \frac{R_l r}{2} - \frac{r^2}{4}\right]\Big|_{R_c}^{R_l}$$

$$=[V_{max} - V^{*}2.44\ln(t)] + \frac{4.88V^{*}}{({R_l}^2-{R_c}^2)}\left[\frac{-{R_l}^2}{2} ln(r-R_l) + \frac{r^2}{2} ln(R_l - r) - \frac{R_l r}{2} - \frac{r^2}{4}\right]\Big|_{R_c}^{R_l}$$

$$=[V_{max} - V^{*}2.44\ln(t)] + \frac{4.88V^{*}}{({R_l}^2-{R_c}^2)}\left[\frac{-{R_l}^2}{2}\left(ln(R_l-R_l) - ln(R_c-R_l)\right) + \frac{{R_l}^2}{2} ln(R_l - R_l) - \frac{{R_c}^2}{2} ln(R_l - R_c) - \frac{R_l(R_l-R_c)}{2} - \frac{{R_l}^2-{R_c}^2}{4}\right]$$

$$=[V_{max} - V^{*}2.44\ln(t)] + \frac{4.88V^{*}}{({R_l}^2-{R_c}^2)}\left[\frac{-{R_l}^2}{2}\left(ln\left(\frac{R_l-R_l}{R_c-R_l}\right)\right) + \frac{{R_l}^2}{2} ln(R_l - R_l) - \frac{{R_c}^2}{2} ln(R_l - R_c) - \frac{R_l(R_l-R_c)}{2} - \frac{{R_l}^2-{R_c}^2}{4}\right]$$

$$=[V_{max} - V^{*}2.44\ln(t)] + \frac{4.88V^{*}}{({R_l}^2-{R_c}^2)}\left[\frac{{R_l}^2}{2}\left(-ln\left(\frac{R_l-R_l}{R_l-R_c}\right) + ln(R_l - R_l)\right) - \frac{{R_c}^2}{2} ln(R_l - R_c) - \frac{R_l t}{2} - \frac{{R_l}^2-{R_c}^2}{4}\right]$$

$$=[V_{max} - V^{*}2.44\ln(t)] + \frac{4.88V^{*}}{({R_l}^2-{R_c}^2)}\left[\frac{{R_l}^2}{2}\left(ln\left(\frac{R_l-R_c}{(R_l-R_l)}(R_l-R_l)\right)\right) - \frac{{R_c}^2}{2} ln(R_l - R_c) - \frac{R_l t}{2} - \frac{{R_l}^2-{R_c}^2}{4}\right]$$

$$=[V_{max} - V^{*}2.44\ln(t)] + \frac{4.88V^{*}}{({R_l}^2-{R_c}^2)}\left[\frac{{R_l}^2}{2}\left(ln(R_l - R_c)\right) - \frac{{R_c}^2}{2} ln(R_l - R_c) - \frac{R_l t}{2} - \frac{{R_l}^2-{R_c}^2}{4}\right]$$

$$=[V_{max} - V^{*}2.44\ln(t)] + \frac{4.88V^{*}}{({R_l}^2-{R_c}^2)}\left[\left(\frac{{R_l}^2}{2} - \frac{{R_c}^2}{2}\right) ln(R_l - R_c) - \frac{R_l t}{2} - \frac{{R_l}^2-{R_c}^2}{4}\right]$$

$$V_{avg}=[V_{max}-V^{*}2.44\ln(t)]+\frac{2.44V^{*}}{(R_l{}^2-R_c{}^2)}\left[(R_l{}^2-R_c{}^2)ln(t)-R_l t-\frac{R_l{}^2-R_c{}^2}{2}\right]$$

$$=[V_{max}-V^{*}2.44\ln(t)]+2.44V^{*}\ln(t)-\frac{2.44V^{*}R_l t}{(R_l{}^2-R_c{}^2)}-1.22V^{*}$$

$$V_{avg}=V_{max}-\frac{2.44V^{*}R_l t}{(R_l{}^2-R_c{}^2)}-1.22V^{*}$$

$$V_{avg}=V_{max}-2.44V^{*}\left(1-\frac{tR_c}{(R_l{}^2-R_c{}^2)}\right)-1.22V^{*}$$

$$=V_{max}-3.66V^{*}-2.44V^{*}\left(\frac{tR_c}{(R_l{}^2-R_c{}^2)}\right)$$

$$V_{avg}=V_{max}-3.66V^{*}-2.44V^{*}\left(\frac{R_c}{(2R_c+t)}\right)$$

For $R_c>>t$,

$$V_{avg}=V_{max}-3.66V^{*}-1.22V^{*}$$

$$V_{avg}=V_{max}-2.44V^{*} \tag{A-47}$$

With the following definitions, the friction factor can be derived,

$$V^{*}=\sqrt{\frac{\tau_w}{\rho}} \tag{A-48}$$

$$\frac{\tau_w}{\rho}=\frac{f}{8}V_{avg}{}^2 \tag{A-49}$$

Therefore,

$$V^* = \sqrt{\frac{f}{8}} V_{avg} \tag{A-50}$$

Combining Eqs. (A-45), (A-47) and (A-50) gives Eq. (A-51),

$$V_{avg} = V^* 2.44 \ln\left(\frac{tV^*}{\nu}\right) + 5V^* - 2.44V^*$$

$$\frac{V_{avg}}{V^*} = 2.44 \ln\left(\frac{\sqrt{\frac{f}{8}} V_{avg} t}{\nu}\right) + 5 - 2.44 \tag{A-51}$$

Where the Reynolds number for this geometry is defined by $Re = \frac{V_{avg} 2t}{\nu}$, which is substituted into Eq. (A-51) and rearranged to give Eq. (A-52),

$$\sqrt{\frac{8}{f}} = 2.44 \ln\left(\frac{Re}{2}\sqrt{\frac{f}{8}}\right) - 2.56$$

$$\sqrt{\frac{1}{f}} = .8626 \ln\left(\frac{Re}{2}\sqrt{\frac{f}{8}}\right) - 0.9059$$

$$\sqrt{\frac{1}{f}} = 0.8626 \ln\left[\left(Re\sqrt{f}\right) - \ln\left(2\sqrt{8}\right)\right] - 0.9059$$

$$\sqrt{\frac{1}{f}} = 0.8626 \ln\left[\left(Re\sqrt{f}\right) - \ln\left(2\sqrt{8}\right)\right] - 0.9059$$

$$\sqrt{\frac{1}{f}} = 0.8626 \ln\left(Re\sqrt{f}\right) - 0.588 \tag{A-52}$$

Which is very similar to the expression for a circular pipe geometry, Eq.(A-53) [43],

$$\sqrt{\frac{1}{f}} = 0.8626\ln\left(\mathrm{Re}\sqrt{f}\right) - 1.02 \tag{A-53}$$

A relationship between the maximum velocity (canister velocity) and average velocity in the gap can be developed from Eq. (A-47) and Eq. (A-48) and manipulated to give Eq. (A-54),

$$V_{avg} = V_{max} - 2.44V^*$$

$$V_{avg} = V_c - 2.44\sqrt{\frac{f}{8}}V_{avg}$$

$$V_{avg}(1 + 0.8626\sqrt{f}) = V_c$$

$$V_{avg} = \frac{V_c}{(1 + 0.8626\sqrt{f})} \tag{A-54}$$

Completing a force and momentum balance,

$$P_1 - P_2 = \rho_C g l - \frac{\rho_f {V_{avg}}^2}{2} f\left(\frac{l}{D_C}\right)$$

$$P_1 - P_2 = \frac{\rho_f {V_{avg}}^2}{2}\left(f\frac{l}{D_h} + K_{form}\right) + \rho_f g l$$

Combining the equations as before,

$$\rho_c g l - \frac{\rho_f {V_{avg}}^2}{2}\left(f\frac{l}{D_c}\right) = \frac{\rho_f {V_{avg}}^2}{2}\left(f\frac{l}{D_h} + K_{form}\right) + \rho_f g l$$

$$2gl\left(\frac{\rho_c}{\rho_f}-1\right)=V_{avg}{}^2\left(f\frac{l}{D_h}+K_{form}+f\frac{l}{D_c}\right)$$

$$V_{avg}{}^2=\frac{2gl\left(\frac{\rho_c}{\rho_f}-1\right)}{\left(f\frac{l}{D_h}+K_{form}+f\frac{l}{D_c}\right)}$$

Plugging in the expression for V_{avg} described by Eq. (A-54), gives Eq. (A-55),

$$\left(\frac{V_c}{(1+0.8626\sqrt{f})}\right)^2=\frac{2gl\left(\frac{\rho_c}{\rho_f}-1\right)}{\left(f\frac{l}{D_h}+K_{form}+f\frac{l}{D_c}\right)}$$

$$V_c=(1+0.8626\sqrt{f})\sqrt{\frac{2gl\left(\frac{\rho_c}{\rho_f}-1\right)}{\left(f\left(\frac{l}{D_h}+\frac{l}{D_c}\right)+K_{form}\right)}} \quad \text{(A-55)}$$

Using the Eq. (A-52) and Eq. (A-55) iteratively, V_c can be calculated. For the reference scenario:

f= 1.27 x 10^{-2}

V_c=11.51 m/s

V_{avg}=10.49m/s

This analysis indicates that the average velocity in the gap is approximately 90% of the canister velocity. This is completely consistent, when compared to the same parameter for a highly turbulent flow in pipes, where V_{avg}/V_{max} values are typically between 0.8 and 0.87 [43]. In reality, the canister would have to be designed to withstand such an impact (in the case of an accidental drop when it is being lifted and emplaced).

Concerning the likelihood of the bottom of the borehole being open to a body of water:

1. If a large body of water exists at the bottom of the borehole, the borehole was not chosen or tested properly, as a body of water may indicate water flow or an aquifer that can transport radionuclides.
2. The open boundary condition would be noticed before the canister is even dropped. If there exists a large body of water that can allow for flow, (i.e the water is not forced up around the canister but is allowed to flow into the reservoir), then it will be impossible to actually fill the borehole with water in the first place, as it will constantly empty into the reservoir.
3. An unfueled test canister will be dropped first to verify good behavior.

A.5 Dimensionless Solution for the Closed Boundary Condition

Converting the expression for the terminal velocity it to a dimensionless form gives further insight into the behavior and controlling variables of the fluid flow, and improves verification of experimental results. Recall that the terminal velocity of the canister in the borehole in the open boundary condition was derived to be Eq. (A-19),

$$V_C = \sqrt{\frac{2gl\left(\frac{\rho_c}{\rho_f} - 1\right)}{\left[f\left(\frac{l}{D_h} + \frac{l}{D_c}\right) + K_{form}\right](V_{ratio} + 1)^2}} \tag{A-19}$$

The Reynolds number is determined by the velocity of the fluid. V_{f2}', the velocity of the fluid in the corrected frame of reference, is equal to the velocity of the canister multiplied by (V_{ratio}+1). Mulitplying both sides by (V_{ratio}+1),

$$V_C(V_{ratio} + 1) = \sqrt{\frac{2gl\left(\frac{\rho_c}{\rho_f} - 1\right)}{\left[f\left(\frac{l}{D_h} + \frac{l}{D_c}\right) + K_{form}\right](V_{ratio} + 1)^2}}(V_{ratio} + 1)$$

Cancelling terms,

$$V_{f_2,} = \sqrt{\frac{2gl\left(\frac{\rho_c}{\rho_f} - 1\right)}{\left[f\left(\frac{l}{D_h} + \frac{l}{D_c}\right) + K_{form}\right]}}$$

Multiplying both sides by ρ_f, D_h and dividing by μ,

$$\frac{\rho_f V_{f_2,} D_h}{\mu} = \sqrt{\frac{2gl\left(\frac{\rho_c}{\rho_f} - 1\right)\rho_f{}^2 D_h{}^2}{\mu^2\left[f\left(\frac{l}{D_h} + \frac{l}{D_c}\right) + K_{form}\right]}}$$

Substituting the Reynolds number, multiplying out ρ_f ,and rearranging terms,

$$Re = \sqrt{\frac{2gl\rho_f(\rho_c - \rho_f)D_h{}^2}{\mu^2\left[f\left(\frac{l}{D_h} + \frac{l}{D_c}\right) + K_{form}\right]}}$$

Multiplying and dividing the top of the expression within the square root by D_h:

$$Re = \sqrt{\frac{2g\rho_f(\rho_c - \rho_f)D_h{}^3\left(\frac{l}{D_h}\right)}{\mu^2\left[f\left(\frac{l}{D_h} + \frac{l}{D_c}\right) + K_{form}\right]}}$$

and substituting the Archimedes number gives the dimensionless form of the solution, Eq. (A-56) :

$$Re = \sqrt{\frac{Ar\left(2\frac{l}{D_h}\right)}{f\left(\frac{l}{D_h} + \frac{l}{D_c}\right) + K_{form}}} \qquad \text{(A-56)}$$

A.6 Numerical Integration of Acceleration (Closed Boundary Condition)

The conservation of momentum equation with a moving frame of reference can be written as Eq. (A-57),

$$\sum Forces_{CV} = \frac{d(MV_{CV})}{(dt)} = \frac{\partial V_{CV}}{\partial t} M + \frac{\partial M}{\partial t} V_{CV} \tag{A-57}$$

Where V_{CV} is the velocity of the control volume, which is drawn along surface of the canister and has equal velocity to the canister (V_c). Since there is no mass accumulating in the canister or control volume, the right hand term goes to zero and substituting the definition of acceleration yields Eq. (A-58),

$$\sum Forces_{CV} = \frac{d(MV_{CV})}{(dt)} = \frac{\partial V_{CV}}{\partial t} M = \frac{\partial V_C}{\partial t} M = a(t)M \tag{A-58}$$

where *a(t)* represents the acceleration of the canister (and control volume) as a function of time. Recall Eq. (A-1), which describes the forces that act on the canister,

$$\sum Forces = P_1 A_C + \tau\pi D_C l - P_2 A_C - Mg \tag{A-1},$$

Equating Eq. (A-58) and Eq. (A-1), using the definition for τ from Eq. (A-3), the definition of M from Eq. (A-4), this can be rearranged to give Eq. (A-59),

$$\sum Forces = A_C \left[(P_1 - P_2) - \rho_C g l + \frac{\rho_f V_f'(t)^2}{2} f\left(\frac{l}{D_C}\right) \right] = (\rho_C l A_C) a(t) \tag{A-59}$$

where $V_f'(t)$ represents the relative fluid velocity in the shifted frame of reference as a function of time. Substituting the relation of P_1 - P_2 from Eq. (A-9) and eliminating A_c gives Eq. (A-60),

$$(\rho_C l)a = \left[\left(\frac{\rho_f V_f'(t)^2}{2}\left(f\frac{l}{D_h} + K_{form}\right) + \rho_f g l\right) - \rho_C g l + \frac{\rho_f V_f'(t)^2}{2} f\left(\frac{l}{D_C}\right)\right] \tag{A-60}$$

Rearranging variables gives Eq. (A-61),

$$a = \frac{\rho_f V_f'(t)^2}{2\rho_C l}\left(f\left(\frac{l}{D_h} + \frac{l}{D_C}\right) + K_{form}\right) + \frac{\rho_f g}{\rho_C} - g \tag{A-61}$$

Applying Eq. (A-14),

$$a = \frac{d(V_c(t))}{dt} = \frac{\rho_f\left(V_C(V_{ratio}+1)\right)^2}{2\rho_C l}\left(f\left(\frac{l}{D_h} + \frac{l}{D_C}\right) + K_{form}\right) + \frac{\rho_f g}{\rho_C} - g \tag{A-62}$$

Discretizing the equation into finite time steps gives Eq. (A-63),

$$a(t) \approx \frac{\Delta(V_c(t))}{\Delta t} = \frac{\rho_f[V_C(t)(V_{ratio}+1)]^2}{2\rho_C l}\left(f\left(\frac{l}{D_h} + \frac{l}{D_C}\right) + K_{form}\right) + \frac{\rho_f g}{\rho_C} - g \tag{A-63}$$

Eq. (A-63) can be integrated numerically (stepwise) using the forward Euler method. This is completed by applying the initial condition that $V_c(t=0)=0$, using a small Δt, solving for the ΔV_c for each time step and adding it to the previous time step's velocity gives the velocity as a function of time. A more direct form is shown in Eq. (A-64),

$$\Delta(V_c(t_{n+1})) = \left[\frac{\rho_f[V_C(t_n)(V_{ratio}+1)]^2}{2\rho_C l}\left(f\left(\frac{l}{D_h} + \frac{l}{D_C}\right) + K_{form}\right) + \frac{\rho_f g}{\rho_C} - g\right]\Delta t \tag{A-64}$$

where t_n denotes current time step, and t_{n+1} denotes the incremental forward time step. The entire discrete integration process can be repeated on this velocity function to obtain position as a function of time

Appendix B. Experimental Results

B.1 Introduction

The experimental results greatly bolster the validity and confirm the basis of the analytical model. Unique canister and sensor design and careful variation of canister properties allowed for the model to be explored over a wide variety of conditions, within the space, cost and time constraints associated with laboratory investigation.

B.2 Canister Density and Fluid Temperature Variation (*Ar*)

Table B-1 presents the masses of components used to vary the density of the experimental canister.

Table B-1. Canister components for the fully loaded 14.79 kg canister

Description	**Mass (kg)**
Lead Bag #1	2.200
Lead Bag #2	2.202
Lead Bag #3	2.212
Lead Bag #4	2.202
Lead Bag #5	2.202
Lead Bag #6	2.202
Small Lead bag	0.376
Bottom plug	0.106
Plastic pipe with top plug	1.086
Total	**14.788**

For the tests described in Figure B-1, the predicted terminal velocity was 0.557 m/s and the measured terminal velocity averaged over 740 data points was 0.543 m/s.

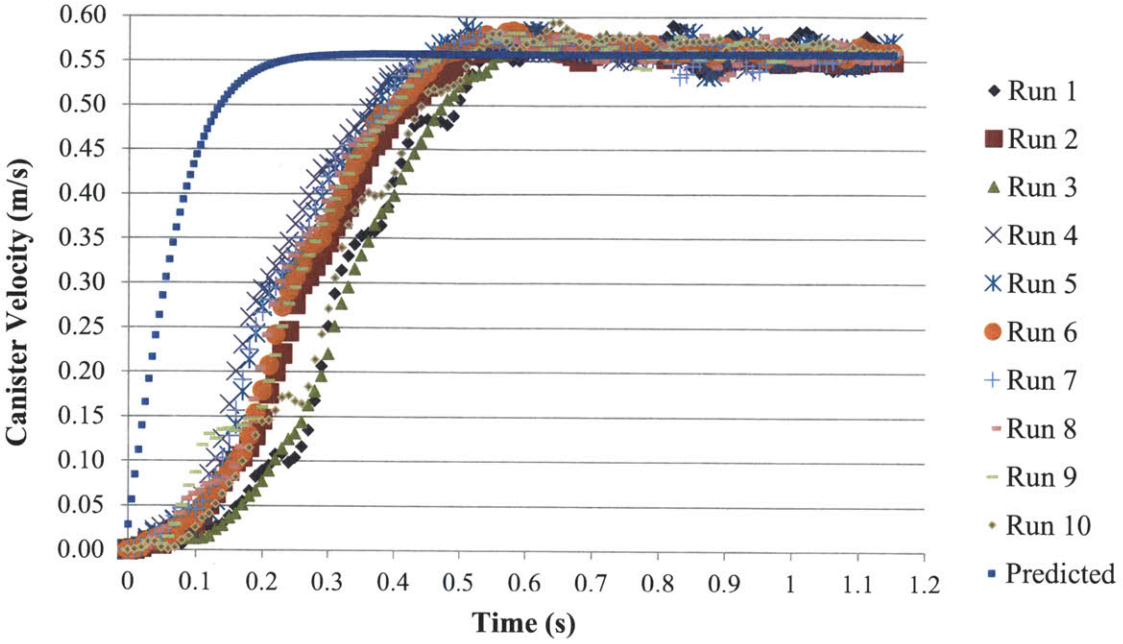

Figure B-1. Experimental results from 10 drop experiments, completed on September 20, 2010, using a 8.188 kg, reference sized canister. Velocity recorded at 100 hz.

For the 11 tests described in Figure B-2, the predicted terminal velocity was 0.683 m/s and the measured terminal velocity averaged over 627 data points was 0.704 m/s.

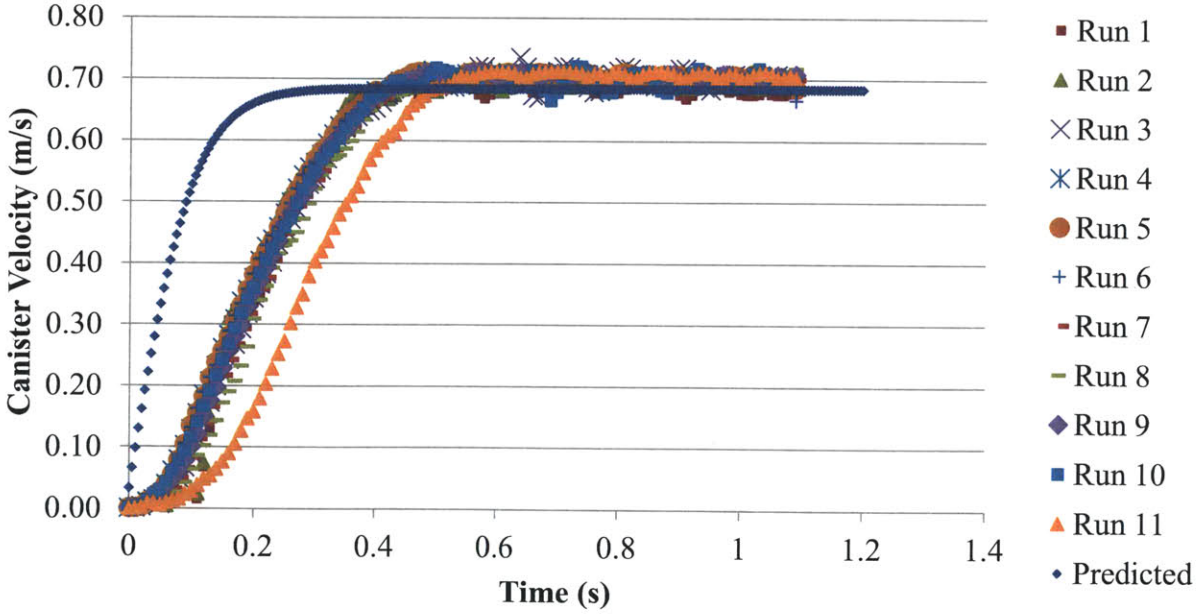

Figure B-2. Experimental results from 11 drop experiments, completed on October 7 2010, using a 10.388 kg, reference sized canister.

For the 9 tests described in Figure B-3, the predicted terminal velocity was 0.794 m/s and the measured terminal velocity averaged over 540 data points was 0.8046 m/s.

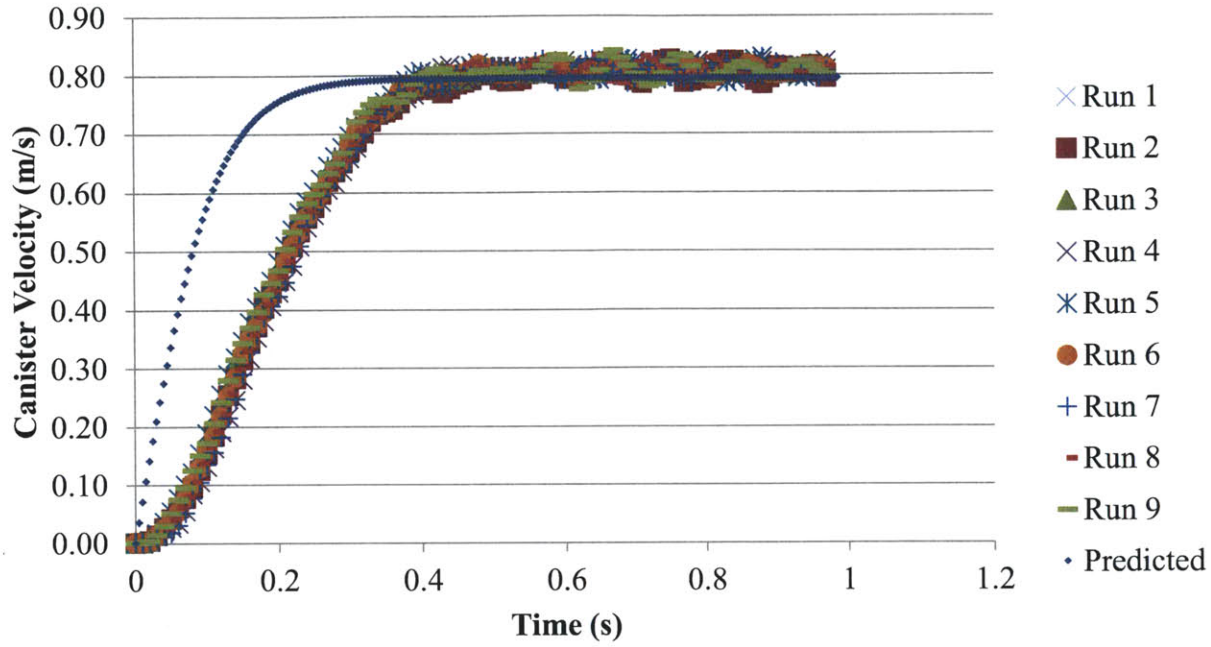

Figure B-3. Experimental results from 9 drop experiments, completed on October 10 2010, using a 12.588 kg, reference sized canister.

An additional 29 drop tests occurring in water temperatures between 48° and 92° C, using a 14.40 kg canister (same canister as described in Table B-1, but with the "small lead bag" removed) and the results, including those from Figure B-1, Figure B-2, Figure B-3 and are summarized in Table B-2.

Table B-2. Summary of drop tests completed to investigate the effect of Ar on Re.

# of runs	Fluid Temp. (° C)	Fluid Density (kg/m^3)	Canister mass (kg)	Canister Density (kg/m^3)	Fluid Viscocity (pa-s)	Terminal velocity of canister (m/s)	Relative Fluid velocity (m/s)	Reynolds number	Archimedes Number
3	22.5	997.61	14.79	4267	9.43E-04	0.8904	3.89E+00	3.79E+04	2.82E+07
9	22.5	997.61	12.59	3632	9.43E-04	0.8046	3.51E+00	3.43E+04	2.27E+07
11	22.5	997.61	10.39	2997	9.43E-04	0.704	3.08E+00	3.00E+04	1.73E+07
10	22.5	997.61	8.19	2363	9.43E-04	0.543	2.37E+00	2.31E+04	1.18E+07
1	92	963.95	14.40	4154	3.07E-04	0.908	3.97E+00	1.15E+05	2.57E+08
1	85.5	968.28	14.40	4154	3.33E-04	0.897	3.92E+00	1.05E+05	2.18E+08
1	79	972.4	14.40	4154	3.59E-04	0.886	3.87E+00	9.67E+04	1.88E+08
1	77.5	973.32	14.40	4154	3.66E-04	0.887	3.87E+00	9.51E+04	1.81E+08
1	76	974.23	14.40	4154	3.73E-04	0.886	3.87E+00	9.33E+04	1.74E+08
1	73.5	975.72	14.40	4154	3.85E-04	0.775	3.39E+00	7.91E+04	1.63E+08
1	72	976.6	14.40	4154	3.93E-04	0.859	3.75E+00	8.60E+04	1.57E+08
1	72	976.6	14.40	4154	3.93E-04	0.86	3.76E+00	8.61E+04	1.57E+08
1	71.5	976.89	14.40	4154	3.96E-04	0.871	3.80E+00	8.66E+04	1.55E+08
1	71	977.18	14.40	4154	3.98E-04	0.868	3.79E+00	8.58E+04	1.53E+08
1	66	979.99	14.40	4154	4.27E-04	0.854	3.73E+00	7.89E+04	1.33E+08
1	65.5	980.26	14.40	4154	4.30E-04	0.86	3.76E+00	7.90E+04	1.31E+08
1	64.8	980.67	14.40	4154	4.35E-04	0.862	3.77E+00	7.83E+04	1.28E+08
1	64.5	980.8	14.40	4154	4.36E-04	0.866	3.78E+00	7.84E+04	1.27E+08
1	64	980.8	14.40	4154	4.36E-04	0.87	3.80E+00	7.88E+04	1.27E+08
1	62	982.14	14.40	4154	4.53E-04	0.855	3.73E+00	7.47E+04	1.18E+08
1	61.5	982.4	14.40	4154	4.56E-04	0.844	3.69E+00	7.33E+04	1.17E+08
1	57	984.69	14.40	4154	4.88E-04	0.836	3.65E+00	6.79E+04	1.02E+08
1	57	984.69	14.40	4154	4.88E-04	0.856	3.74E+00	6.95E+04	1.02E+08
1	57	984.69	14.40	4154	4.88E-04	0.86	3.76E+00	6.99E+04	1.02E+08
1	57	984.69	14.40	4154	4.88E-04	0.83	3.63E+00	6.74E+04	1.02E+08
1	57	984.69	14.40	4154	4.88E-04	0.862	3.77E+00	7.00E+04	1.02E+08
1	49.5	988.01	14.40	4154	5.47E-04	0.852	3.72E+00	6.20E+04	8.11E+07
1	49.5	988.01	14.40	4154	5.47E-04	0.856	3.74E+00	6.23E+04	8.11E+07
1	48	988.9	14.40	4154	5.66E-04	0.853	3.73E+00	6.01E+04	7.58E+07
1	48	988.9	14.40	4154	5.66E-04	0.855	3.73E+00	6.02E+04	7.58E+07
1	48	988.9	14.40	4442	5.66E-04	0.86	3.76E+00	6.06E+04	8.27E+07

B.3 Results of Added Form Loss and Surface Roughness

Table B-3 presents the masses of components of the experimental canister with added form loss.

Table B-3. Canister components for the canister with added form loss (plug)

Description	Mass (kg)
Lead Bag #1	2.200
Lead Bag #2	2.202
Lead Bag #3	2.212
Lead Bag #4	2.202
Lead Bag #5	2.202
Lead Bag #6	2.202
Small Lead bag	0.376
Rubber weight	0.032
Bottom form loss	0.260
Plastic pipe with top plug	1.086
Total	**14.974**

Table B-4 presents the temperature and velocity data collected from the drop tests that involved an additional form loss and roughness.

Table B-4. Summary of experiments that varied form loss and surface roughness.

# of runs	Fluid Temp (° C)	Fluid Density (kg/m^3)	Can. mass (kg)	Can. Density (kg/m^3)	Viscosity (pa-s)	Terminal velocity of canister (m/s)	Relative Fluid velocity (m/s)	*Re*	*Ar*	Form loss plug?	Surface Roughness
1	77.5	973.32	14.97	4321	3.66E-04	0.75	3.28	8.04E+04	1.91E+08	Yes	Smooth
1	76	974.23	14.97	4321	3.73E-04	0.757	3.31	7.97E+04	1.84E+08	Yes	Smooth
1	76	974.23	14.97	4321	3.73E-04	0.745	3.25	7.84E+04	1.84E+08	Yes	Smooth
1	73.5	975.72	14.97	4321	3.85E-04	0.75	3.28	7.65E+04	1.72E+08	Yes	Smooth
1	72	976.6	14.97	4321	3.93E-04	0.77	3.36	7.71E+04	1.65E+08	Yes	Smooth
1	72	976.6	14.97	4321	3.93E-04	0.75	3.28	7.51E+04	1.65E+08	Yes	Smooth
5	22.5	997.61	15.102*	4321	9.43E-04	0.437	1.91	1.86 E+04	2.90E+07	Yes	60 grit
6	22.5	997.61	14.933**	4309	9.43E-04	0.547	2.39	2.33 E+04	2.86E+07	No	80 grit

*Sandpaper added 132 grams to the canister

**Sandpaper added 98.56 grams to the canister, and removing the form loss (plug) reduced the canister mass by 102 grams.

B.4 Measurement of Surface Roughness

Surface roughness was measured via an Olympus LEXT OLS3000 Confocal Scanning Laser Microscope. Figure B-4 and Figure B-5 present the images produced by the microscope's software package.

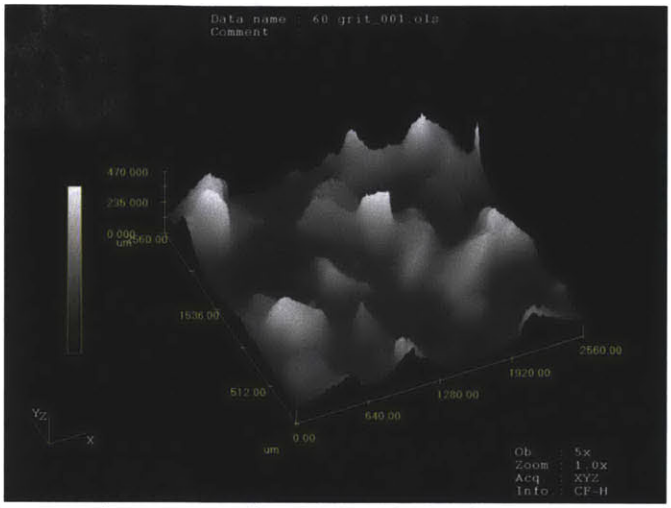

Figure B-4. Confocal microscopic contour plot of 60 grit sandpaper, with height exaggerated.

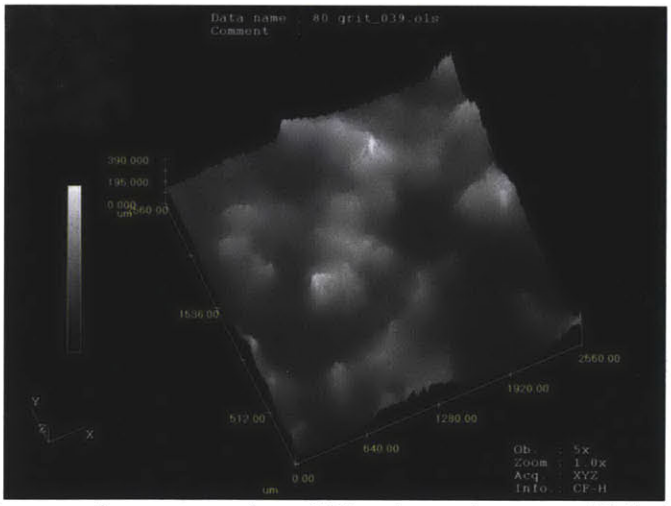

Figure B-5. Confocal microscopic contour plot of 80 grit sandpaper, with height exaggerated.

The software produced many measures of roughness, varying within a range by a factor of 6.The ten point mean roughness of the 60 grit sandpaper was calculated by the microscope's software to be 412 micrometers, somewhat matching the predictions of 271 microns, based on the literature search. For the 80 grit sandpaper the ten point mean roughness was 300 micrometers, slightly larger than the predicted value of 200 micrometers for the average particle size.

Table B-5. Summary of roughness parameters produced by the confocal microscope.

Grit	Average Particle Size (predicted) microns	Ten point mean roughness (measured) microns	Mean Roughness (predicted) microns	Mean Roughness (measured) microns
60	271	412.2406	67.09	60.278
80	195	311.95	53.8	40.36

Using "mean surface roughness" seems to underestimate the roughness of the surface. For example, the roughness of stainless steel is reported in literature to be 40 microns. Overall, the "mean surface roughness" metric unrealistically implies that the roughest of sandpaper grits has similar roughness to stainless steel. In reality, it would seem to be closer to that of cast iron, which has a reported roughness of 250-800 microns. Therefore, the ten point mean roughness was used as the measure for average particle size.

B.5 Error Analysis

Measurement uncertainty is propagated by adding the uncertainties of each measured, independent variable. The variables of importance for the canister velocity when determined by rotary motion are described by Eq. (B-1):

$$V = \omega \cdot 2\pi r \tag{B-1}$$

where ω is the rotational velocity and r is the radius of the pulley. In the region where terminal velocity has been achieved, ω is constant and can be approximated by Eq. (B-2),

$$V = \frac{C}{t} \cdot 2\pi r \tag{B-2}$$

where C is the number of cycles or rotations the pulley undergoes, and t is the time interval over which terminal velocity is achieved.

Since the computer and rotational meter record velocity, and there is no statement with regards to the tolerances of time recording, it is assumed that time measurement is a negligible source of uncertainty. The manufacturer reported the radius of the pulley to be 29 mm, and this was confirmed by measurement with calipers.

A large source of precision uncertainty results from measuring *C*. A physical explanation for the existence of precision uncertainty with the rotary motion sensor is the small tendency of the nylon string to slip around the rotary motion sensor during a test. The deviation is quantified by recording the return position of the rotary motion sensor and subtracting it from the starting position, before the canister was lifted and dropped. The average error per revolution is calculated by taking the absolute deviation after a full test and dividing it by the total number of revolutions during the entire drop. This would tend to overestimate the average error per revolution during testing, because it is most likely that the string slippage occurs after the test when the canister impacts (when tension in the nylon string is lost), not while the test is actually occurring. The expected error during the period of terminal velocity is calculated by taking the average error per revolution Table B-6 presents the data from 15 drop tests, showing the deviation and error from slippage.

Table B-6. Rotational motion sensor deviations from origin after 15 drop tests. Analysis completed for drop tests completed on February 10, 2011.

Trial	Error after full drop test (revolutions)	Total # of rev. in a full drop (revolutions)	Error per revolution (rev./rev)	# of revolutions during terminal velocity (revolutions)	Expected error during terminal velocity time interval (revolutions)
1	0.072	6.18	0.011650485	2.53	0.029476
2	0.036	6.658	0.005407029	2.59	0.014004
3	0.006	6.308	0.000951173	2.13	0.002026
4	0.011	6.656	0.001652644	2.21	0.003652
5	0.006	6.66	0.000900901	2.219	0.001999
6	0.005	6.675	0.000749064	2.202	0.001649
7	0.069	6.733	0.010248032	2.175	0.022289
8	0.042	6.588	0.006375228	2.075	0.013229
9	0.008	6.58	0.001215805	2.116	0.002573
10	0.011	6.53	0.001684533	2.112	0.003558
11	0.05	6.21	0.00805153	2.06	0.016586
12	0.061	6.33	0.009636651	2.08	0.020044
13	0.008	6.305	0.001268834	2.05	0.002601
14	0.006	6.594	0.000909918	2.065	0.001879
15	0.033	6.3611	0.005187782	2.07	0.010739

From Table B-6, the mean error in revolution measurement (during the terminal velocity time interval) can be estimated using Eq. (B-3),

$$u_\mu = t_{.025,n-1}\frac{\sigma}{\sqrt{n}} \tag{B-3}$$

where u_μ is the 95% precision uncertainty in μ, n is the number of measurements made, $t_{.025,n-1}$ is the student t statistic or "t factor" obtained from tables given n ,and σ is the standard deviation of the sample. Substituting in $n=15$, $t_{.025,n-1}= 2.131$ and calculating σ, $u_{\mu,c}$is calculated to be 4.99 x 10^{-3} rotations.

There also exists precision uncertainty from the rotary motion sensor angle measurement system, which has a rated tolerance of 1 degree, or 2.777 x 10^{-3} rotations. Adding this to the previous source of rotational uncertainty yields $u_{\mu,c}$= 7.77 x 10^{-3} rotations.

If one assumes the error in radius measurement to be equal to the diameter of the fishing line, then the $u_{\mu,r}$ is estimated to be 0.7112 mm. Since time is considered a certain factor, $u_{\mu,t}$ is assumed to be 0.

Assuming the independent variables are statistically independent, the estimated precision error in V is then calculated as Eq. (B-4):

$$u_y = \sqrt{\left(\frac{\partial y}{\partial x_1}u_1\right)^2 + \left(\frac{\partial y}{\partial x_2}u_2\right)^2 + \cdots + \left(\frac{\partial y}{\partial x_n}u_n\right)^2} \tag{B-4}$$

where y is a parameter of interest determined by variables $x_1, x_2, \ldots, x_n$. u_y is the precision in measurement uncertainty the quanity y, determined by the measurement uncertainty of input variables $u_1, u_2, \ldots, u_n$, and the partial derivatives of y with respect to $x_1, x_2, \ldots, x_n$. Applying Eq. (B-4) to Eq. (B-2),

$$u_V = \sqrt{\left(\frac{dV}{dC} \cdot u_{\mu,C}\right)^2 + \left(\frac{dV}{dr} u_{\mu,r}\right)^2 + \left(\frac{dV}{dt} u_{\mu,t}\right)^2}$$

calculating derivatives and substituting,

$$u_V = \sqrt{\left(\frac{2\pi r}{t} \cdot u_{\mu,C}\right)^2 + \left(\frac{2\pi C}{t} u_{\mu,r}\right)^2} \quad \text{(B-5)}$$

Substituting experimental values (r= 29 mm, t = *0.5 sec, C=2.17)* into Eq. (B-5) yields u_V = 1.93 x 10^{-2} m/s. Thus is it is concluded that precision in measurement uncertainty is an insignificant source of error.

Random statistical spread is another contributor to the error in the data. For example consider the data from the experiment completed on Nov. 3, 2010 with a 14.396 kg canister dropped into 85.5° C water.

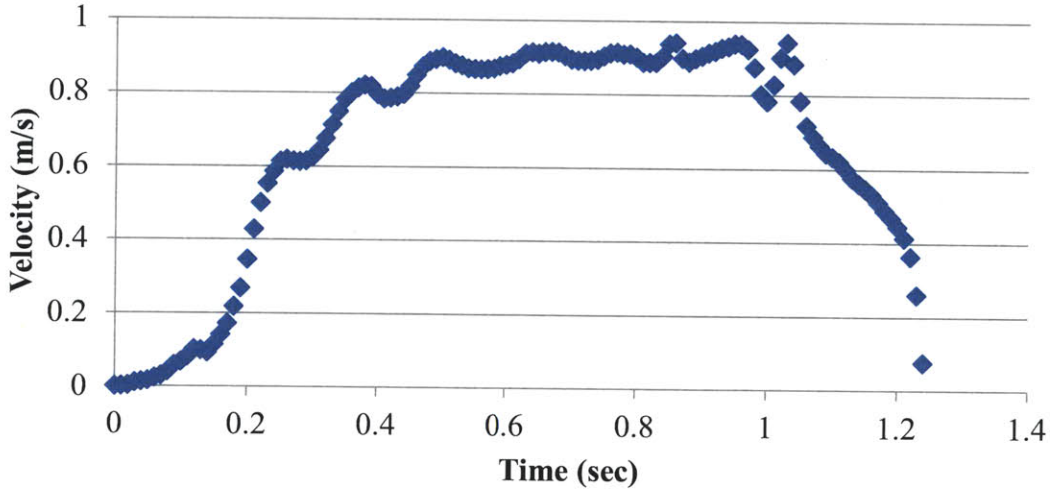

Figure B-6. Velocity data obtained from a drop test using 14.396 kg reference geometry canister into 85.5° C water.

The standard deviation from the average terminal velocity in the time interval of 0.49 to 0.96 seconds in the calculated in Excel yields σ= 1.997 x 10^{-2}. For such a large sample (n=48), the t statistic converges to 2, and $u_{\mu,V}$ is calculated to be 5.77 x 10^{-3} m/s. Adding this to the precision

uncertainty yields an overall measurement uncertainty of 2.51 x 10^{-2} m/s. Compared to the mean value of terminal velocity (~0.75 m/s), this represents a relative error of 3.34%.

As for the model uncertainty, the greatest error lies in the measurement of the canister diameter. For example, consider the canister measurements for the experiments on February 10, 2011.

Table B-7. Measured values for the canister diameter.

Canister Diameter (mm)
67.82
67.8
67.85
68.08
68.02
68.49
68.08

The standard deviation σ for the data in Table 2 is 0.2399. Using the student t statistic for n = 7, $t_{.025,n-1}$= 2.365 and therefore u_μ= .2144 mm. The estimates for the resulting error in model predictions were completed using the "range" method, by testing the maximum and minimum possible values of D_h and checking the resulting range in terminal velocity. This absolute error was converted to a relative error, which was calculated to be 3.44%. The final graph including all errors is shown in Figure 5-8.

Appendix C. Thermal Analysis of Canister During Emplacement

C.1. Introduction

In order to ensure that potentially troublesome temperatures would not be experienced during the emplacement procedure, a thermal analysis is applied. The square assembly canister is treated as a homogenous region with uniform conductivity and effective circular diameter. Conduction through the concrete cask (necessary for radiation shielding) poses the greatest barrier to heat transfer. Overall this requires an iterative approach because the heat transfer coefficient associated with natural convection on the surface of the concrete cask is a function of the temperature of the surface.

C.2. Surface Temperatures

The decay heat can be described by an inverse power law relationship in Equation (C-1):

$$q' = \frac{2200}{t^{0.75}} \tag{C-1}$$

where, t is canister age in years, and q' is linear heat generation in W/m.

This equation applies to a 4.2 m tall, 0.2417 m effective diameter, PWR assembly (17X17) with 0.5 metric tons of uranium at 60 GW-day/MTU of burnup. Outside of the assembly is a 12.1 mm thick steel casing in addition to a 0.5 m thick concrete cask to provide shielding. A diagram of the homogenized assembly, steel casing, and concrete cask configuration was shown previously in Figure 6-1. The overall canister diameter is then:

$$D = 2r_{cask} = 2(r_{canister} + \delta_{conc}) = 2(r_{assembly} + \delta_{steel} + \delta_{conc})$$

where,

D is the overall cylinder package diameter in m,

$r_{assembly}$ is the homogenized fuel assembly effective radius in m,

r_{cask} is the cask outer radius in m,

$r_{canister}$ is the steel canister outer radius in m,

δ_{conc} is the concrete thickness in m,

δ_{steel} is the steel canister thickness in m.

The cask surface temperature as a function of the decay heat can be analyzed through dimensionless heat transfer correlations. The convective heat transfer coefficient for a cylinder experiencing natural convection can be defined in terms of the Rayleigh (*Ra*), Prandtl (*Pr*), and Nusselt (*Nu*) dimensionless groups- Eqs.(C-2), (C-3), and (C-4). The Rayleigh number for is defined as in Eq. (C-2):

$$Ra_d = \frac{g\beta(T_{cask} - T_{air})D^3}{\nu\alpha} \tag{C-2}$$

where,

g is gravitational acceleration (m/s^2)

β is expansion coefficient in (1/K)

ν is kinematic viscosity (m^2/s)

α is thermal diffusivity in (m^2/s)

T_{air} is the air temperature in (°K)

T_{cask} is the cask surface temperature (°K)

The Prandtl number is defined in Eq. (C-3)

$$Pr = \frac{\mu\, c_p}{k} \tag{C-3}$$

where,

μ is the dynamic viscosity (Pa-s),

c_p is the specific heat capacity of the fluid in (J/kg-°K) and

k is the fluid conductivity (W/m-°K).

The definition and correlation *Nu=f(Ra,Pr)* is shown in Eq. (C-4) for a horizontal cylinder [64],

$$\overline{Nu}_d = \left\{0.60 + \frac{0.387 {Ra_d}^{1/6}}{[1 + 0.559/Pr^{9/16}]^{8/27}}\right\}^2 = \frac{hD}{k} \tag{C-4}$$

where,

Ra_d is the Rayleigh number based on the cylinder diameter,
Pr is the Prandtl number of the fluid, and
h is the convective heat transfer coefficient (W/m^2-°K).

The canister heat dissipation rate in W/m through radiation and natural convection is defined in Eq. (C-5),

$$q' = q'_{conv} + q'_{rad} = h\pi D(T_{cask} - T_{air}) + \varepsilon\sigma\pi D({T_{cask}}^4 - {T_{air}}^4) \quad \text{(C-5)}$$

where,
ε is emissivity and
σ is the Stefan-Boltzmann constant in W/m^2-°K^4.

By setting the canister heat dissipation rate equal to the canister decay heat (steady state assumption) it is possible to iteratively solve for the surface temperature of the canister package, using Eq (C-6),

$$\frac{2200}{t^{0.75}} = h\pi D(T_{cask} - T_{air}) + \varepsilon\sigma\pi D({T_{cask}}^4 - {T_{air}}^4) \quad \text{(C-6)}$$

The temperature difference between the cask surface temperature and steel canister surface is defined as Eq. (C-7),

$$T_{canister} = \frac{\ln(r_{cask}/r_{canister})}{2\pi k_{conc}} + T_{cask} \quad \text{(C-7)}$$

where,
$T_{canister}$ is the canister surface temperature (°K) and
k_{conc} is the concrete conductivity (W/m-°K).

The steel canister contributes to a very small temperature difference between the canister surface temperature and assembly surface temperature, defined in Eq. (C-8),

$$T_{assembly} = \frac{\ln(r_{canister}/r_{assembly})}{2\pi k_{steel}} + T_{canister} \quad \text{(C-8)}$$

where,

$T_{assembly}$ is the canister surface temperature (°K),

k_{steel} is the steel canister conductivity in (W/m-°K).

The centerline temperature is defined in Eq. (C-9),

$$T_{ctr} = \frac{q'}{4\pi k_{eff}} + T_{assembly} \quad \text{(C-9)}$$

where,

T_{ctr} is the canister centerline temperature (°K),

q' is linear heat generation in W/m

R is canister radius in m

k_{eff} is the effective canister conductivity (W/m-°K)

The assumed values for the thermal analysis are summarized in Table C-1.

Table C-1. Assumed material and thermal parameters for analysis of the shielded canister temperature distributions[12] and from Table A.3 [64] .

Parameter	Value	Units
g	9.8	m/s^2
β	2.725×10^{-3} (air at 94 °C)	$1/°K$
v	2.28×10^{-5} (air at 94 °C)	m^2/s
α	3.285×10^{-5} (air at 94 °C)	m^2/s
k_{air}	0.0313 (air at 94 °C)	$W/m°K$
k_{conc}	1.4	$W/m°K$
k_{steel}	50	$W/m°K$
k_{eff}	0.63	$W/m°K$
Pr	0.697 (air at 94 °C)	
ε	0.85	
σ	5.67×10^{-8}	$W/m^2°K^4$
T_{air}	23	°C
$r_{assembly}$	0.12085	m
$r_{canister}$	0.1269	m
r_{cask}	0.6269	m

Using the assumed values, Figure 6-2 shows the canister decay heat, surface temperature, and centerline temperature versus the number of years the fuel assembly has been removed from the reactor.

C.3. Cylindrical Temperature Distribution

The internal temperature profile within a cylinder is defined by Eq. (C-10) [64],

$$T(r) = \frac{\dot{q}R^2}{4k_{eff}}\left(1 - \frac{r^2}{R^2}\right) + T_s \tag{C-10}$$

where,

r is the radius in m

R is canister radius in m

k_{eff} is the fuel assembly effective conductivity in W/m-K

$\dot{q}$ is the volumetric heat generation W/m^3

Converting volumetric heat generation term to linear heat generation term the resulting temperature distribution is Eq. (C-11),

$$\dot{q} = \frac{q'}{\pi R^2}$$

$$T(r) = \frac{q'}{4\pi k_{eff}}\left(1 - \frac{r^2}{R^2}\right) + T_s \tag{C-11}$$

The generalized formula for the temperature distribution for cylindrical geometry is Eq. (C-12) [64],

$$T(r) = \frac{\dot{q}r^2}{4k_{eff}} + C_1 \ln r + C_2 \tag{C-12}$$

The boundary conditions define the temperature at the inner and outer radius, given by Eq (C-13) and Eq. (C-14),

$$T(r_{in}) = T_{in} \tag{C-13}$$

$$T(r_{out}) = T_{out} \tag{C-14}$$

Substituting Eq. (C-14) into Eq. (C-12) and solving for C_2 gives Eq. (C-15),

$$T_{out} = \frac{\dot{q} {r_{out}}^2}{4k_{eff}} + C_1 \ln r_{out} + C_2$$

$$C_2 = T_{out} - \frac{\dot{q} {r_{out}}^2}{4k_{eff}} - C_1 \ln r_{out} \tag{C-15}$$

Substituting the Eq (C-13) into Eq. (C-12) solving for C_1 gives Eq. (C-16),

$$T_{in} = \frac{\dot{q} {r_{in}}^2}{4k_{eff}} + C_1 \ln r_{in} + C_2$$

$$T_{in} = \frac{\dot{q} {r_{in}}^2}{4k_{eff}} + C_1 \ln r_{in} + T_{out} - \frac{\dot{q} {r_{out}}^2}{4k_{eff}} - C_1 \ln r_{out}$$

$$C_1 \ln \frac{r_{out}}{r_{in}} = T_{out} - T_{in} - \frac{\dot{q}}{4k_{eff}} ({r_{out}}^2 - {r_{in}}^2)$$

$$C_1 = \frac{T_{out} - T_{in} - \frac{\dot{q}}{4k_{eff}} ({r_{out}}^2 - {r_{in}}^2)}{\ln \frac{r_{in}}{r_{out}}} \tag{C-16}$$

Substituting Eq. (C-15) and Eq. (C-16) into Eq. (C-12) and collecting terms gives Eq. (C-17),

$$T(r) = \frac{\dot{q} r^2}{4k_{eff}} + \frac{T_{out} - T_{in} - \frac{\dot{q} {r_{out}}^2}{4k_{eff}} ({r_{out}}^2 - {r_{in}}^2)}{\ln \frac{r_{in}}{r_{out}}} \ln r + T_{out} - \frac{\dot{q} {r_{out}}^2}{4k_{eff}} - \frac{T_{out} - T_{in} - \frac{\dot{q}}{4k_{eff}} ({r_{out}}^2 - {r_{in}}^2)}{\ln \frac{r_{in}}{r_{out}}} \ln r_{out}$$

$$T(r) = \frac{\dot{q}}{4k_{eff}} (r^2 - {r_{out}}^2) - \frac{T_{out} - T_{in} - \frac{\dot{q}}{4k_{eff}} ({r_{out}}^2 - {r_{in}}^2)}{\ln \frac{r_{in}}{r_{out}}} \ln \frac{r}{r_{out}} + T_{out} \tag{C-17}$$

Defining volumetric heat generation rate as a function of q', substituting it into Eq. (C-17) and simplifying terms gives Eq. (C-18),

$$\dot{q} = \frac{q'}{\pi(r_{out}^2 - r_{in}^2)}$$

$$T(r) = \frac{q'}{4\pi k_{eff}} \frac{(r^2 - {r_{out}}^2)}{(r_{out}^2 - r_{in}^2)} - \frac{T_{out} - T_{in} - \frac{q'}{4\pi k_{eff}} \frac{({r_{out}}^2 - {r_{in}}^2)}{(r_{out}^2 - r_{in}^2)}}{\ln \frac{r_{in}}{r_{out}}} \ln \frac{r}{r_{out}} + T_{out}$$

$$T(r) = \frac{q'}{4\pi k_{eff}} \frac{(r^2 - {r_{out}}^2)}{(r_{out}^2 - r_{in}^2)} - \frac{T_{out} - T_{in} - \frac{q'}{4\pi k_{eff}}}{\ln \frac{r_{in}}{r_{out}}} \ln \frac{r}{r_{out}} + T_{out} \qquad \text{(C-18)}$$

Using the assumed values from Table C-1, the temperature profiles were calculated. The internal temperature distribution for various linear heat generation rates is shown in Figure 6-3.